DEVELOPMENT OF ELECTROCATALYSTS IN SOLID ACID FUEL CELLS

Thesis by

Haemin Paik

In Partial Fulfillment of the Requirements for

the Degree of

Doctor of Philosophy

CALIFORNIA INSTITUTE OF TECHNOLOGY

Pasadena, California

2019

(Defended May 3, 2019)

Haemin Paik
ORCID: 0000-0001-8358-6067

ACKNOWLEDGEMENTS

First and foremost, I am grateful to my thesis advisor, professor Sossina Haile. She has been and will be my role model as a woman scientist. She not only gave me deliberate and thoughtful guidance on my research works, but she also guided me on a personal level. It was my pleasure and honor to work with her for my PhD program.

It was not an easy decision to move to Evanston with her, leaving sunny Pasadena behind. However, at the end, I came to appreciate the beautiful scenery of Evanston as well, and have had countless valuable experiences at Northwestern University. I would like to thank all of Caltech crews, Tim, Sihyuk, Moureen, Hadi, Vanessa, Ho-Il, Chris, Mike and Anu, who moved to Chicago together and helped me to adapt to the Chicago winter. I also would like to thank Northwestern University affiliated group members who warmly welcomed us and helped to make a wonderful new group culture. I especially would like to thank Dae-Kwang, Austin, Shobhit, Xin (Xu), and Sheel, who contributed to a great part of my thesis projects.

My thesis committee members, professor William Johnson, William Goddard, and George Rossman, gave valuable and significant comments on my research projects with their keen insight. The intellectual discussion with them during the PhD qualifying exam and thesis defense expanded the scope of my thinking and led to my research to a meaningful direction.

I also would like to acknowledge my collaborators, professor Stephen Skinner, professor Joseph Hupp, Dr. Andrey Berenov, Dr. Jian Liu, Dr. Calum Chisholm, and Fernando Campos. My mentees Kaiting and Christian, and visiting scholar Dr. Sheng-Yuan Kao also gave meaningful contributions to the research projects.

There were many scientists and specialists, from specialists in industries to research professors on campus who supported my endeavor, and I am grateful for their assistance. Without their knowledge and specialties, I couldn’t have done many of my experiments and analysis.

I owe my gratitude to Caltech community for making Caltech such a distinguished and amazing place to work at, and helping me be a part of it. Incredibly supportive staffs on campus, including Jonathan, Christy, Daniel, and Laura (F. Kim) helped me to adapt quickly

in a new environment. Of course, without my classmates, roommates, and friends, especially Laura (B. Kim), Serim, Gahye, Jingjing, Sisir, Stephen, Heidi, and Cecilia, I would not have survived the course works and the qualifying exam. I also would like to thank Northwestern University and Korean catholic church community for making Chicago my second home. I would like to also thank people who came to so many coffee breaks and quick dinners with me whenever I asked - Youngeun, Ha-Kyung, Hyojun, Sarah, Hyejin, Dongjoon, and Yongjin. All my old friends back in South Korea, especially Sehee, Elenora, and Bomin, have been amazingly supportive. I am indeed grateful to be surrounded by so many wonderful people. My last six years have been as bright as they were for the kind people I had.

I am also truly fortunate to meet Yong Jun, who is the most considerate and earnest person I have ever met. He has been ever so supportive and patient with me whenever I struggled with my concerns and insecurity until the end of this journey.

Lastly, my family has been the best supporters during the long and tough journey. I would have not completed the PhD program without them. I would like to express deep gratitude for the endless love and trust from my parents and artistic diagrams my sister drew for the figures in the thesis. I would like to dedicate this thesis to them.

All the research works were financially supported by the Kwanjeong Education Foundation, U.S. Department of Energy through ARPA-e, Northwestern University, and Caltech fellowships.

ABSTRACT

Solid acid fuel cells (SAFCs) can operate at intermediate temperature (near 250 °C) using a non-toxic, solid proton-conducting electrolyte, CsH_2PO_4, which allows for fuel flexibility, high efficiency, inexpensive auxiliary components, and easy on-off cycling. Despite these features, large activation overpotentials at the electrodes require high Pt loadings in order to achieve acceptable power output. Few alternatives to Pt have emerged for either the hydrogen oxidation reaction or the oxygen reduction reaction in SAFCs. This thesis explores the use of Pd and Pd-containing alloys for electrocatalysis in SAFCs to reduce overall precious metal loading and therefore reduce cost to commercialization.

First, this work explores the use of Pd at the SAFC anode, assessing both catalytic activity for hydrogen electro-oxidation and reactivity with the CsH_2PO_4 electrolyte. A thin film geometry, in which nanometric layers of metal were deposited onto a polycrystalline disk of CsH_2PO_4 was used to simplify the device and facilitate interpretation electrochemical behavior. Using a symmetric geometry, the cells were examined under a uniform hydrogen-rich gas. It was found that Pd reacts with CsH_2PO_4, forming palladium phosphide (Pd-P) at the metal-electrolyte interface. With the aim studying the behavior of Pd in the absence of this reactivity, Pd overlain on Pt was examined in a bilayer geometry of Pd | Pt | CsH_2PO_4 | Pt | Pd. The bilayer Pt | Pd films show much higher activity for hydrogen electro-oxidation than films of Pt alone, as measured by AC impedance spectroscopy. *Ex-situ* low energy ion scattering and scanning transmission electron microscopy revealed that Pd diffused into the Pt layer under operating conditions. The extremely high activity of the interdiffused films suggest that Pd catalyzes reactions at both the metal-gas and metal-electrolyte interfaces, and furthermore facilitates rapid hydrogen diffusion rates through the films.

The high activity of Pt | Pd films, in which Pd eventually contacts the underlying electrolyte due to interdiffusion of the metals, motivates an investigation of Pd-based catalysts (Pd and Pd-P) for hydrogen electro-oxidation in a fuel cell relevant configuration. Working electrodes were formed from a mixture of Pd on carbon and the electrolyte material. The hydrogen oxidation kinetics from Pd, Pd_6P, and $Pd_3P_{0.8}$ were observed to be comparable. The result is consistent with the observation that Pd catalyst reacts with CsH_2PO_4 and converts into Pd-P during cell operation. Both Pd and Pd-P appear to be more effective electrocatalysts for hydrogen oxidation than the equivalent mole percent of Pt supported on carbon. Further enhancement of Pd catalytic activity is achieved by reducing its crystallite size.

Lastly, this work examines the catalytic activity of Pd for oxygen reduction at the SAFC cathode. Evaluation of this system is complicated by the instability of Pd on CsH_2PO_4 under oxidizing conditions, which causes microstructure collapse and performance degradation. A SnO_2 thin film was introduced as a barrier layer to inhibit Pd reactivity with CsH_2PO_4 and as a structural support for the catalyst. Employing atomic layer deposition, a SnO_2 thin film was deposited either between the Pd and CsH_2PO_4 interface, or over the Pd catalyst. Both Pd-SnO_2 bilayers show improved fuel cell performance stability compared to a Pd-only control, forming Pd-Sn alloys under cathode conditions. This suggests that the formation of Pd-Sn alloy stabilizes the metallic phase of Pd, improving catalytic activity. This work presents a new approach for designing the cathode materials for SAFCs.

PUBLISHED CONTENT AND CONTRIBUTIONS

Chapter 3

Paik, H., Berenov, A. V., Skinner, S. J., Haile, S. M., Hydrogen Oxidation Kinetics on Platinum-Palladium Bimetallic Thin Films for Solid Acid Fuel Cells, *APL Materials*, **7**, 013201 (2019) doi : 10.1063/1.5050093

H. Paik participated in the conception of the project, performed the experiment and analysis, and wrote the manuscript.

Appendix A

Lim, D.-K, Liu J., Pandey S. A., Paik, H., Chisholm, C. R. I., Hupp, J. T., Haile, S. M., Atomic layer deposition of Pt@CsH_2PO_4 for the cathodes of solid acid fuel cells, *Electrochimica Acta*, **288**, 12 (2018) doi : 10.1016/j.electacta.2018.07.076

H. Paik participated in the conception of the project, performed the part of experiment and analysis, and review the manuscript.

TABLE OF CONTENTS

LIST OF FIGURES

LIST OF TABLES

Chapter 1

INTRODUCTION

1.1 Overview

Fuel cells convert chemical energy into electrical energy through the electrochemical reaction of an oxidant and a reductant. These devices can generate electricity with less impact on the environment than other energy conversion technologies, such as internal combustion engines or batteries. The merits of fuel cells include high energy conversion efficiency, low emission of harmful gases and smoke, and low noise and mechanical vibration. Fuel cells operating at higher temperatures benefit from having high energy conversion efficiency, and fuel flexibility. On the other hand, operating at lower temperatures gives the advantages of lower cost components and easy stop/start operation. Intermediate temperature fuel cells, which operate at 200-500 °C, combine the benefits of high and low temperature operation. Solid acid fuel cells (SAFCs) have drawn attention for their operability at intermediate temperature using the non-toxic, proton-conducting solid electrolyte, cesium dihydrogen phosphate (CsH_2PO_4).[1,2] At 250 °C CsH_2PO_4 displays high proton conductivity, ~10^{-2} S/cm, good stability, and high fuel cell power density.[3,4] While many of the performance characteristics of SAFCs are now approaching commercial requirements, high Pt loadings (~2 mg_{Pt}/cm^2 for both electrodes combined) have hampered market entry. Moreover, few alternatives to Pt have emerged for either the hydrogen oxidation reaction or the oxygen reduction reaction in SAFCs.

Here, I present a general introduction to fuel cells and electrocatalysis is presented, after which I proceed to the current status and progress of electrocatalysis of SAFCs. The challenges and opportunities for developing the electrocatalysts in SAFCs, arising from the unique features of the solid acid electrolyte, are then described in this chapter.

1.2 Fuel cells

1.2.1 Basic theory

The definition of a fuel cell is an electrochemical cell converting the chemical energy of a fuel into electrical energy as output. A fuel cell can continue to produce electricity as long as fuel is delivered. Generally, a fuel cell has been compared with a battery in regard to generating electricity from an electrochemical cell. The main difference between the two is that a battery lowers its chemical potential as it is used, while a fuel cell has the capacity to maintain a constant chemical potential when using a continuous fuel supply. A combustion engine/turbine also converts the chemical energy of fuel into electrical energy. Unlike a fuel cell, however, we need to burn fuel in order to produce the heat energy, which in turn generates mechanical energy. Subsequently, the process converts mechanical energy into the final state, electrical energy. During this process, it creates lots of toxic byproducts, smoke, noise, and heat release. Accordingly, fuel cells are advantageous in terms of energy conversion efficiency, and environmental impact.

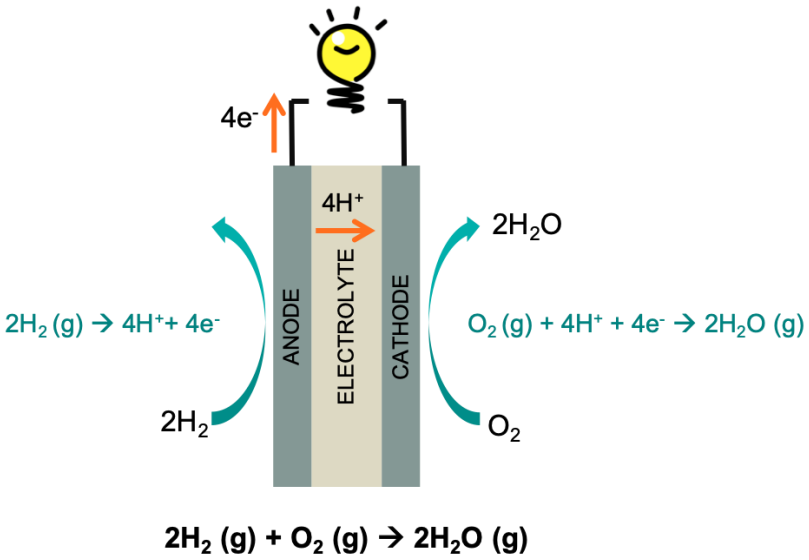

Figure 1.1 Schematic of a fuel cell with a proton conductive electrolyte membrane

Figure 1.1 describes a simple hydrogen fuel cell system with a proton conducting electrolyte. Instead of burning a hydrogen in one place, the combustion reaction is split into two half-cell reactions occurring at spatially separated electrodes with the help of an electrolyte that allows only ions to pass:

$$2H_2(g) \rightarrow 4H^+ + 4e^- \quad (1.1)$$

$$O_2(g) + 4H^+ + 4e^- \rightarrow 4H_2O\ (g) \quad (1.2)$$

An external circuit transmits the generated electrons at the hydrogen side to do work (*e.g.* lighting a lightbulb) and enter to the other side of the cell. At the oxygen side, electrons from the external circuit and protons transported through the electrolyte membrane combine with accessible oxygen toward forming the final product, H_2O. Overall, the net cell reaction is the same as in the hydrogen combustion system:

$$2H_2(g) + O_2(g) \rightarrow 2H_2O\ (g) \quad (1.3)$$

Understanding the thermodynamics of a fuel cell is beneficial to determine possible fuel cell systems, and to estimate the upper limits on the maximum electrical power density generated from a cell. Using the Gibbs free energy of formation of the reaction, ΔG_{rxn}^{0}, theoretical voltage across a fuel cell can be calculated. The relation between the electrochemical potential *E* and Gibbs free energy of formation is expressed by Nernst equation.

$$E = -\frac{\Delta G}{nF} \tag{1.4}$$

Here, *n* is the number of electrons transferred in an electrochemical reaction, and *F* is Faraday constant.

Since an actual fuel cell is operated away from standard state conditions, the free energy change at operating conditions, ΔG, appears with additional variables of temperature and chemical activities of gases participating the reaction.

$$\Delta G = \Delta G^{0} + RTln\frac{\Pi a_{products}^{n_i}}{\Pi a_{reactants}^{n_i}} \tag{1.5}$$

where *R* is ideal gas constant and n_i is stoichiometric coefficient. In general, the chemical activity for a gas can be expressed with its partial pressure. Accordingly, the free energy change for the reaction (1.3) can be expressed as:

$$\Delta G = \Delta G^{0} + RTln\frac{(pH_2O)^2}{(\mathrm{p}H_2)^2(pO_2)} \tag{1.6}$$

Using an equation (1.4), equation (1.6) can be rewritten as:

$$E = E^{0} - \frac{RT}{4F}ln\frac{(pH_2O)^2}{(\mathrm{p}H_2)^2(pO_2)} \tag{1.7}$$

This is the so-called equilibrium or theoretical Nernst potential for a given cell, indicating the maximum voltage obtainable from a fuel cell.

In an ideal fuel cell, this voltage should be constant despite how much current drawn from a cell. In reality, however, the potential across a fuel cell is lower than the theoretical potential and decreases further when more current is drawn from a cell. Irreversible losses cause undesirable voltage drop, which become greater as more current leaves from a cell. These losses are described by overpotentials meaning the potential difference between the theoretical potential and the one experimentally obtained. Three major types of overpotentials are considered to describe the voltage drop of a real fuel cell: the activation overpotential from the kinetics of electrochemical reactions, the ohmic overpotential from the ionic and electronic conduction across a cell, and the concentration overpotential from the limited mass transport. The real voltage across the current density j is expressed by subtracting the overpotentials from the Nernst potential.

$$E(j) = E_{eq} - \eta_{act} - \eta_{ohmic} - \eta_{conc} \tag{1.8}$$

The gas leaks or electronic leaks across the electrolyte also lead to an overpotential, which is sometimes small enough to ignore.

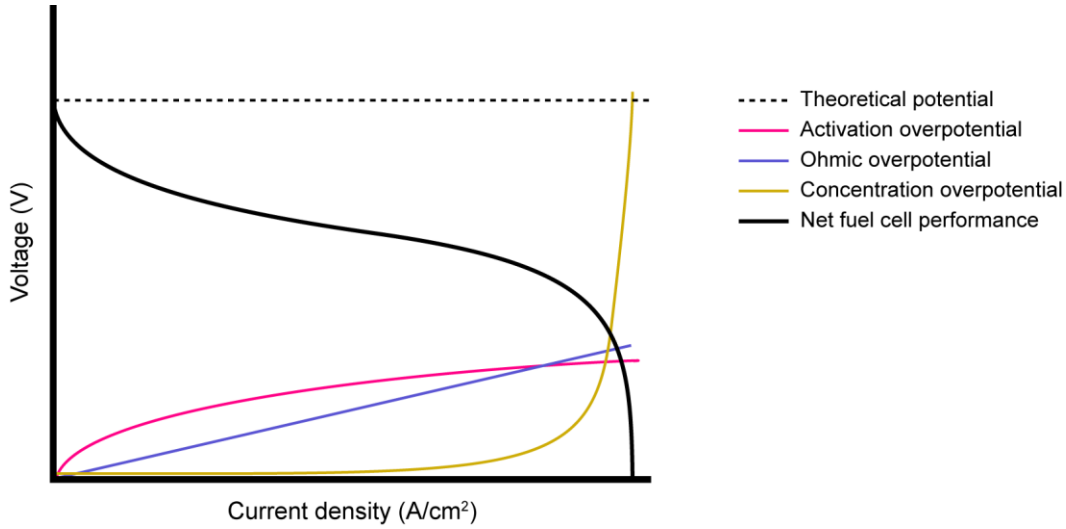

Figure 1.2 Schematic of a fuel cell polarization curve with major overpotentials. Net fuel cell performance is determined by subtracting various overpotential from equivalent potential (Nernst potential).

Figure 1.2 illustrates the overall fuel cell performance in practice showing the effects of the overpotentials to the voltage losses across the current density. The power density delivered by a fuel cell is the product of the voltage and current density (Figure 1.3). As a consequence of the voltage losses, the produced power per supplied fuel also decreases, *i.e.* the energy conversion efficiency decreases. Accordingly, reducing the overpotentials is critical to improve overall fuel cell performance.

Improving an electrode design by finding a better catalyst and geometrical structure can increase the electrochemical reaction rate occurring at the electrodes and reduce the activation overpotential. Sufficient porosity of the electrode structure is also essential for minimizing the mass transport losses to deliver adequate amount of reactants and continuously remove the products at the active sites. Lowering the ohmic overpotential due

to the ionic transport across an electrolyte can be obtained by reducing the thickness of a membrane.

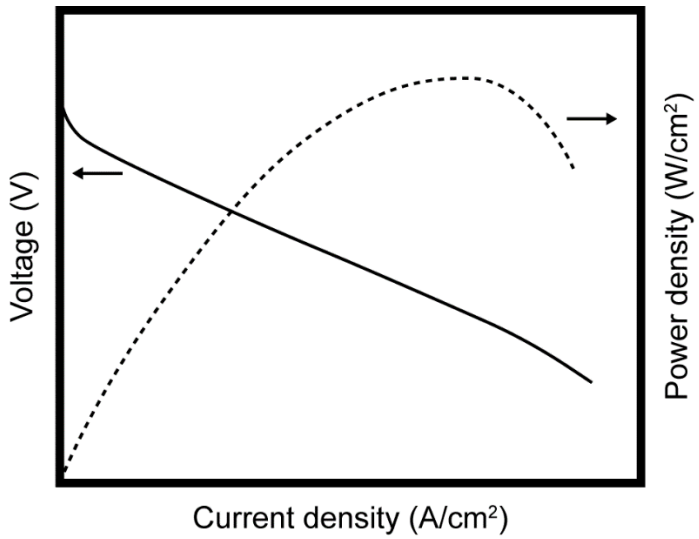

Figure 1.3 Relation of IV polarization and power density, which is determined by multiplying the voltage and current density at each point on the IV curve.

Different types of fuel cells are classified by the materials of electrolyte. Table 1.1 summarizes selective types of fuel cells.[5,6] While the general mechanisms of fuel cell operation are same across different types of fuel cells, charge carriers and operating temperatures vary with the types of electrolytes.

	Electrolyte	Operating temperature	Charge carrier	Fuel
PEMFC	Polymer membrane	20-120 °C	H_3O^+	H_2, CH_3OH
AFC	Liquid KOH	90-120 °C	OH^-	H_2
PAFC	Liquid H_3PO_4	150-200 °C	H^+	H_2
SAFC	Solid acid	200-300 °C	H^+	Hydrocarbons
MCFC	Molten carbonate	600-700 °C	CO_3^{2-}	Hydrocarbons, CO
SOFC	Solid oxide	500-1000 °C	O^{2-}	Hydrocarbons, CO

Table 1.1 Description of selective fuel cell types

1.2.2 Fuel cell advantages and disadvantages

As briefly discussed above, the advantages of a fuel cell are energy efficiency when in comparison to a combustion engine, and consistency of electricity production in comparison with a battery. Unlike a combustion engine, a fuel cell operates in a stationary state; it does not make noise during operation and has the potential of long-term operation. Also, toxic byproducts and smoke emission are not expected to be generated from a fuel cell. Comparing with a battery, a fuel cell can scale up both power and capacity independently, while a battery has a convoluted relation of power and capacity.[7]

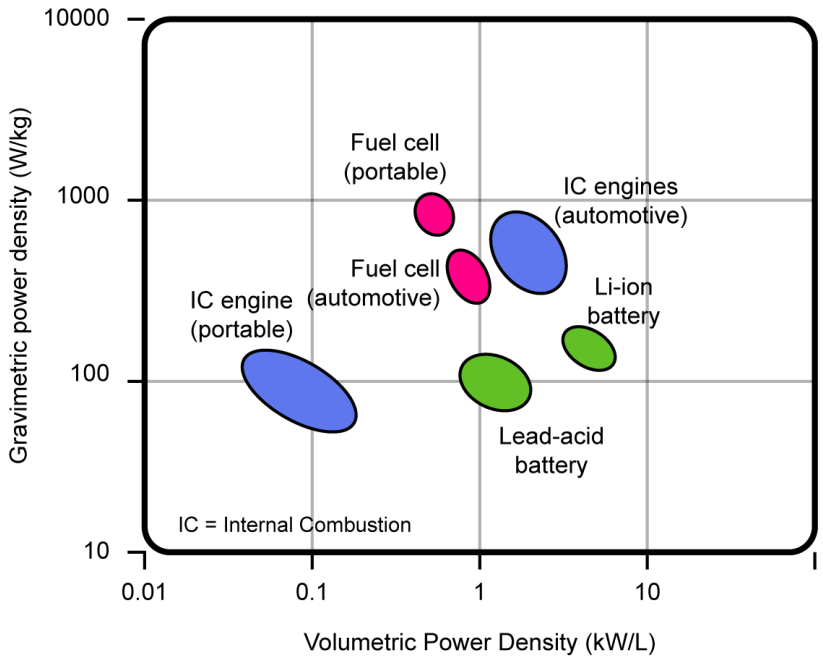

Figure 1.4 Power density comparison of selected technologies. Adapted from ref [7]

Although there are many attractive advantages in a fuel cell, there are still several disadvantages that a fuel cell needs to overcome. A major problem that a fuel cell encounters is a high upfront cost mainly from a precious-metal catalyst in a low temperature fuel cell and a complex fabrication for a high temperature fuel cell. Secondly, the achievable peak power density is still lower than what is achieved in competing systems. Figure 1.4 represents a comparison of volumetric power density with different technologies. In the case of a hydrogen fuel cell, fuel storage and availability are another barrier. Contrary to gasoline, infrastructure for hydrogen fuel transport is still poor, which impedes hydrogen fuel cell commercialization.

1.3 Electrocatalysis in fuel cells

1.3.1 Reaction kinetics

The activation overpotential relates to the reaction kinetics at the electrodes. Electrochemical reactions involve the electron transfer between an electrode surface and chemical species near the electrode surface. Electrochemical processes in fuel cell reactions only take place at the interface between an electrode and an electrolyte. As electrochemical reactions produce and consume electrons, flowing electrical current implies the rate of charge transfer under an assumption of 100% Faradaic efficiency. If an electrochemical reaction results in the transfer of *n* electrons, current will be expressed with the rate of an electrochemical reaction ν (mol/s) and Faraday's constant *F*,

$$i = \frac{dQ}{dt} = nF\frac{dN}{dt} = nF\nu \tag{1.9}$$

Integrating a rate gives the total amount of electricity produced, which relates to the number of moles of the material involved in the electrochemical process.

$$\int i\,dt = Q = nFN \tag{1.10}$$

In the electrochemical reaction, it is more common to use current density *j* (=*i*/A) than current *i*. This is because the maximum ion flux is limited by the cross-sectional area of the cell. Similarly, electrochemical reaction rate also can be expressed with area normalization:

$$J = \frac{1}{A}\frac{dN}{dt} = \frac{i}{nFA} = \frac{j}{nF} \tag{1.11}$$

with the unit of mol/cm^2.

The relations between activation overpotential η_{act} and current density j generated from the electrochemical reaction is expressed by the Butler-Volmer equation.

$$j = j_0 \left[e^{-\frac{\alpha \eta F}{RT}} - e^{\frac{(1-\alpha)\eta F}{RT}} \right] \approx j_0 e^{\frac{\alpha \eta F}{RT}} \tag{1.12}$$

Approximation is for large activation energy η_{act}. Here, j_0 is exchange current density which flows under zero overpotential (at the equilibrium), and α is exchange coefficient, expressing the electrochemical activity under non-zero overpotential with the value between 0 to 1. In order to increase the electrochemical current flow from the electrodes, the exchange coefficient and exchange current density needs to be larger. There is not much way to control the exchange coefficient which determined by the material itself property. As an exchange current density defines the current density equally flows in forward and reverse reaction at the equilibrium, it can be increased by (1) increasing the reactant concentration, (2) increasing the temperature, (3) increasing the number of reaction sites, and (4) decreasing the reaction activation barrier by employing appropriate catalyst. The last two methods can be improved by optimizing the electrode design.

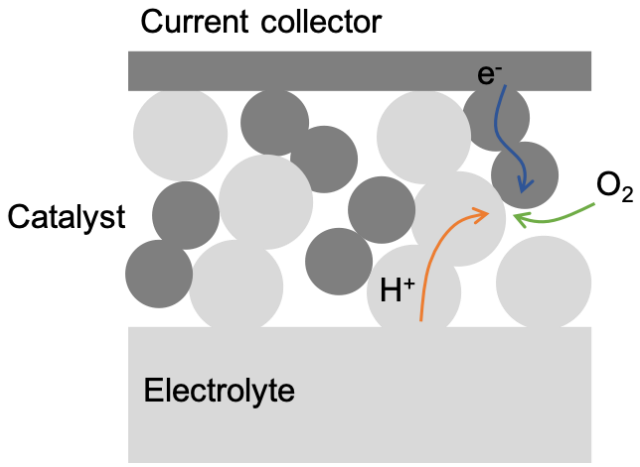

Figure 1.5 Schematic of a composite electrode and possible pathways of electron, ion and gas species at a cathode.

To increase the number of reaction sites, the spots where gas phase, electrically conducive catalyst, and ionic conductive electrolyte meet together, need to be increased. These sites are often called triple-phase boundaries (TPBs). As the electrochemical reaction involves the gas phase species, electrons and ions, an electrode structure requires interconnected ionic, electronic, and gas pathways. Thus, porous nanostructured composite of electronic conductive catalysts and ionic conductive electrolyte is generally employed for a fuel cell electrode (Figure 1.5).

In order to find the right catalyst for a given electrochemical reaction, the Sabatier principle would be one way to provide a helpful guide to discover new catalysts. It states that the interaction between the catalyst and the reaction chemical species should be neither too strong nor too weak. If the interaction is too weak, the reactants will not bind to the catalyst, while too strong interaction leads to blocking of sites as adsorbed particles are slower to dissociate. Catalytic activity is quantified as turnover frequency (TOF), which is the rate of

reaction per individual catalytic active site. The Sabatier principle can be expressed by plotting the TOF or activity versus adhesion strength, called the volcano plot (Figure 1.6). When different catalyst materials are plotted together, a volcano-type curve is produced, showing the maximum on catalytic activity presents at the intermediate adhesion strength between a reactant and a catalyst surface. As the adhesion strength can be calculated using quantum mechanics, volcano plots are regularly reproduced and predicted by density function theory (DFT) calculation.[8]

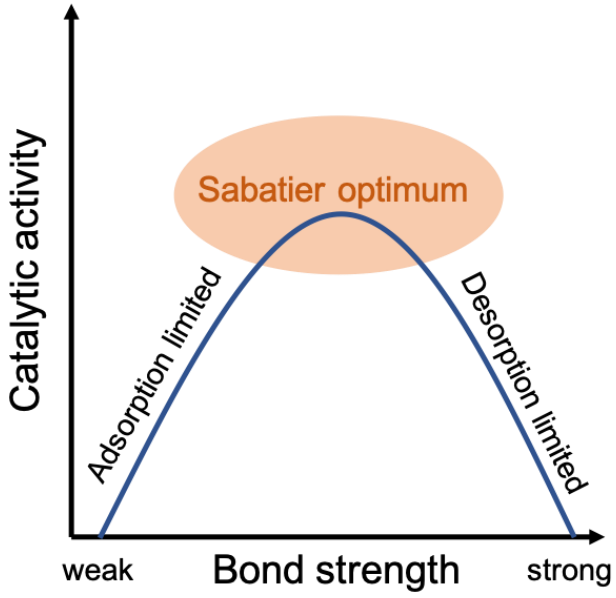

Figure 1.6 Schematic of a typical volcano plot determined by the Sabatier principle.

1.3.2 Hydrogen electro-oxidation and oxygen electro-reduction

Reaction kinetics vary with the type of electrochemical reaction and catalyst. Sluggish reaction kinetics lead to a large activation overpotential. In the H_2/O_2 fuel cell

system, the kinetics of hydrogen oxidation reaction are extremely fast, while the kinetics of oxidation reduction reaction are slow. For example, in the polymer membrane fuel cell system, the exchange current density for hydrogen oxidation reaction at smooth surface of Pt is reported as 10^{-3} A/cm^2, while the one for oxygen reduction reaction at the same catalyst is reported as 10^{-9} A/cm^2, which is six orders of magnitude lower.[7,9] Slower oxygen reduction reaction vis a vis hydrogen oxidation comes the fact that oxygen reduction requires more complicated steps and substantial molecular reorganization.

1.4 Solid acid fuel cells

1.4.1 Introduction of SAFC

Solid acid fuel cells (SAFCs) are a relatively new type of fuel cell, that employ purely protonic conductive solid materials, so called solid acid compounds, as electrolytes. Solid acid compounds, based on tetrahedral oxyanion groups, have characteristics of both salts and acids, meaning that they can dissolve in water and donate the protons. Even before solid acid compounds were explored as electrolytes of fuel cells, these compounds have been studied over thirty years. Some of solid acids have shown superprotonic phase transitions in which the ordered hydrogen-oxyanion structure at room temperature undergoes structural transition to highly disordered hydrogen bond network at 100-300 °C, showing high proton conductivity typically in ~10^{-2} S/cm.[2,10]

The most common solid acid compound for a fuel cell electrolyte is cesium dihydrogen phosphate (CsH_2PO_4). It shows a superprotonic transition at 228 °C under 1 atm

pressure, with a polymorphic phase transition from monoclinic to cubic structure (Figure 1.7). As with other solid acids, CsH_2PO_4 also tends to be dehydrated at high temperature and decomposed to $CsPO_3$ and H_2O.[11]

$$CsH_2PO_4 \rightarrow CsPO_3 + H_2O \quad (1.13)$$

This reaction is more favorable at the superprotonic phase, losing the protonic conductivity consequently.[12] Suitable water partial pressure impedes the dehydrating reaction by forcing the (1.9) reaction toward the left.[2,13] Figure 1.8 describes the relation between temperate/water partial pressure and dehydration behavior of CsH_2PO_4. This graph provides the window for proper condition for fuel cell electrolyte.

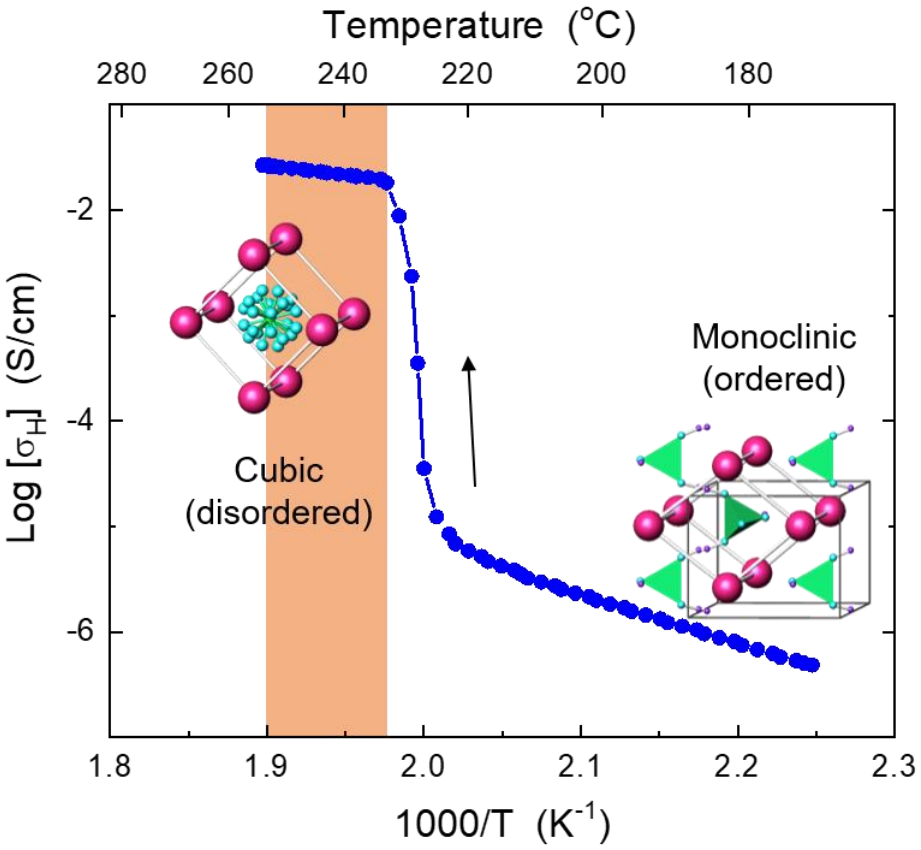

Figure 1.7 Superprotonic phase transition in CsH_2PO_4 and corresponding crystal structures. Pink spheres represent Cs atoms, blue spheres represent O atoms, purple spheres represent H atoms, and green tetrahedrons represent PO^{4-}s. Fuel cell operating temperature range is indicated by orange colored shade.[2,6,14]

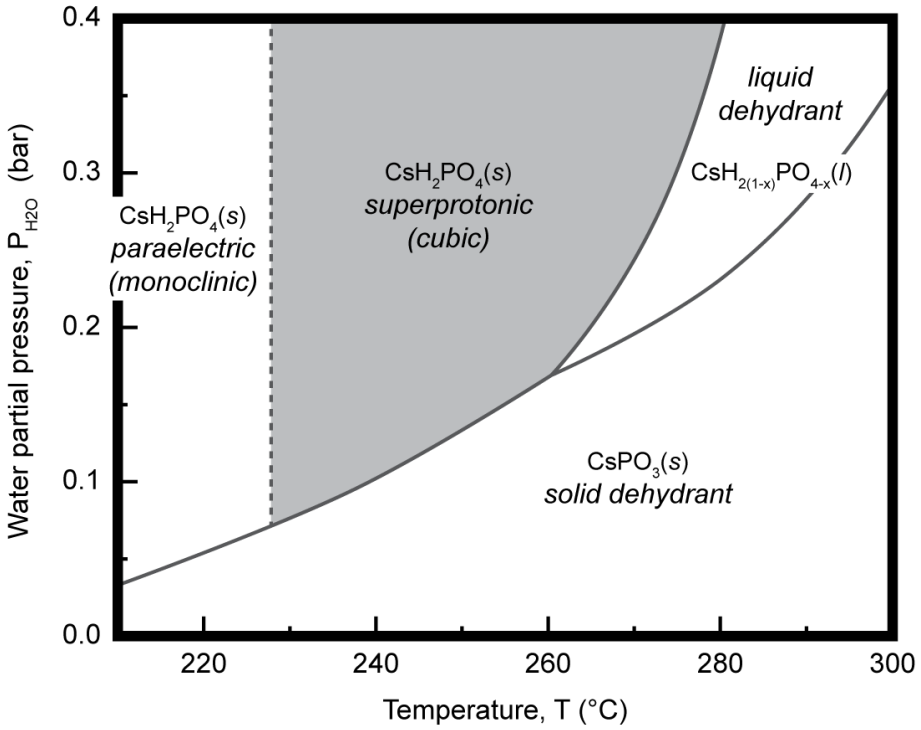

Figure 1.8 Phase diagram of CsH_2PO_4 indicating the region of stable phase for a fuel cell operation.[10]

Accordingly, the operating temperature of CsH_2PO_4 based SAFCs is 230-280 °C under ~0.4 atm water partial pressure. As an intermediate temperature fuel cell, SAFC has the combined advantages of a high temperature fuel cell, which has fuel flexibility and high efficiency, and a low temperature fuel cell, which has inexpensive auxiliary components and easy on-off cycling. With Pt catalysts, SAFCs have shown a peak power density of ~200 mW/cm^2 when operated under humidified H_2/Air condition at 250 °C [15] and as high as 415 mW/cm^2 under humidified H_2/O_2 [4] with significantly stable performance over several hundred hours. It also has shown fuel stream impurity tolerance toward CO, H_2S, NH_3, CH_3OH, C_3H_8, and CH_4 as well as fuel flexibility for reformed hydrocarbons.[10,16] In case of

a polymer membrane fuel cell, the exposure to those impurities in ppm level is detrimental to the cell performance.[17]

Despite the impressive data on performances of SAFCs, high Pt loading at the electrodes (~2 mg_{Pt}/cm^2 in total) for lowering the activation overpotentials hampers the economics of commercialization due to its high cost and price volatility. We can achieve a decrease in the cost per unit power output from SAFCs by decreasing the materials costs and by increasing the fuel cell powder density.

One of the efforts toward increasing the power output has done is decreasing the electrolyte thickness 25μm and reducing down the electrolyte area specific resistance to 0.11 $\Omega\ cm^2$.[4] However, as shown in many IR-corrected polarization curves with subtracted ohmic resistance contribution, significant overpotential over the fuel cell behavior is not from the electrolyte ohmic resistance, but more likely from a slow electrocatalysis rate at the electrode.

1.4.2 Progress on SAFC performance

Another approach to improving the power output is by introducing Pd as a catalyst for the cathode.[10] Figure 1.9 shows peak power density reaches as high as 600 mW/cm^2 with $Pt_{0.2}Pd_{0.8}$ alloy. Pd catalyst has shown advanced catalytic activity for both hydrogen oxidation reaction and oxygen reduction reaction compared to conventional Pt catalyst in SAFC systems.[10,18-20] However, the Pd-based catalyst reacts with CsH_2PO_4 under operating condition at the cathode, causing poor electrode stability.[10,19,20]

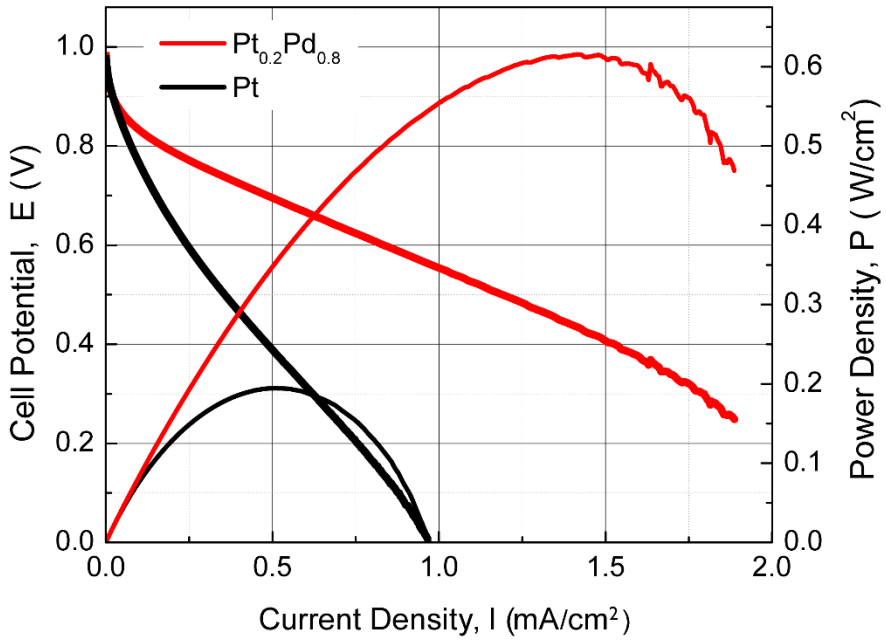

Figure 1.9 Polarization and power density curves for SAFCs with Pt and $Pt_{0.2}Pd_{0.8}$ cathode catalysts. Anode catalyst is Pt in both cells.[10]

Increasing the number density of catalyst sites could also impact on the power density output. The mixture of CsH_2PO_4 particles and electronically conductive catalyst materials composes the electrode of SAFCs, providing the paths of proton and electron respectively. Unlike polymer electrolyte based or liquid electrolyte solution-based fuel cells, where the electrolytes are already gas permeable, active sites for electrochemical reaction in SAFCs are limited to where the catalyst, CsH_2PO_4, and pore are present all together (triple-phase boundary).[21] Therefore, reducing the size of CsH_2PO_4 particles in the electrode notably improve the overall fuel cell performance by increasing electrode-electrolyte contact area and effective charge transfer resistance.[10]

In addition to controlling the size of CsH_2PO_4, new strategy of depositing a porous Pt thin film directly on the CsH_2PO_4 through metalorganic chemical vapor deposition method

(MOCVD) has been invented to increase the triple phase boundary at the cathode. This allows almost all of CsH_2PO_4 surface to be active for electrochemical reaction as well as provides electron path way networks. Furthermore, employing the MOCVD method has cut down the total Pt loading at the cathode to < 1.75 mg_{Pt}/cm^2 from 4-8 mg_{Pt}/cm^2 of the electrode fabricated by mechanically mixing the CsH_2PO_4 particles and Pt black (or Pt on carbon).[21]

Further effort to reduce the Pt loading at the anode has been done by introducing an electrospray deposition in order to construct porous nanostructured composition electrodes.[22] Water-methanol solution of CsH_2PO_4, catalytic additive (Pt black, Pt on carbon or carbon nanotube), and polyvinylpyrrolidone (PVP) is electro-sprayed onto a substrate, forming an interconnected composite with a high porosity and surface area. With this method, Pt loading at the anode has been reduced down toward 0.3 ± 0.2 mg_{Pt}/cm^2, which is 30 × decrease relative to mechanically milled electrode with comparable activity.

After developing an electrospray deposition technique, subsequent studies have been conducted toward reducing the Pt loading as well as improving the Pt utilization (defined as the area specific electrode conductance, S/cm^2, divided by the Pt loading, mg/cm^2) at the anode of SAFC. A Solution of CsH_2PO_4 and Pt catalysts (Pt nanoparticles, or Pt on carbon) is directly deposited onto carbon nanotube-overgrown carbon paper by electrospraying to form a highly porous, fractal structural composites.[23] Afterwards, Pt decorated carbon nanotubes are synthesized and introduced into a CsH_2PO_4-based solution and electrosprayed onto carbon paper in order to enhance the interconnects of electron, proton pathways with utilization of all deposited Pt catalysts.[24] As a result, total Pt loading at the anode is just 0.014

mg_{Pt}/cm^2 and Pt utilization is ~80 S/mg, an order of magnitude over the milled composites electrode.

Besides the Pt-based catalyst, investigations exist regarding alterative metal catalysts for the electrodes in SAFC system with the purpose of replacing the high cost Pt catalyst. Ni nanoparticles have shown reasonable catalytic activity for hydrogen evolution reaction, while the hydrogen oxidation activity is nearly absent.[25] On the other hand, Ru nanoparticles have shown excellent tolerance to CO and the catalytic performance for the hydrogen oxidation reaction comparably to those with Pt-based anode.[26]

C h a p t e r 2

EXPERIMENTAL METHODS

2.1 Catalyst deposition

2.1.1 Sputter deposition

Typical electrodes of electrochemical cells have 3-D geometries that maximize triple-phase site and porosity, but this method leads to some challenges in systematic studies. In order to alleviate these complications, thin film electrodes are implemented for systematic electrocatalyst study.[18,27-30] DC sputtering is a common thin film fabrication technique, that consists of depositing a metal thin film on a substrate. The sputtering process involves ejecting materials from the solid surface of a target of interest by the bombardment of energetic ions, usually Ar, on the target surface.

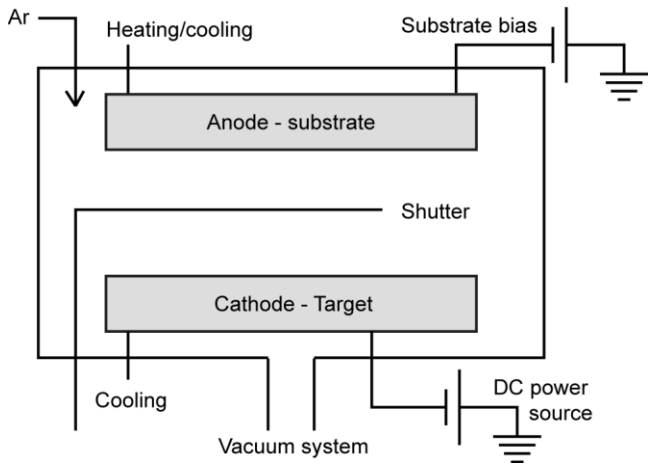

Figure 2.1 Schematic of a DC sputtering system. Adapted from ref [31]

Figure 2.1 shows a schematic of a DC sputtering system. The metal target is placed at the cathode, which has high negative voltage, and a substrate, where the metal film should be deposited on, is mounted on the anode. Sputtering is carried out in a vacuum chamber with the presence of Ar gas kept in low pressure, a few mTorr. By applying a potential between two electrodes in the presence of Ar gas, free electrons are accelerated away from the cathode and collide with Ar atoms, creating plasma with Ar^+ ions. Positive ions are accelerated into a cathode, striking the surface of a target and ejecting target atoms mostly in the form of neutral particles, as well as more free electrons. Ejected target atoms travel straight in random directions, and some of them arrive at the substrate, forming a thin film. Meanwhile, some of free electrons keep generating the Ar^+ ions by collisions, and some of them recombine with the positive Ar^+ ions, releasing photons.

Morphology of deposited film differs depending on the sputtering conditions, such as working pressure, substrate temperature and bias voltage at the substrate.[32] Kinetic energy of sputtered particles plays a key role in the film growth and crystallization, determining the diffusion and mobility of the atoms adsorbed on a substrate surface.[33] Gas pressure effects on the kinetic energy of sputtered particles by varying the chance of collision with other particles while traversing to a substrate. Substrate temperature changes the kinetic energy of the adatoms on a substrate, where its temperature can also rise by the bombardment particles hitting the substrate, transferring the kinetic energy to thermal energy. For example, with higher Ar pressure and lower substrate temperature, deposited film tends to grow in a columnar structure with porous morphology.[34] As bias voltage accelerates the electrons or

ions toward the substrate, it also influences the behavior of film growth as well as the film properties.[32]

2.1.2 Metalorganic chemical vapor deposition

In SAFCs, carbon should be avoided in the cathode composition because carbon reacts with oxygen under operating condition and results in the cell degradation.[35] As a consequence, instead of using standard metal nanoparticles on carbon, a few nanometers thickness of metal film is deposited on the surface of CsH_2PO_4 particles through chemical vapor deposition and lightly pressed to create a porous structure with interconnected protonic and electronic conduction pathways. Two different state-of-the-art techniques of metal deposition onto CsH_2PO_4 powder have been used: one is metalorganic chemical vapor deposition (MOCVD) [21] and the other is atomic layer deposition (ALD),[15] which will not enter the further discussion here.

MOCVD is a well-established deposition technique used to grow a thin film with high purity through heterogenous chemical reactions. Film growth relies on the transferring of gas phase from a precursor to a solid substrate surface. Decomposing the precursor requires a high temperature. As the MOCVD technique does not involve any aqueous solution processing, it is suitable for depositing films on the surface of CsH_2PO_4, which is soluble in water.

In typical process of MOCVD, a substrate of interest is exposed to a volatile metal precursor, followed by decomposing or reacting of precursor on the substrate surface and forming a film. After the reaction the byproducts, which are usually also volatile, are purged

out by flowing gas. It is generally preferable to keep in vacuum before the deposition in order to reduce the undesired reactions caused by other gas phase reactions and improves the film homogeneity. Depending on the purpose, plasma can be introduced in the deposition step to improve the film growth rate and crystallization.

MOCVD technique used for SAFC application is conducted by the following steps. First, the metal precursor is milled together with CsH_2PO_4 particles and heated in a fixed-bed at low pressured reactor filled with N_2 gas and water vapor in order to prevent the dehydration of CsH_2PO_4. Then, a thin metal film is coated on CsH_2PO_4 surface in a closed reactor as a consequence of vaporization and decomposition of the precursor. After finishing the reaction, the reactor is purged out with N_2 gas before taking out the metal coated CsH_2PO_4 powder. This method has been implemented for fabricating cathode composites for the facile and low-cost applications. However, there is the problem of organic precursor residue remaining in the composite, which cause the cathode to degrade in performance over time. Several new attempts have been tried to improve the purity of the metal film by removing the organic residues.

2.1.3 Solution deposition

The carbon supported metal nanoparticles are prepared by solution reduction deposition. The solution deposition technique is advantageous for the substrate having porous and complex geometry as long as it is stable and dispersible in aqueous solution. One benefit of this technique is that it does not require elaborate experimental equipment. High surface carbon powder is immersed in a solution containing metal ions and a reducing agent

is added in to the solution afterward. Simultaneous reactions between metal ions and reducing agent lead to simultaneous metal nanoparticle formation and stabilization on the surface of carbon support. The kinetics of electron transfer from a reducing agent to a metal ion is necessary to be slow, otherwise it would be possible to reduce the metal ion in the bulk solution.[36] As bath temperature, concentration of the metal ions, pH, and stirring speed control the deposition rate and properties of deposited metal,[37] optimizing the deposition conditions for each type of metal is necessary for yielding the desired properties of metal particles.

2.2 Electrochemical cell geometry

2.2.1 Symmetric cell

One of the typical ways to probe the electrocatalysis at an electrode of an electrochemical cell is characterizing a symmetric cell. In this context, symmetric cell means a cell consisting of two electrodes with identical geometry/compositions at both sides of an electrolyte and operating under uniform gas environment (Figure 2.2 (a)). This technique has several advantages over traditional fuel cell geometries. Unlike in a fuel cell configuration, where both anode reaction and cathode reaction occur spontaneously, half-cell reaction of interest can be isolated from the other. In addition, building a cell test station is relatively easy. By using a single chamber, it is possible to eliminate the difficulty in sealing two separate gas compartments since a uniform gas environment is applied to both sides. As electrochemical potential does not exist across the cell, impedance analysis (which will be

discussed later) at the open circuit voltage, provides the information of a gas reaction at the equilibrium state, $H_2 = 2H^{2+} + 2e^-$ for the anode reaction, and $H_2O = 2H^+ + 2e^- + ½O_2$ for the cathode reaction.

Symmetric cell studies, however, do not deconvolute the forward and reverse reactions. Probing only one direction of interested reaction, such as hydrogen oxidation reaction and oxygen reduction reaction is rarely possible from this geometry.

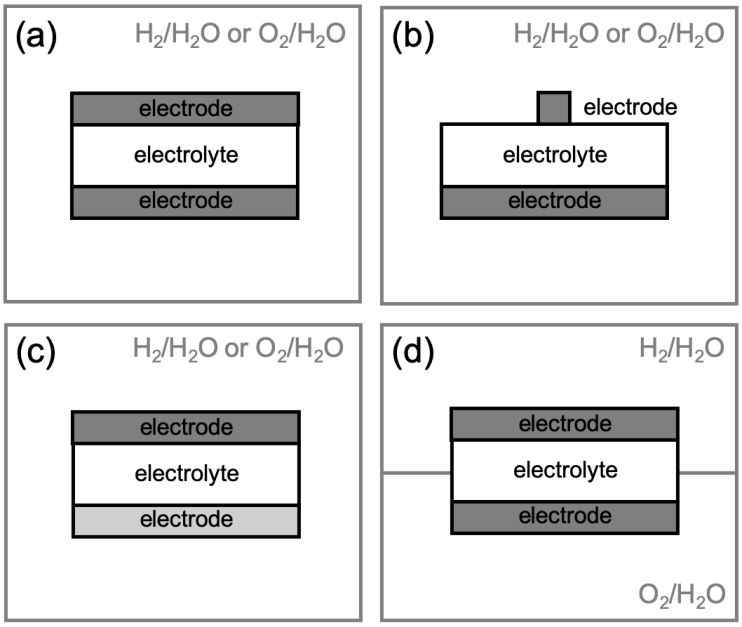

Figure 2.2 Schematics of electrode design and gas environment for solid state electrochemical measurements: (a) symmetric electrode in a uniform gas environment, (b) asymmetric electrode geometry in a uniform gas environment, (c) asymmetric electrode catalyst in a uniform gas environment and (d) symmetric electrode geometry in asymmetric gas environment.

2.2.2 Asymmetric cell

To overcome the limits of the deconvolution of two reactions from the symmetric cell study, asymmetric cell studies are also widely conducted. There are two type of

asymmetric cell measurements, one is evaluating a cell in a uniform gas environment with asymmetric electrodes (Figure 2.2 (b, c)), and the other one is measuring a cell under asymmetric gas environment using dual chambers (Figure 2.2 (d)).

To separate the forward and reverse reaction in a uniform gas environment, DC bias needs to be applied across a cell to induce a reaction of interest to occur at a working electrode and corresponding reaction at a counter electrode. With this condition, reducing the area of a working electrode leads the resistance of the counter electrode negligible by comparison which leads to the working electrode dominating the detected response (Figure 2.2 (b)).[14,28] Another way to have asymmetric electrodes configuration is preparing a cell with a counter electrode comprised of catalysts with higher activity or higher active site density than the catalyst at a working electrode, as figure 2.2 (c) presents. As with the previous configuration, the working electrode prevails the total electrode response of a cell. The downside of this cell design is that it has limitations when studying relatively low activity catalysts.

Although studying an electrochemical cell under the uniform gas environment has several advantages, evaluating the overall fuel cell performance by preparing a full cell and placing it between two gas chambers are mostly carried out for cathode material studies. As the majority of activation loss in a fuel cell is from the cathode having slow kinetics for the oxygen reduction reaction, the overpotential from the anode is negligible. Cathode catalytic behavior can be analyzed under representative conditions of fuel cell operation. In addition, fuel cell measurements are advantageous to study a cathode catalyst containing Pt, which is tricky to study in symmetric cell configuration under humidified oxygen by reason of the formation of PtO near the open circuit voltage.[38,39]

2.3 Electrochemical cell test stations

Two types of electrochemical cell test stations are used for a study of electrocatalysis in SAFCs system. Electrochemical properties of symmetric cells are characterized in a single chamber with a uniform gas environment. In fuel cell measurements, on the other hand, each electrode is exposed to different gases; one side is the reducing gas and the other side is the oxidizing gas. Unlike in a symmetric cell test station, gas sealing between the two electrodes is crucial to avoid gas leakage for a fuel cell test station.

Figure 2.3 and Figure 2.4 illustrate schematic of test stations used for *in-situ* electrochemical cell characterization. Basic components of cell test station for a symmetric cell and a fuel cell are same. Major differences between two stations are number of bubbler and design of cell holders. Each gas passes through a digital mass flow controller, which is calibrated by a gilibrator in advance, enters to a water bubbler heated at 75 °C to subjoin a sufficient amount of steam. The resulting humidified gas is delivered to an electrochemical cell through the gas line heated at 150 °C to keep water from condensing in the line. For a symmetric cell, reactant gas goes into a single cylinder chamber where a cell is located and leaves to the outlet. Before downstream gas leaves to the ventilator, water vapor condenses in a room-temperature bubbler, which also monitors gas flow. For a fuel cell test station, two humidified gases are delivered separately to each side of a cell and then go to the exhausts.

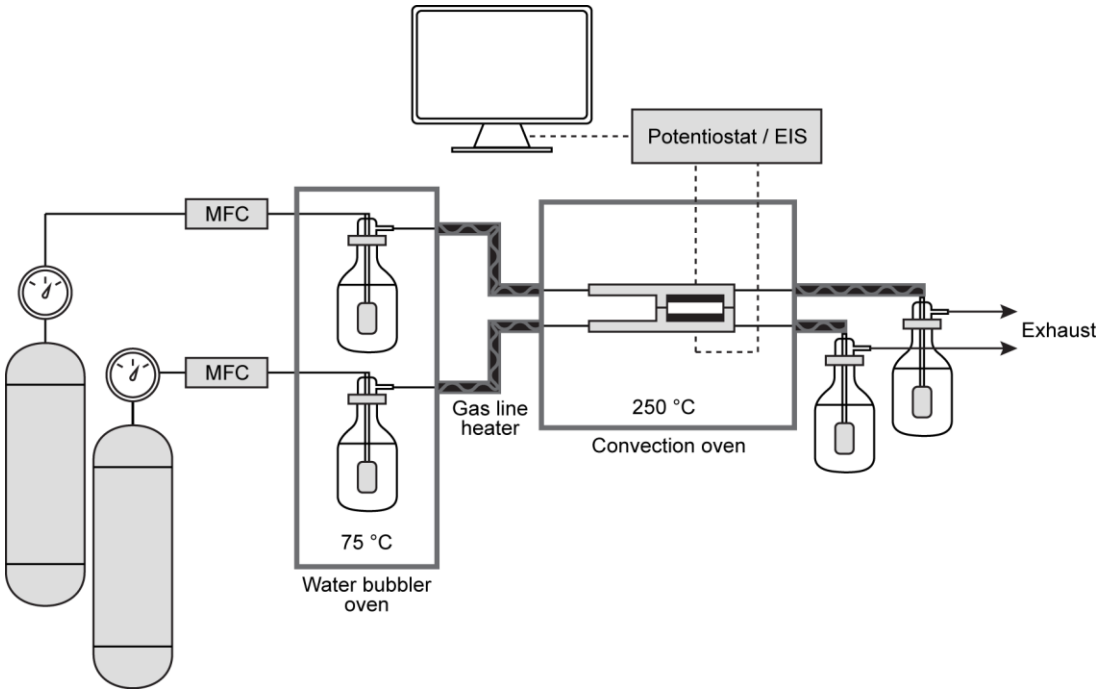

Figure 2.3 Schematic of test station for a fuel cell measurement.

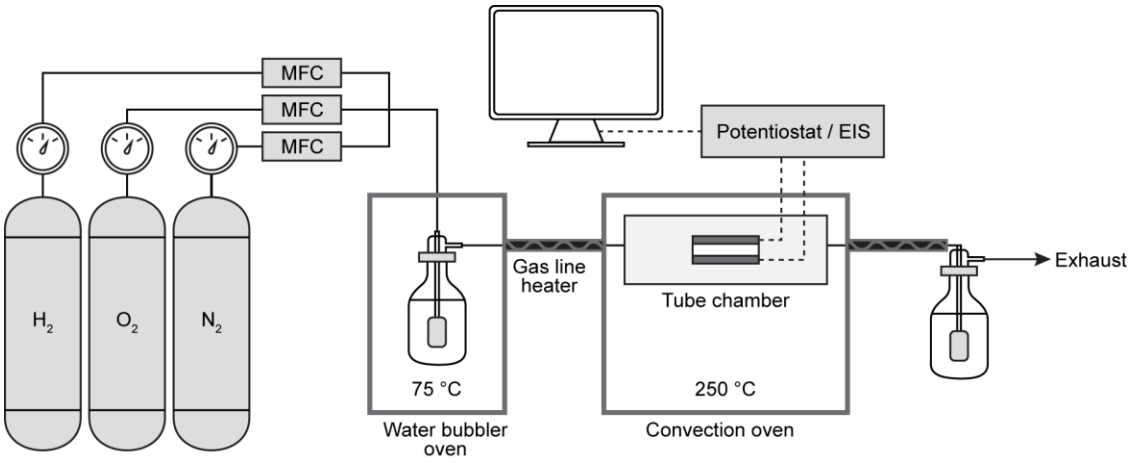

Figure 2.4 Schematic of test station for a symmetric cell measurement.

As a CsH_2PO_4 based electrochemical cell operating temperature is 230-250 °C,[10] a cell is placed at the set of test fixtures and heated up in a convection oven with careful monitoring of cell temperature using a thermocouple probe attached near to a cell. Two silver wires are attached on each side of electrode in a pseudo four-point probe configuration (Figure 2.5). With this method, ohmic contribution from the silver wire is removed from the electrochemical cell measurement. However, the inductance signal is unavoidable from the AC impedance measurement at a high frequency range and further data correction is necessary. One way is by performing a short-circuit correction, in which measuring the impedance response of shorted cell holders by contacting together without a cell and using the short correction measurement data to subtract the inductor response from the experimental data. Another method is accounting for an inductor element in an equivalent circuit model, which will be discussed in the next section.

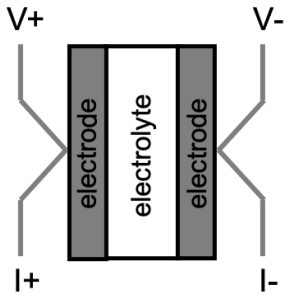

Figure 2.5 Schematic of pseudo four-point probes configuration.

2.4 Electrochemical cell characterization

2.4.1 DC current-voltage measurement

The most ubiquitous technique for electrochemical cell characterization is the current-voltage measurement, providing an overall evaluation of a cell performance. Regarding current-voltage measurement, there are two types of techniques, one is potentiostat and the other one is galvanostat. The potentiostat controls the voltage of a system and measuring the resulting current response. The galvanostat, on the other hand, controls the current of a system and measuring the resulting voltage response. In fact, either technique yields the identical I-V curves in steady state. However, when a system does not have enough time to relax to its steady state, potentiostat and galvanostat measurements may deviate. This behavior is commonly observed from the current interrupt measurement, which exceeds our discussion here.

Generally, an electrochemical cell is characterized by current-voltage measurement in two ways. The overall overpotential over different current densities is analyzed by drawing a polarization curve. To avoid overestimated measurement, scan speed should be slow enough to reach a pseudo steady-state condition[7]. If the scan speed is too fast, the IV curve will be shifted to the higher voltage. Whereas, the long-term stability of a cell performance is assessed by applying a constant current to a system and recording a resulting voltage response with time. It also can be performed by monitoring the current response over the constant given voltage. If the overpotential of a cell increases with time, increment of voltage (or decline of current in potentiostatic mode) will be observed.

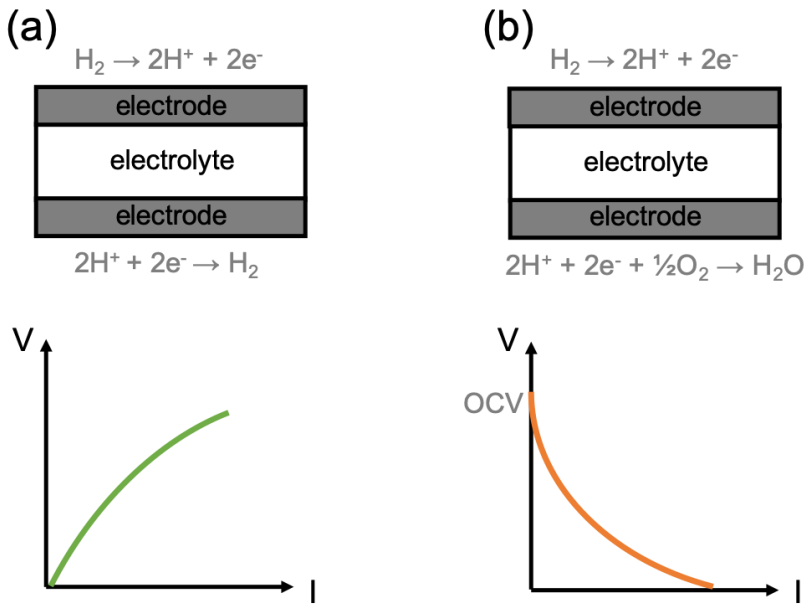

Figure 2.6 Schematics of electrochemical cells with half-cell reactions and polarization curves for (a) a symmetric cell and (b) a fuel cell.

The behavior of polarization curves for a fuel cell and a symmetric cell appear differently. As described above, a symmetric cell is measured in a uniform gas environment, either oxidizing or reducing condition. As an electrochemical potential gradient does not exist at open circuit voltage, one should apply an electric field to the cell to drive the electrochemical reaction. For instance, anode | electrolyte | anode cell in a uniform humidified hydrogen environment, drawing a polarization curve induces one side is hydrogen oxidation reaction and the other side is proton reducing reaction simultaneously (Figure 2.6 (a)). If the area of both electrodes is identical, the slope of the polarization curve is from the combination of hydrogen oxidation/proton reduction responses. However, if the area of one electrode is smaller than the other one, the electrode response from the larger

area is negligible, and consequentially the slope of the polarization curve is mainly from the reaction occurring at the smaller electrode as the reaction rate scales with the area.[28]

In a fuel cell configuration, an anode is exposed to reducing condition and a cathode is exposed to oxidizing condition (Figure 2.6 (b)). When a cell is in an equilibrium condition, the open circuit voltage is close to the theoretical value defined by Nernst equation. A polarization curve obtained with a slow scan reveals the overpotential behavior over the current density. Separating the various loss contributions is challenging, yet careful data analysis yields valuable information. Losses at low current densities arise predominantly from activation losses. In the case for the H_2/O_2 fuel cell, the slow oxygen reduction reaction dominates activation losses. Further voltage drops as load current increases is a result of ohmic loss and mass transport loss contributes when fuel consumption exceeds fuel supply. Open circuit voltage is also used as an indicator of sealing the two champers to ensure the separation of two gas environment. Overall fuel cell performance and its stability are evaluated through repeated polarization curve measurements over time.

2.4.2 AC impedance spectroscopy

Unlike a polarization curve measurement, where the deconvolution of the various overpotentials is challenging, impedance spectroscopy is a powerful technique for distinguishing the different loss contributions in an electrochemical cell. It allows for the separation of individual components of losses in a frequency domain and identify them through a well-controlled experiment.[40,41]

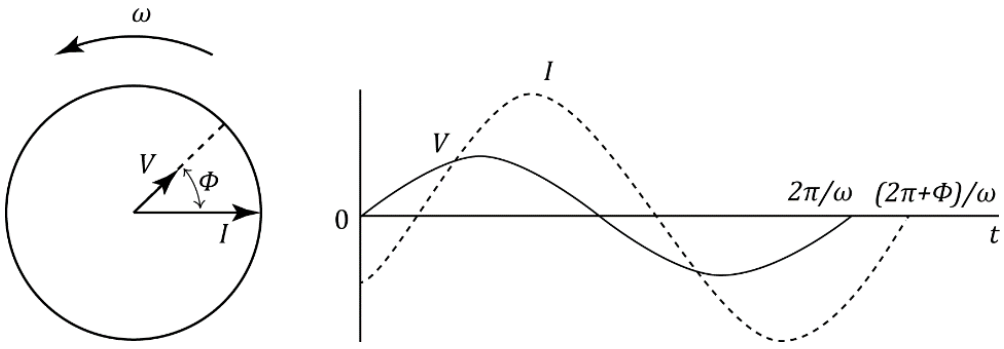

Figure 2.7 Phasor diagram describing the relationship between sinusoidal voltage and responding current at frequency ω. Adapted from ref [42]

Similar to resistance, impedance describes the ratio between voltage and current as a function of frequency. Impedance measurements are conducted by applying a small sinusoidal voltage perturbation to a system and recording the resultant current response or applying a sinusoidal current perturbation and recording the voltage response. Sinusoidal voltage and current at time *t* are expressed as

$$V(t) = V_0 e^{i\omega t} \tag{2.1}$$

$$I(t) = I_0 e^{i(\omega t+\phi)} \tag{2.2}$$

where V_0 and I_0 are the amplitudes of the voltage and current, ω is the radial frequency, and ϕ is a phase shift from the current response (Figure 2.7). With these definitions, impedance can be written in terms of a real and an imaginary component:

$$Z(\omega) = \frac{V(t)}{I(t)} = Z_0 e^{-i\phi} = Z_0 cos\phi - iZ_0 sin\phi = Z' - iZ'' \tag{2.3}$$

The impedance of a system can expressed with an impedance magnitude Z_0, and a phase shift ϕ, or a real component ($Z' = Z_0 cos\phi$) and an imaginary component ($Z'' = Z_0 sin\phi$). Mostly, impedance data are plotted in a Nyquist plot, where Z' is on the x-axis and $-Z''$ is on the y-

axis. This plot is useful to visualize the different electrochemical processes taking place in different characteristic timescale represented in separated arcs along the x-axis. [42]

Impedance measurement on an electrochemical cell allows to investigate activation loss, ohmic loss and mass transport loss by comparing with an equivalent circuit model. For instance, ohmic electrolyte loss can be expressed with a resistor R as a simple resistor, which does not have imaginary component. Nyquist plot for a resistor is appeared as a single point on the real axis.

The equivalent circuit for an electrochemical reaction is represented in more complicated way. Typically, electrochemical reaction interface is modeled as a parallel combination of a resistor and a capacitor. Resistor describes the kinetic resistance of an electrochemical reaction. Capacitor represents the nature of charge separation across the reaction interface, where electron accumulation in the electrode matches ion accumulation built up in the electrolyte. The charge separation of ions and electrons placed at the interface acts like a capacitor and reaction kinetic of an electrochemical reaction behaves like a resistor. When the interface between an electrode and an electrolyte is not perfectly smooth but has rough surface or porous, constant phase element Q (CPE in ZView software) is used instead of C capacitance and composes a RQ circuit.[41] Table 2.1 describes the difference of a constant phase element and a capacitor is an exponent element *n,* where the value of n is between 0 to 1.

When the electrochemical reaction involves the diffusion rate-limiting step by a reactant species, which is related to a mass transport, Warburg element is introduced to an equivalent circuit.[43] If the thickness of the diffusion layer is infinite, Infinite Length Warburg,

W is used to represent the species diffusing into a layer at low frequencies. If a diffusion layer is thin, low frequencies will penetrate the entire layer, creating a boundary. On the basis of the type of the boundary, either Finite Length Warburg (FLW) for short circuit terminus (W_s), or for open circuit terminus (W_o) are used. First one is for reversible boundary, where a system acts like a resistor at low frequencies, which is commonly observed in a fuel cell. The second one, on the other hand, is for irreversible boundary, where a system acts as a capacitor at low frequencies, which is easily observed in a Li-ion battery. The characteristic feature of a Warburg element in a Nyquist plot is a straight line at high frequencies. As the expression of Warburg element has a diffusion time τ ($\tau = L^2/D$, where L is the effective diffusion thickness and D is the effective diffusion coefficient), diffusion coefficient for a reactant species can be calculated by fitting the impedance data with a Warburg element.

Lastly, another element that commonly observed in an experimental system is an inductor, L. As described in Chapter 2.3, an electrochemical cell test station has electrical wires attached to a cell. These wires act like an inductor, appearing as a long vertical line along the positive imaginary Z" axis at high frequencies in a Nyquist plot. Because of the inductor element, it is easy to overestimate the ohmic resistance as well as reading a shifted characteristic frequency unless the appropriate equivalent circuit is well fitted. Twisting the wires each other could help to reduce the inductance.

Table 2.1 summarizes the mathematical expression for each equivalent circuit element. Although there are more equivalent circuit elements, these elements are enough to explain most of electrochemical cell behaviors here. With a careful and logical construction of an equivalent circuit for a cell to be analyzed, individual values, such as ohmic resistance

and electrochemical resistance are calculated by fitting the measured data. An example of a simple equivalent circuit composed of an inductor, an ohmic resistance and a RQ circuit representing an electrochemical reaction at an electrode with a resulting Nyquist plot is shown in Figure 2.8. For CsH_2PO_4 based anode symmetric cell experiments, typically two electrode responses are overlapped in one semi-circle arc at OCV as a result of comparable kinetic reactions of hydrogen oxidation reaction and proton reduction reaction.[28]

Circuit	Impedance Z(ω)
Resistor, R	R
Capacitor, C	$\frac{1}{i\omega C}$
Constant phase element, Q	$\frac{1}{Y(i\omega)^n}$
Inductor, L	$i\omega L$
Infinite length Warburg, W	$\frac{R_0}{(i\omega\tau)^n}$
Finite Length Warburg-short circuit, W_s	$R_0\frac{\tanh[(i\omega\tau)^n]}{(i\omega\tau)^n}$
Finite Length Warburg-open circuit, W_o	$R_0\frac{\coth[(i\omega\tau)^n]}{(i\omega\tau)^n}$

Table 2.1 Summary of common equivalent circuit elements

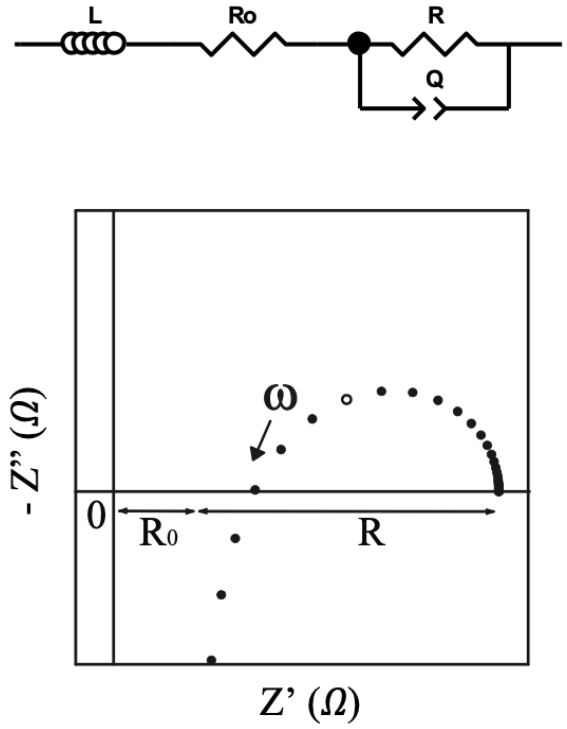

Figure 2.8 Example of a simple equivalent circuit and corresponding Nyquist plot with an indication of characteristic frequency (open circle), which is defined as 1/RC, located at the apex of a semi-circle of RC or RQ circuit. Inductor element shifts the position of a characteristic frequency as well as reducing the width of the semi-circle. Adapted from ref [14]

To characterize an electrochemical cell behavior over a range of current densities, AC impedance analysis also accompanies DC bias. By collecting the impedance response along the I-V polarization curve, contribution of different losses emerges, as described in Figure 2.9. For instance, at near open circuit value, impedance response relating to activation kinetic is dominant. At higher currents where the higher activation overpotentials are present, impedance response from an activation kinetic decrease and mass transport effect may appear with a new impedance feature with a Warburg element emerges at low frequencies.

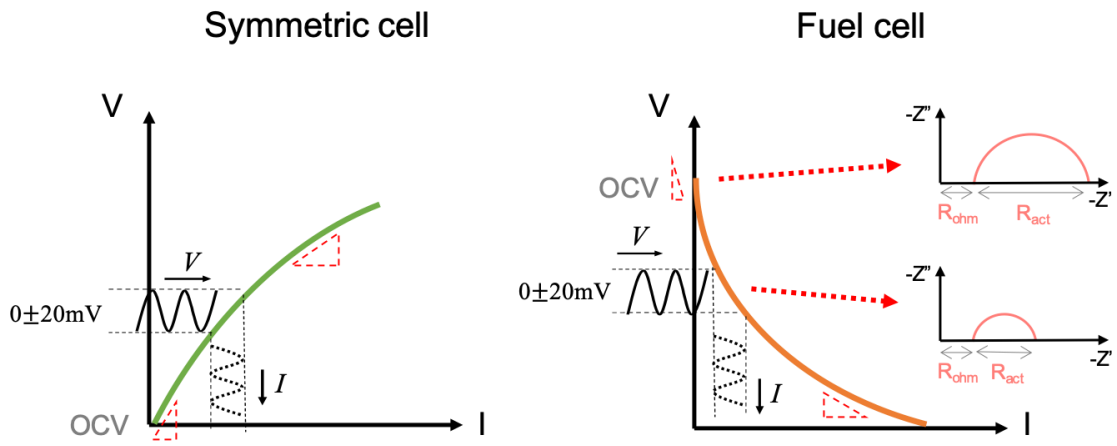

Figure 2.9 Schematic of AC impedance response in relation to polarization curves for symmetric cell and fuel cell. Examples of Nyquist plots at two different points along a fuel cell polarization curve are shown, describing the relation between the slop and impedance response.

C h a p t e r 3

HYDROGEN ELECTRO-OXIDATION KINETICS ON PLATINUM-PALLADIUM BIMETALLIC THIN FILMS

Paik, H., Berenov, A. V., Skinner, S. J., Haile, S. M., Hydrogen Oxidation Kinetics on Platinum-Palladium Bimetallic Thin Films for Solid Acid Fuel Cells, *APL Materials*, **7**, 013201 (2019) doi : 10.1063/1.5050093

Abstract

Solid acid fuel cells (SAFCs) based on the proton-conductive electrolyte CsH_2PO_4 have shown promising power densities at an intermediate operating temperature of ~ 250 °C. However, Pt loadings in SAFCs remain higher than desirable, and the electrocatalysis mechanisms in these devices are still unknown. Here, hydrogen oxidation kinetics on Pt and Pt-Pd bimetallic thin film electrodes on CsH_2PO_4 have been evaluated to establish the potential for a beneficial role of Pd in SAFC anodes. Symmetric cells fabricated by depositing metal film on both sides of electrolyte discs are characterized for studying hydrogen electro-oxidation across the gas | metal | CsH_2PO_4 structure. It was found that Pd reacts with CsH_2PO_4, forming palladium phosphide at the metal-electrolyte interface. Accordingly, the activity of Pd was examined in a bilayer geometry of Pd | Pt | CsH_2PO_4 | Pt | Pd. The bilayer Pt | Pd films showed much higher activity for hydrogen electro-oxidation than films of Pt alone, as AC impedance spectroscopy measured. *Ex-situ* low energy ion scattering and scanning transmission electron microscopy revealed that Pd diffused into the Pt layer under operating conditions. The dramatic impact of Pd along with its presence

throughout the film suggests it catalyzes reactions at both the metal-gas and metal-electrolyte interfaces, as well as increasing hydrogen diffusion rates through the films.

3.1 Introduction

In this chapter, the suitability of Pd as a catalyst component in SAFC anodes is examined. Pd and Pd-Pt alloys have shown high activity in SAFC cathodes, but these materials quickly react with the electrolyte.[10,19,20] It is a common suggestion that the ready oxidation of Pd in the SAFC cathode environment enables this reaction. In contrast, no such oxidation reaction would be expected in the anode environment, suggesting the possibility of stability of Pd^0 against reaction with CsH_2PO_4. Measurements of Pd electrocatalytic activity for hydrogen oxidation in SAFC anodes, however, have produced contradictory results. Louie *et al* [18] and Sasaki.[44] independently found Pd to be much more active than Pt, whereas Papandrew *et al.*[45] have reported that Pt and Pd are comparable in terms of both activity and stability. In the present work we examine the reactivity of Pd with CsH_2PO_4 under anode conditions, and explore strategies for using Pd to enhance hydrogen electro-oxidation rates in solid acid systems. To facilitate interpretation of electrochemical behavior, we employ a thin film geometry in which metal films are deposited onto a polycrystalline disk of the CsH_2PO_4 electrolyte and the resulting symmetric cells are examined under a uniform hydrogen-rich gas.[18,27,28,30]

3.2 Experiment

3.2.1 Sample preparation

CsH_2PO_4 was synthesized by dissolving Cs_2CO_3 and H_3PO_4 (85% assay) in deionized water, followed by precipitation in methanol. Disks of CsH_2PO_4, 0.75" in diameter and typically 1 mm in thickness, were fabricated by uniaxial compression at 69 MPa. The surfaces were polished to a final mirror finish using silicon carbide sandpaper with a grit size of by 8.4 μm. Metal deposition was performed using an AJA International ATC Orion system under 3 mTorr Ar. Pt was deposited in DC mode using a plasma power of 75 W, and Pd in RF mode using a power of 150 W.

3.2.2 Characterization

X-ray diffraction patterns were collected using a Rigaku SmartLab X-ray diffractometer (Cu Kα radiation). Diffraction analysis was used to confirm synthesis of CsH_2PO_4 and deposition of crystalline metal films (not shown). Field emission scanning electron microscopy (FE-SEM) was performed using Hitachi SU8030 with accelerating voltage 5 kV. XPS spectra were measured with a Thermo Scientific ESCALAB 250Xi X-ray photoelectron spectroscopy system using Al Kα X-ray radiation in combination with an electron flood gun. The X-ray probe size was 300 μm. For depth profiling, Ar^+ ion with 3 keV energy was used to etch a 2×2 mm^2 area of the sample. All spectra were referenced to the C 1s peak (284.8 eV).

Low-energy ion scattering (LEIS) experiments were performed using a Qtac100 (ION-TOF GmbH, Germany) instrument fitted with a double toroidal energy analyzer, which collects the scattered ions at a scattering angle of 145° from all azimuthal angles. The LEIS spectra were collected using 3 keV He^+ primary ion beams directed perpendicular to the sample surface. The primary beam was rastered over a large area (1.0×1.0 mm^2) to maintain an ion fluence below 10^{15} ions cm^{-2} and to avoid significant surface damage. The low-energy sputtering for depth-profiling was performed using a 1 keV Ar^+ beam bombardment at 59 °. The sputtered area was 1.5×1.5 mm^2.

High resolution imaging and Pt and Pd elemental mapping were performed using a Hitachi HD-2300 STEM (scanning transmission electron microscope) equipped with dual energy-dispersive X-ray spectroscopy (EDS) detectors. Data were obtained in high-angle annular dark-field (HAADF) mode using an accelerating voltage of 200 keV. Cross-sectional samples for such analysis were obtained following an established lift-out procedure[46] using a FEI Helios Nanolab 600 dual-beam focused ion beam (FIB) instrument. Around 1.5 μm of a Pt/C protection layer was deposited on top of the bilayer film to prevent surface erosion during milling, which was performed using 30 keV Ga^+ ion with 21 nA-93 pA current. In the final step, the surfaces of the extracted samples were cleaned with 2-5 keV and 28-46 pA Ga^+ ion current.

Electrochemical impedance spectroscopy (EIS) was performed using a Solartron analytical 1260 frequency response analyzer in a pseudo four-probe configuration. A 20 mV perturbation voltage about zero bias was applied over a frequency range of 100 kHz to 0.1 Hz. The impedance spectra were insensitive to gas flow rate in the range used for the

measurement, ensuring that the results were not impacted by gas-phase mass diffusion limitations. Electrode resistance values were obtained by fitting the impedance spectra using ZView software (Scribner Associates) with an empirical equivalent circuit comprised of R-CPE circuits, where CPE is a constant phase element.[43] Between three and six distinct cells were measured for each electrode thickness, and the data in this work reflect averaged values from the multiple cells.

3.3 Results and discussion

For evaluation of possible reactivity between Pd and CsH_2PO_4 under SAFC anode conditions, we performed depth-resolved X-ray photoelectron spectroscopy (XPS) on as-prepared and annealed Pd-film | CsH_2PO_4 structures, Figure 3.1. The heat treatment was carried out at 250 °C under humidified H_2 (pH_2O = 0.4 atm, balance H_2) for 40 hours. The as-prepared structure is well-behaved, showing for example, the presence of a component in the P 2p edge region at 134.5±0.1 eV corresponding to the P-O bonds in CsH_2PO_4 only after the Pd film has been removed. The emergence of the P-O peak at a nominal depth of 26 nm despite a film that is 30 nm thick is likely due to the 5 nm sampling depth inherent to the XPS method. The spectra from the annealed structure, in contrast, reveal the presence of P through the entirety of the nominally Pd film with a peak position of 130.1±0.1 eV. This feature corresponds to the formation of palladium phosphide [47] and reveals that even metallic Pd can react with CsH_2PO_4. Deeper into the structure, the P 2p peak position corresponds to that in pristine CsH_2PO_4. A large region (~50 nm) of coexistence between reduced and oxidized phosphorous suggests a non-uniform reaction front.

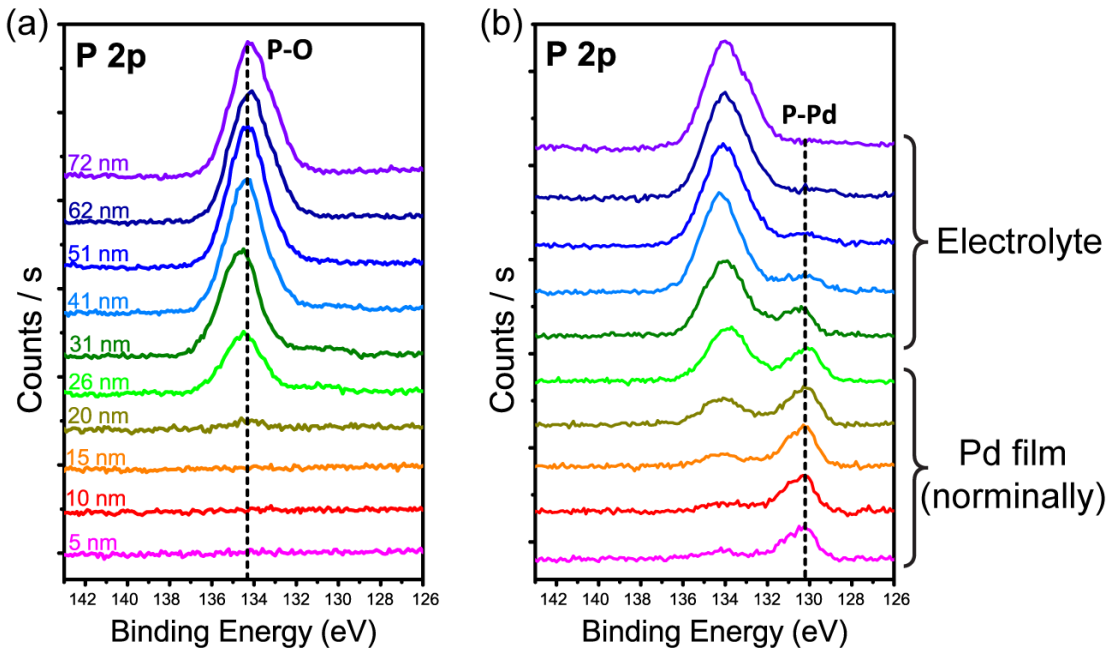

Figure 3.1 X-ray photoelectron spectroscopy (XPS) depth profile analysis in the P 2p region, collected from Pd (30 nm) on CsH_2PO_4: (a) as-deposited, and (b) after annealing for ~ 40 h under SAFC anode conditions (T = 248 °C, pH_2 = 0.6 atm, pH_2O = 0.4 atm). The etching depth indicated in (a) applies also to (b). Although not easily seen here, P 2p has spin-orbital doublets with a difference of 0.9±0.1 eV between $p_{1/2}$ and $p_{3/2}$.

The XPS spectra about the Pd 3d and Cs 3d peaks, Supplementary Figure 3.S1, were consistent with the interpretation developed on the basis of the P 2p spectra. The Pd film and CsH_2PO_4 electrolyte sharply delineate in the as-prepared sample, whereas after annealing Pd is incorporated into the electrolyte and conversely Cs is incorporated into the film. Further evidence of reaction between Pd and CsH_2PO_4 is provided from electron microscopy imaging of free-standing films obtained by dissolving away the CsH_2PO_4 substrate, Figure 3.2. The as-deposited films reveal the surface structure of the underlying polycrystalline electrolyte. In contrast, the annealed films have evolved into a less-defined structure with significant porosity. Such porosity presumably contributes to the detection by XPS of P and

Cs even at the very top region of the annealed CsH_2PO_4-Pd structure, Figure 3.1(b) and Supplementary Figure S1(d). Moreover, XPS analysis of the annealed free-standing Pd films revealed the presence of significant quantities of P and Cs on the electrolyte-facing side, whereas no P or Cs were detected in films which had not been annealed, Supplementary Figure 3.S2. A similar study of free standing Pt films, showed no morphological evolution in response to heat treatment, and no evidence of P or Cs incorporation, Supplementary Figures 3.S3 and 3.S4.

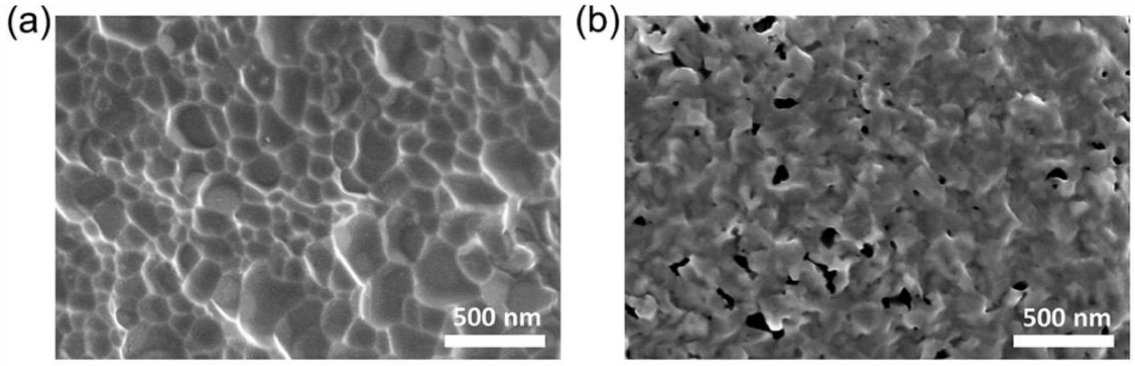

Figure 10 Scanning electron microscope (SEM) images of the electrolyte-facing side of freestanding 30 nm Pd films removed from the CsH_2PO_4 substrate: (a) as deposited, and (b) after annealing for ~40 h under SAFC anode conditions (T = 248 °C, pH_2 = 0.6 atm, pH_2O = 0.4 atm). Image in (a) reflects the morphology of the polycrystalline substrate and is essentially identical of that of analogous Pt films, Figure 3.S2 and prior work[27].

Based on these observations, the overall reaction between CsH_2PO_4 and Pd is tentatively described as

$$CsH_2PO_4 + Pd + zH_2(g) \rightarrow \frac{1}{2}Cs_2O \,/\, CsOH + Pd_xP + yH_2O(g) \qquad (3.1)$$

with Cs remaining in the fully oxidized state, whether it exists in the electrolyte or is part of a minor impurity phase in the metal/metal phosphide film. A slight shift in the Pd peak position after annealing towards high binding energy at the metal-electrolyte interface

[Figure 3.S1(b), Figure 3.S2(c)] indicates maximum formation of the phosphide at this location.

In light of the obvious reaction between CsH_2PO_4 and Pd, electrochemical experiments with Pd directly applied to the electrolyte material were not pursued. Instead, the activity of Pd for catalyzing the reaction step at the metal | gas interface was assessed using bilayer films of Pd on Pt, under the hypothesis that Pt would serve as a reaction barrier to be eventually replaced by a less expensive material should Pd prove promising in this configuration. In this context it is to be noted that we have previously demonstrated that the global interfacial impedance associated with hydrogen electro-oxidation across the CsH_2PO_4 | Pt-film | gas interface as measured by AC impedance spectroscopy, occurs via a serial process in which hydrogen is incorporated at the gas-metal interface, diffuses through the metal to the electrolyte interface, and is incorporated there as protons.[27] Though not demonstrated, it is supposed that charge transfer (conversion of atomic hydrogen to protons) occurs at the metal-electrolyte interface. In thick films (> ~50 nm), the process is dominated by solid state diffusion through the Pt film, whereas the process is co-limited by reaction and diffusion across thinner films. On the basis of the film thickness trend, the resistance associated with the reaction step (or steps) alone, *i.e.*, excluding diffusion, for hydrogen electrooxidation on Pt was estimated to be 2.2 Ω cm^2. Those results are generally corroborated here, Supplementary Figure 3.S5, in which impedance as a function of Pt film thickness in the range 15 to 80 nm has been recorded.

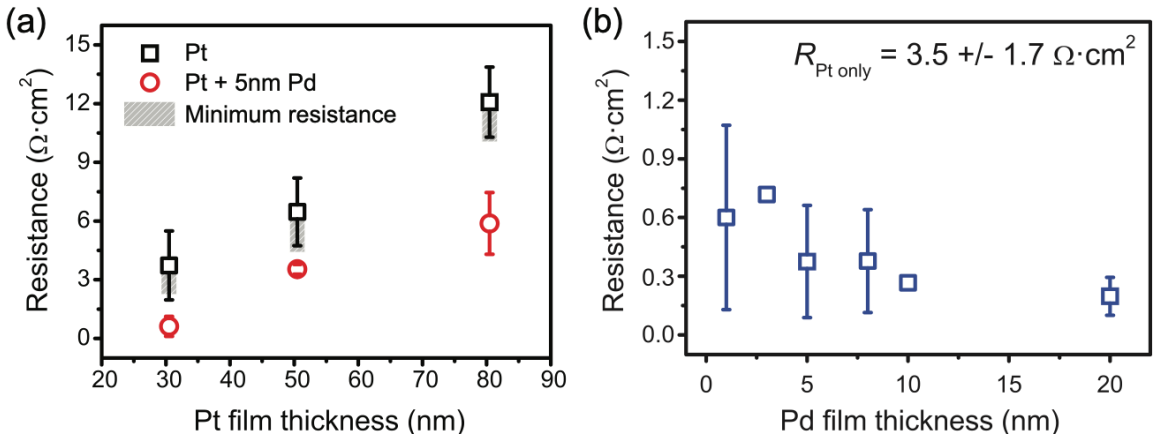

Figure 3.3 **.** Electrochemical interfacial resistance under SAFC anode conditions (T = 248 °C, pH_2 = 0.6 atm, pH_2O = 0.4 atm, after 22 h of equilibration) at zero bias of (a) Pt | CsH_2PO_4 | Pt and Pd | Pt | CsH_2PO_4 | Pt | Pd symmetric cells with varied Pt thickness; and (b) Pd | Pt | CsH_2PO_4 | Pt | Pd symmetric cells with varied Pd thickness on 30 nm Pt. Also shown in (a) is the resistance anticipated if only diffusion through the Pt film were to contribute to the measurement.

Because the diffusion and surface reaction resistance contributions to the global reaction resistance are known for Pt, it is possible to estimate the minimum resistance that would be encountered should a Pd overlayer render the reaction steps on Pt essentially barrierless. Of course, higher impedance than this minimum would result if Pd either has no effect or hampers the reaction steps. Figure 3.3(a) shows a comparison of the measured global electrochemical resistance on Pt of varying thickness, the estimated minimum possible resistance values, and the measured resistance of Pt films with a 5 nm Pd overlayer. Impedance spectra were collected continuously under humidified hydrogen at 248 °C, and the results shown are from measurements made after 22 hours of stabilization. The impedance drifted upwards over this period, Supplementary Figure 3.S6, and the measurement after 22 hours appears as a reasonable equilibration time for the purpose of exploring the impact of film thickness and bilayer structure. In all cases, the bilayer films

display resistance values that are far lower than the estimated minimum resistances under the assumption that the role of the Pd is simply to eliminate the resistance associated with surface reaction steps. The result is particularly dramatic in the case of the 80 nm thick Pt film, which in principle, bulk diffusion resistance entirely dominated. Moreover, the thickness of the Pd overlayer has limited impact on the interfacial resistance. For an underlying Pt film that is 30 nm thick, the interfacial resistances fall from an already low value of ~0.6 Ω cm^2 when the Pd overlayer is 2 nm thick, to ~0.2 Ω cm^2 when the thickness is 20 nm, Figure 3.3(b).

The dramatic influence of Pd in the bilayer configuration indicates that it must modify the bulk characteristics of the underlying Pt. The behavior also suggests the possibility that Pt-Pd alloys may yield anodes with decreased precious metal loadings and higher activity than today's state-of-the-art electrodes. For example, given an electrode resistance of ~0.2 Ω cm^2 for bi-layer films of 30 nm Pt + 20 nm Pd, Figure 3.3(b), with a total metal loading of ~0.09 mg/cm^2, the mass normalized activity is on the order of 55 S/mg, a value approaching that achieved using Pt nanoparticles deposited on carbon nanotubes.[24]

Although the bulk phase diagram of the Pt-Pd system indicates immiscibility of these elements at 250 °C,[48] but the data are not entirely conclusive. The clear impact of Pd on the bulk characteristics of Pt films motivated us to perform chemical analysis of Pd-Pt bilayer films and search for possible intermixing. Specifically, as-deposited and annealed bilayer structures were characterized using depth-resolved low energy ion scattering (LEIS) spectroscopy, where depth profiling was achieved using Ar sputtering, and cross-sectional energy dispersive spectroscopy (EDS) in combination with high resolution scanning transmission electron microscopy (STEM). For ease of interpretation, the analyses were

performed on bilayers grown on single crystal Si (111) with Pt and Pd thicknesses of 20 nm and 15 nm, respectively and high temperature annealing was performed under dry air. Both the LEIS and EDS, Figures 3.4 and 3.5, respectively, show that the as-deposited bilayers are formed of distinct Pd and Pt films. Depletion of Pd at the top surface suggested by the LEIS measurements, Figure 3.4(a), is likely due to the presence of exterior impurities, and an apparent intermixing region of ~5 nm at the Pd-Pt interface is likely due to roughness created by the Ar sputtering.[49] After exposure to 250 °C for 24 hours, in contrast, Pt is clearly detected in the Pd region and conversely, Pd is clearly detected in the Pt region, Figure 3.4(b) and Figure 3.5(b).

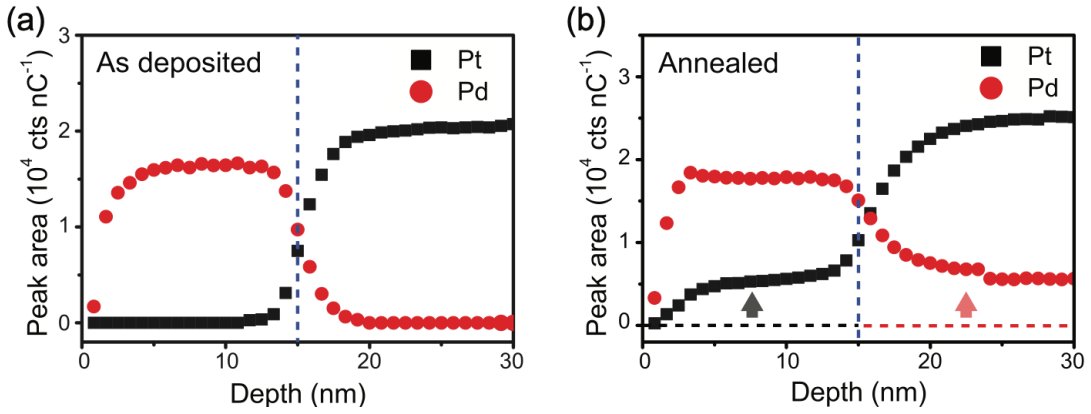

Figure 11 Integrated Pd and Pt peak areas from low-energy ion scattering (LEIS) spectra as a function of depth, from 15 nm Pd | 20 nm Pt bilayers on an Si substrate: (a) as deposited, and (b) after annealing at 250 °C for 24 hours in synthetic air. The interface between the Pd and Pt films is indicated with a dashed line in both figures.

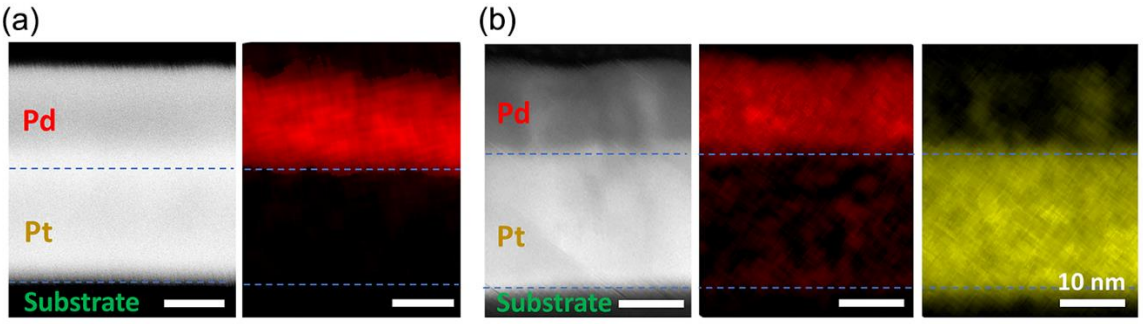

Figure 3.5 Scanning transmission electron microscope (STEM) images in high-angle annular dark-field (HAADF) mode, and energy-dispersive X-ray spectroscopy (EDS) measurements of Pd (red) and Pt (yellow) concentrations, from 15 nm Pd | 20 nm Pt bilayers on an Si substrate: (a) as-deposited, and (b) after annealing at 250 °C for 24 hours in synthetic air.

Complete intermixing between Pd and Pt is unexpected in light of the limited miscibility of these two metals at 250 °C. However, it is known that when a polycrystalline metal film is in contact with another material, rapid incorporation of the foreign element along grain boundaries can occur even at a low temperature.[50] The heterogeneous distribution of Pt in Pd and of Pt in Pd that the EDS elemental mapping evinces, Figure 3.5(b), suggests that such a phenomenon has occurred here. Accordingly, we propose that Pd-rich grain boundaries within the nominally Pt film become pathways for rapid hydrogen diffusion, Figure 3.6. With increasing thickness of the underlying Pt film at constant Pd thickness, the cross-sectional area of such Pd-rich pathways must decrease, resulting in the observed increase in the global electrochemical reaction resistance, Figure 3.3(a). The analogous situation presumably occurs when the thickness of the Pd film varies at fixed Pt thickness, Figure 3.3(b). The extremely low impedance (0.2-0.5 Ω cm^2) when the Pd : Pt film thickness ratio exceeds 2 : 30, falling below that for the electrochemical reaction step(s) of Pt-only films (~2.2 Ω cm^2) indicates that the Pd must also provide benefit to the interfacial processes.

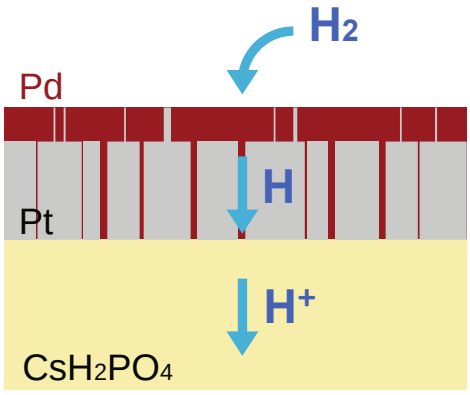

Figure 12 Schematic of the structure proposed to form from Pt-Pd bilayers as a consequence of Pt-Pd interdiffusion along grain boundaries, and the resulting pathways created for hydrogen electrooxidation on CsH_2PO_4.

In an attempt to assess whether the benefits of Pd accrue from the inherent chemistry of a fine-scale composite of Pt-Pd or from the proposed grain-boundary templated structure, we measured the electrochemical characteristics of co-sputtered films of Pd and Pt. Remarkably, the co-sputtering yields resistance values that are about three times greater than that of bilayer structures with identical overall composition and film thickness, Figure 3.7. The result supports the hypothesis that grain-boundary templating creates favorable hydrogen transport pathways. Despite the activity penalty encountered by co-sputtering, even these films show much higher activity than Pt-only films of equal thickness, and even higher activity than if only the surface steps on Pt are considered.

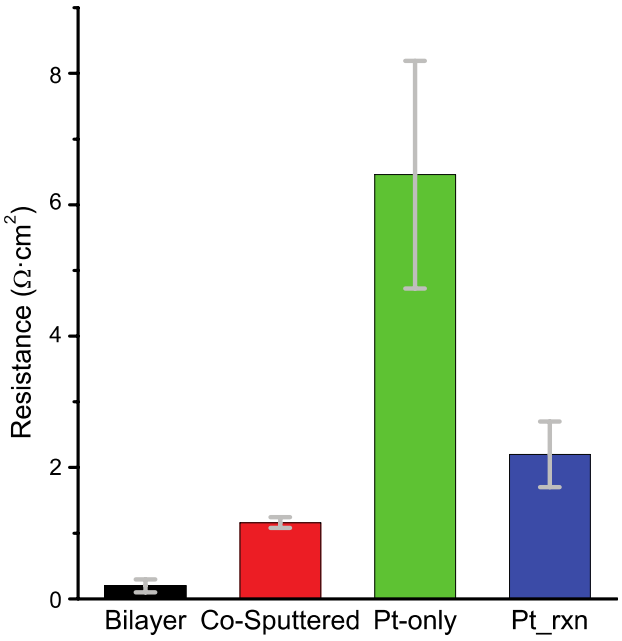

Figure 3.7 Comparison of electrode resistance under hydrogen at 250 °C obtained from different types of 50 nm thick films on CsH_2PO_4: Pd-20nm | Pt-30nm; co- sputtered Pd_2Pt_3; Pt; and an estimate of the resistance for the surface reaction steps (only) on Pt. Error bars are the standard deviations obtained from averaging results from multiple cells.

3.4 Conclusion

Despite reaction between Pd and CsH_2PO_4 under reducing conditions, Pd-Pt nanocomposites appear to be more suitable electrocatalysts for hydrogen electro-oxidation than Pt alone in solid acid fuel cells. Moreover, we find that the activity in such composites can be manipulated via control of the Pd-Pt distribution. We propose that Pd in an initially bilayered structure permeates the grain boundaries of Pt films, creating pathways for rapid hydrogen diffusion. Remarkably, the surface/interfacial reaction steps in such composite films are also more facile than the analogous steps on Pt-only films. This observation opens up the possibility that the products of reaction between Pd and CsH_2PO_4, which require

several hours to form and which other experiments may have overlooked, may be highly active catalysts for hydrogen electrooxidation.

3.5 Supplementary information

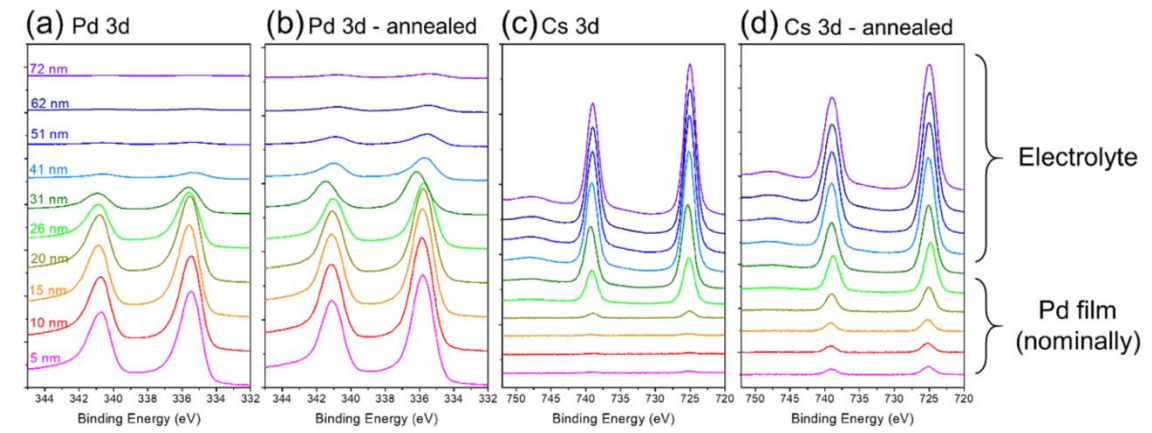

Figure 3.S1 X-ray photoelectron spectroscopy (XPS) depth profile analysis in the (a, b) Pd 3d and (c, d) Cs 3d regions, collected from Pd (30 nm) on CsH_2PO_4: (a, c) as-deposited, and (b, d) after annealing for ~40 h under SAFC anode conditions (T = 248 °C, pH_2 = 0.6 atm, pH_2O = 0.4 atm). The etching depth indicated in (a) applies also to all other panels. Pd 3d and Cs 3d signals appear as doublets due to spin-orbit splitting, 3d3/2 and 3d5/2. In (b), Pd 3d peaks are detected in the electrolyte and the peak positions at 31 nm depth are shifted by 0.4 eV to higher binding energy indicating oxidation of the Pd. In (d) Cs peaks are detected in the metal film, concomitant with the formation of Pd-P.

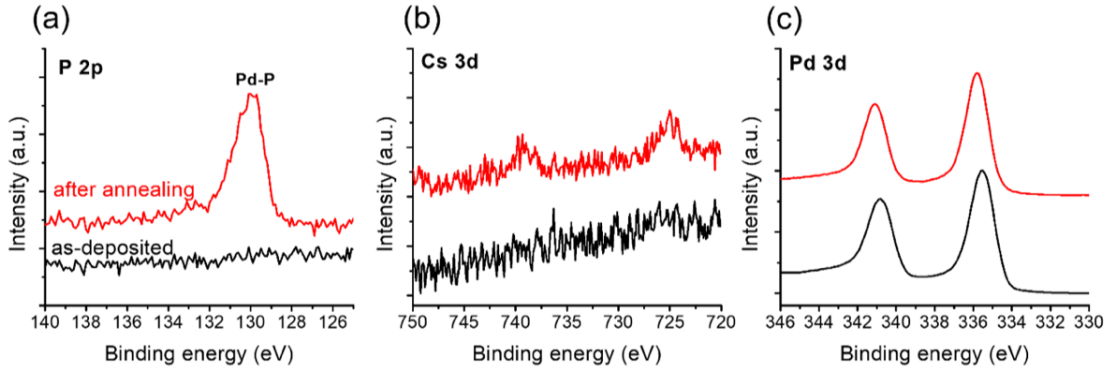

Figure 3.S2 X-ray photoelectron spectroscopy (XPS) analysis after substrate removal of the electrolyte-facing side of free-standing 30 nm Pd films, both as-deposited and after annealing for ~40 h under SAFC anode conditions (T = 248 °C, pH$_2$ = 0.6 atm, pH$_2$O = 0.4 atm): (a) P 2p region; (b) Cs 3d region; and (c) Pd 3d region. After annealing, P and Cs are detected in the film, and the Pd peaks are slightly shifted indicated oxidation, presumably by P.

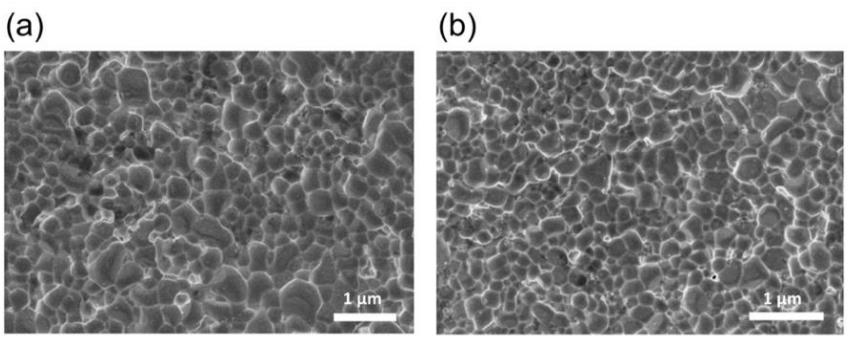

Figure 3.S3 Scanning electron microscope (SEM) images of the electrolyte-facing side of free-standing 30 nm Pt films removed from CsH_2PO_4 substrates: (a) as deposited, and (b) after annealing for ~40 h under SAFC anode conditions (T = 248 °C, pH$_2$ = 0.6 atm, pH$_2$O = 0.4 atm). The features reflect the morphology of the polycrystalline substrates and are essentially identical of that of analogous Pt films of a prior study[27].

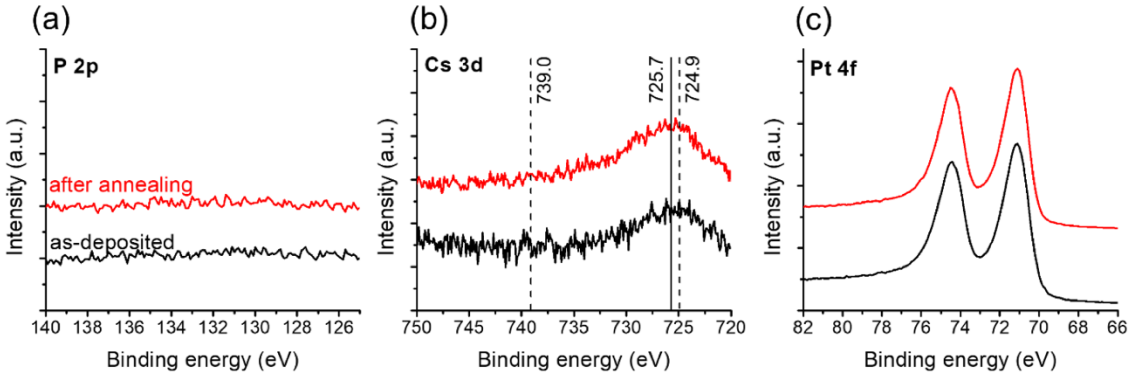

Figure 3.S4 X-ray photoelectron spectroscopy (XPS) analysis of the electrolyte-facing side of free-standing 30 nm Pt films, both as-deposited and after annealing for ~40 h under SAFC anode conditions (T = 248 °C, pH$_2$ = 0.6 atm, pH$_2$O = 0.4 atm): (a) P 2p region; (b) Cs 3d region; and (c) Pt 4f region. Spectra are unchanged as a result of annealing. In (b) dashed lines indicate expected positions of Cs 3d peaks, whereas the solid line corresponds to the binding energy of Pt 4s.

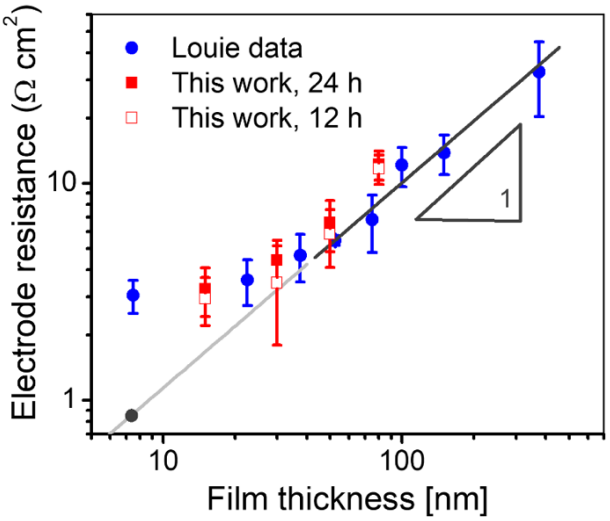

Figure 3.S5 Electrochemical interfacial resistance under SAFC anode conditions (T = 248 °C, pH$_2$ = 0.6 atm, pH$_2$O = 0.4 atm) at zero bias of Pt | CsH$_2$PO$_4$ | Pt cells as a function of Pt film thickness. Present results (with equilibration times indicated) compared to previous data from Louie.[11] Good agreement is observed. Straight line represents the expected linear dependence for a process that is fully diffusion limited. When the Pt film thickness falls below about 50 nm, surface reaction steps become important.

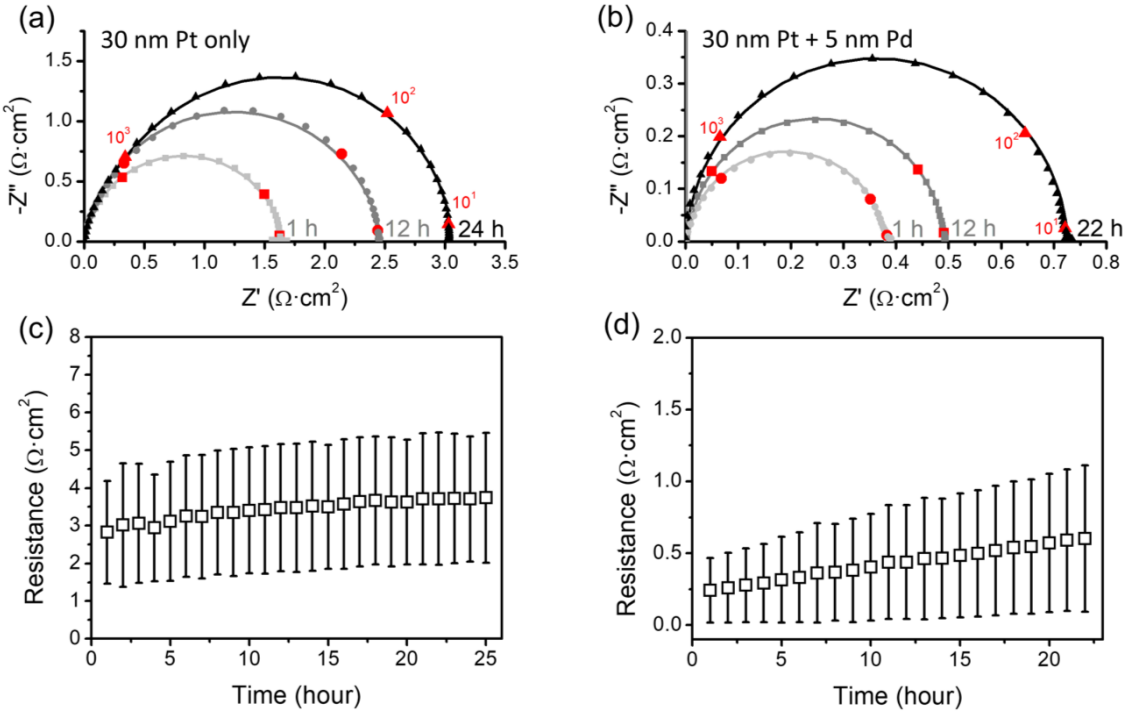

Figure 3.S6 Representative electrochemical results under SAFC anode conditions (T = 248 °C, pH$_2$ = 0.6 atm, pH$_2$O = 0.4 atm) at zero bias: (a,c) measurement of 30 nm Pt | CsH_2PO_4 | 30 nm Pt symmetric cells, and (b,d) measurement of 5 nm Pd - 30 nm Pt | CsH_2PO_4 | 30 nm Pt - 5 nm Pd symmetric cells. Raw impedance spectra shown in (a) and (b) after subtraction of ohmic resistance due to electrolyte and stray induction due to apparatus. Time evolution of electrochemical interfacial resistance as averaged over multiple cells presented in (c) and (d), indicating spread in values and typical level of temporal evolution.

Chapter 4

HYDROGEN ELECTRO-OXIDATION KINETICS ON PALLADIUM AND PALLADIUM PHOSPHIDE CATALYSTS

4.1 Introduction

From the Pd-Pt bimetallic thin film anode study described in the previous chapter, the formation of palladium phosphide (Pd-P) was observed from the reaction between Pd and electrolyte under the anodic condition of CsH_2PO_4 based solid acid fuel cells (SAFCs).[29] Interestingly, forming the Pd-P layer and $CsOH/CsO_2$ byproduct between the Pd-film and the CsH_2PO_4 electrolyte interface does not act as a barrier for the electrochemical reaction. The product instead seems to lower the electrochemical resistance of Pd. This finding encourages the investigation of the electrochemical properties of materials formed after the reaction between Pd and CsH_2PO_4. There are preliminary results that a trace amount of CsOH may improve the hydrogen oxidation reaction of the metal catalyst, however, more than 1 wt% of CsOH added into the Pt catalyst impedes the electrochemical reaction. A more well-controlled study will need to be conducted in order to understand the effect of CsOH and/or CsO_2 on the metal catalyst in the SAFC anode.

Herein, we focus on understanding the catalytic activity of Pd-P for the hydrogen oxidation reaction in a SAFC. In the last two decades, metal phosphides have attracted substantial attention as a promising catalyst for electrochemical reactions, especially for the excellent activity for hydrogenation of alkynes, and the hydrogen evolution reaction.[51-53] In addition to catalytic activity, metal phosphides have shown outstanding stability in both

acidic and basic media.[54] As one of the metal phosphides with an extensive based of research, Pd-P also has shown catalytic activities for the hydrogen oxidation reaction and the oxygen reduction reaction,[47,54,55] as well as the hydrogen evolution reaction.[56,57] Pd-P has unique features in terms of wide range of stoichiometry.[58] Despite the presence of P in the Pd lattice, the high Pd-content phases, for instance Pd_6P and $Pd_3P_{0.8}$, have higher hydrogen solubility than Pd by creating a variable number of interstitial sites.[59] $Pd_3P_{0.8}$ forms a interstitial solution with filling the phosphorus vacant sites with hydrogen atoms.[60] Data also exist for the alloy phase of Pd_6P for higher hydrogen solubility than Pd metal and lower than $Pd_3P_{0.8}$ through the formation of hydrogen interstitial solution, $Pd_6PH_{0.15}$.[59] With these interesting properties of Pd-P, we evaluate the electrocatalytic activity of Pd-P for the hydrogen oxidation reaction in SAFC anodes in comparison to Pd and Pt catalysts. Examination of electrocatalytic performance of the metal catalyst is carried out by preparing the electrode composite spread over the in-house fabricated anode supported half-cell. The working electrode composite that contains the catalyst of interest is made up of a mixture of CsH_2PO_4 particles and carbon supported metal nanoparticles. The resulting cells are assessed by I-V polarization and AC impedance spectroscopy analysis as well as crystal structural characterization in order to evaluate the Pd-P as the catalyst for hydrogen oxidation reaction in SAFC system.

4.2 Experiment

4.2.1 Deposition of Pd nanoparticles on carbon

Depositing ~62 wt% of Pd nanoparticles on Vulcan, a high surface area carbon support, was prepared by the following procedure. 45 mg of Vulcan XC-72R (Fuel Cell Store) was mixed in 20 ml of deionized water by magnetic stirring. A small amount of additional deionized water was added to rinse any Vulcan on the beaker walls. While stirring, 120.8 mg of palladium(II) chloride ($PdCl_2$, ≥ 99.9 %, Sigma Aldrich) was added. An aqueous solution of 80 mg of sodium borohydride ($NaBH_4$, 98 %, Sigma Aldrich) dissolved (and stirred by spatula) into 30 ml of ice-cold deionized water was slowly added into the solution drop wise using a pipette. Stirring was continued up to 30 minutes. The disappearance of the orange color from the Pd^{2+} indicated the reaction was complete at this point. The Pd decorated carbon powders were obtained by vacuum filtering the solution through a 0.45 um pore size PVDF membrane filter (Durapore, EMD Millipore) with sufficient deionized water for rinsing Samples were dried overnight at 80 °C. Theoretical yield of palladium nanoparticles on carbon support (Pd/C) was 117 mg.

4.2.2 Synthesis of Pd-P on carbon

Palladium phosphide on carbon (Pd-P/C) was prepared by mechanically mixing the synthesized Pd/C and CsH_2PO_4 in a 1:6 mass ratio in an ultra-high purity quartz boat (MTI

Corporation) with a few drops of deionized water, followed by annealing under humidified air (pH_2O = 0.38 atm) at 80 °C for 40 hours. After annealing, unreacted CsH_2PO_4 was rinsed out with sufficient amount of deionized water through the same filtering system described above. Fabrication of Pd-P/C powders was completed by drying overnight at 80 °C and crystal phases of the products are confirmed by X-ray diffraction analysis.

Another attempt to synthesize the Pd-P nanoparticles was adding Pd/C into H_3PO_4 and heating the solution at 140 °C, which is lower than boiling temperature of H_3PO_4, ~158 °C, for 6 hours under N_2 atmosphere. After annealing, the precipitate was rinsed with deionized water and ethanol through the filtering system and dried overnight at 80 °C. This approach intended to avoid the formation of CsOH or CsO_2, which were the byproducts after synthesizing the Pd-P through the reaction of Pd and CsH_2PO_4. However, this method did not result into Pd-P nanoparticles, and require further optimization of synthesis condition.

4.2.3 Characterization

The microstructure of Pd/C, Pd-P/C, and the cross-sectional structure of the electrodes were studied by field emission scanning electron microscopy (FE-SEM) using Hitachi SU8030 with an accelerating voltage of 10 kV for metal/C and 2 kV for the cross-section of electrodes in order to reduce the beam damage on CsH_2PO_4. X-ray photoelectron spectroscopy (XPS) spectra for Pd/C and Pd-P/C were collected with Thermo Scientific ESCALAB 250Xi X-ray photoelectron spectroscopy system using Al Kα X-ray radiation ($h\nu$ = 1486.6 eV) with a probe size of 300 μm, while an electron flood gun was applied for charge compensation during the measurement. The spectra of P 2p and Pd 3d were an

average of five scans acquired at pass energy of 50 eV. Thermo Advantage software was used for defining the SMART background and peak fitting. In order to confirm the crystallite size of metal nanoparticles on carbon and the phase of synthesized palladium phosphide (Pd-P) on carbon, X-ray diffraction (XRD) patterns for the metal/C were collected and analyzed. Diffraction patterns were obtained using a D/MAX Ultima, Rigaku using Cu Kα radiation (44 kV, 40 mA) with a with a 2θ range of 30-75 ° and a step size and scan rate of 0.01 ° and 5 °/min, respectively. Only diffraction patterns for the Pd-P/C after the electrochemical measurement was collected at the scan rate of 2 °/min in order to increase the signal from the limited amount of sample available from the electrochemical cells. Refinement of the diffraction patterns to estimate the crystallite size and quantitative analysis of phase composition were conducted by JADE software (MDI). It can be more specific such as refining for sample displacement and zero point offset as well as holding the Lorentzian components constant to the instrument broadening, which a calibration with LaB_6 determined.

4.2.4 Electrochemical characterization

To evaluate the catalytic activity for the hydrogen oxidation reaction on Pd/C and Pd-P/C, electrochemical cells were fabricated by applying the catalyst composite onto in-house prepared standard anode supported half-cells. The working electrode composite was prepared by mixing fine CsH_2PO_4 powder received from SAFCell, Inc. and the catalyst material for evaluating in a 3:1 mass ratio using a mortal-pestle for 3 minutes with a few drops of isopropyl alcohol to mix thoroughly. 50 mg of working electrode composite powder

was spread over the other side of the half-cell, and pressed at 3 tons for 3 seconds. The carbon paper and stainless steel gas diffusion layer were placed subsequently on top of the working electrode.

For electrochemical characterization, the fabricated cells were sealed into an in-house constructed electrochemical cell test station. Impedance spectra at the open circuit voltage and polarization curves were obtained at 250 °C under humidified (pH_2O = 0.38 atm) high purity hydrogen on both sides of the cell. Data were recorded using a SP-300 potentiostat (Bio-Logic Science Instrument) configured with an integrated frequency response analyzer. Impedance spectra at the open circuit voltage were collected over the frequency range 0.1 to 10^6 Hz under 20 mV sinusoidal perturbation voltage. Polarization curves were obtained every 30 minutes by scanning the voltage from 0 to 0.4 V at a rate of 10 mV/s to induce the hydrogen oxidation reaction at the working electrode and the hydrogen evolution reaction at the counter electrode where the standard Pt anode worked as a catalyst.

4.3 Results and discussion

Figure 4.1 shows representative morphologies of the synthesized Pd/C and Pd-P/C. It is notable that agglomerated excess Pd nanoparticles are observed in addition to the well-distributed nanoparticles on the carbon surfaces. The feature of the Pd is relatively clear and the size is smaller compared to the Pd-P nanoparticles. After synthesizing the Pd-P nanoparticles by annealing Pd and CsH_2PO_4 under humidified H_2, the average crystallite size of the Pd-P particles increase about 40-80 % compared to the size of the Pd estimated by analyzing the X-ray diffraction patterns using the Scherrer equation[61]. Two types of Pd-P/C

are prepared; Pd-P/C #1 is Pd_6P rich, and Pd-P/C #2 is $Pd_3P_{0.8}$ rich phase. Both Pd_6P and $Pd_3P_{0.8}$ are thermodynamically favorable phases, forming spontaneously during the reaction between Pd and CsH_2PO_4 under humidified H_2 at 250 °C. $Pd_3P_{0.8}$ is one of the variation of Pd_3P phase with random vacancies at the phosphorus position.[62] Quantitative phase analysis for the synthesized Pd-P is conducted by refinement of the diffraction patterns presented in Figure 4.2 and the estimated phase compositions with 6 % of standard deviation as a consequence of the fitting are described in Table 4.1. In both cases, more than 5 % of the Pd particles remain unreacted. Diffraction patterns of Pd_6P and $Pd_3P_{0.8}$ are identical aside from three characteristic peaks in the $Pd_3P_{0.8}$ spectrum indicated with stars.

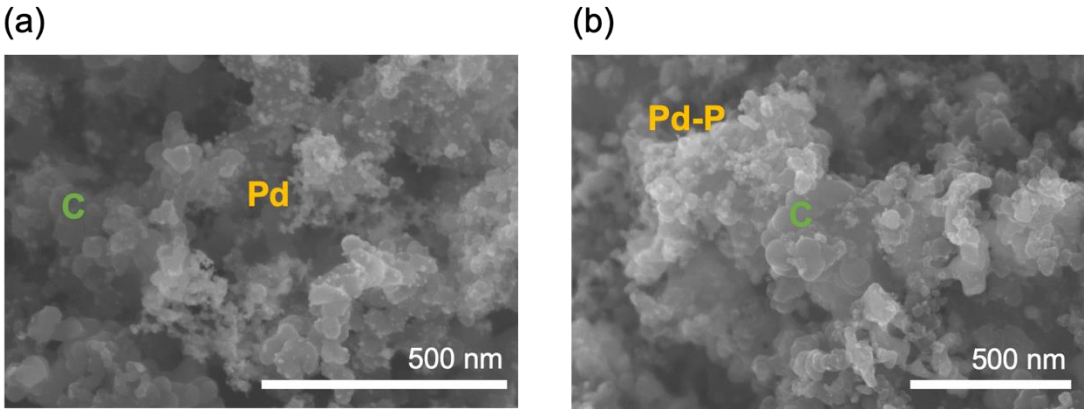

Figure 4.1 SEM image of Pd nanoparticles deposited on the carbon (a) and as-synthesized Pd-P (palladium phosphide) on the carbon after chemical reaction with CsH_2PO_4 (b).

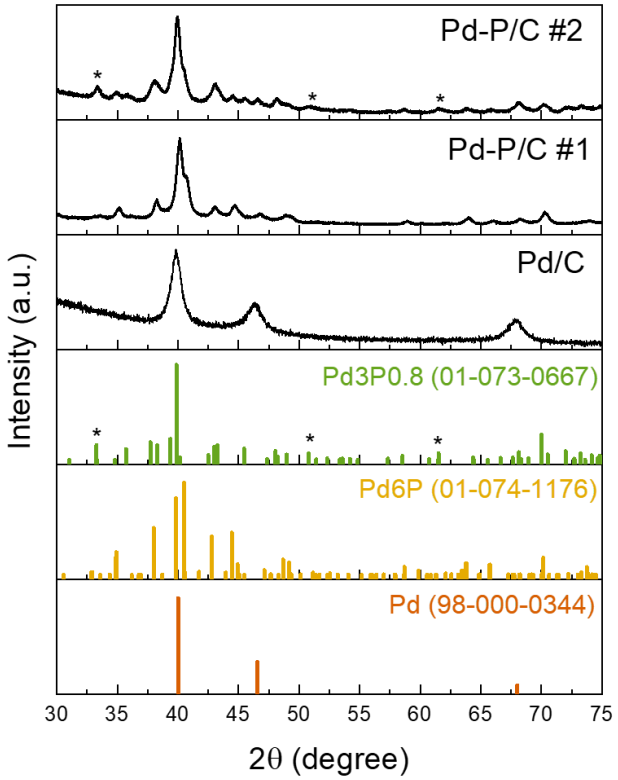

Figure 4.2 X-ray diffraction patterns from the as-prepared Pd/C and two different powders of Pd-P/C; one is Pd_6P rich (Pd-P/C #1) and the other one is $Pd_3P_{0.8}$ rich (Pd-P/C #2) Reference spectra of Pd, Pd_6P, and $Pd_3P_{0.8}$ are presented with their PDF numbers. Marks (*) indicate the characteristic peaks of $Pd_3P_{0.8}$ different from the Pd_6P.

Sample	Estimated phase composition of metal (wt%)
Pd/C	100 % Pd
Pd-P/C #1	10±0.1 % Pd; 90±0.7 % Pd_6P
Pd-P/C #2	6±0.4 % Pd; 19±1 % Pd_6P; 75±4 % $Pd_3P_{0.8}$

Table 4.1 Estimated phase composition of Pd and Pd-P synthesized on the carbon.

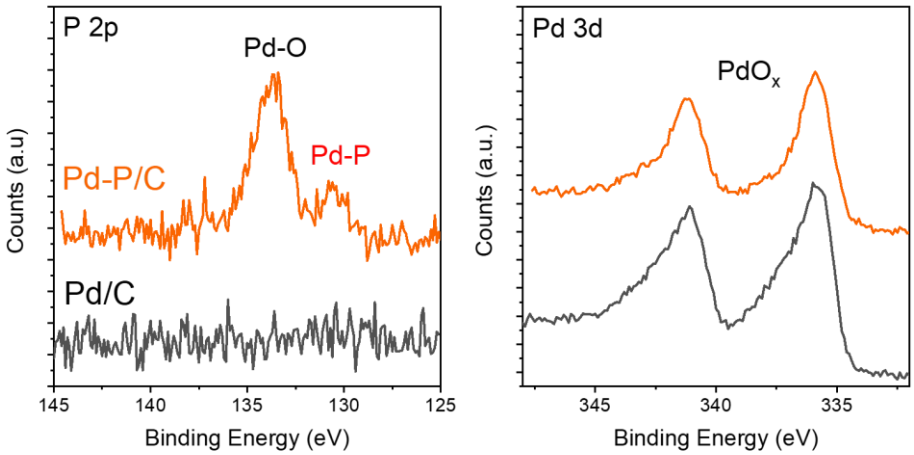

Figure 4.3 XPS spectra in the P 2p and Pd 3d region collected from the Pd/C (black line) and synthesized Pd-P/C(orange line). Pd-O peak appeared at ~134 eV comes from the residue of CsH_2PO_4 from the synthesis process of Pd-P. Two peaks in Pd 3d region are from the spin-orbital doublets, $3d_{3/2}$ and $3d_{5/2}$.

XPS analysis on the Pd/C and Pd-P/C is carried out in order to compare the chemical state of Pd as well as to confirm the existence of P at the P 2p and Pd 3d level (Figure 4.3). The peak near the 130.7 eV attributed to the bonding between palladium and phosphorus, and the peak around the 134 eV from the phosphorous bonded to the oxygen originated from the CsH_2PO_4 residue indicate the successful synthesis. Detection of Cs 3d peaks from the Pd-P/C sample (not shown) supports the existence of CsH_2PO_4. There is a negligible change in the peak positions of Pd 3d before and after converting to Pd-P, yet both have partially oxidized palladium, indicating the formation of palladium oxide during the Pd nanoparticle synthesis on the carbon support. Supplementary Figure 4.S1 presents deconvolution results of Pd 3d peaks into Pd^{2+} and Pd^0 peaks for both Pd/C and Pd-P/C. Increment of the relative

intensity of Pd^0 peak over Pd^{2+} from the Pd-P/C implies the reduction of PdO during the Pd-P formation.

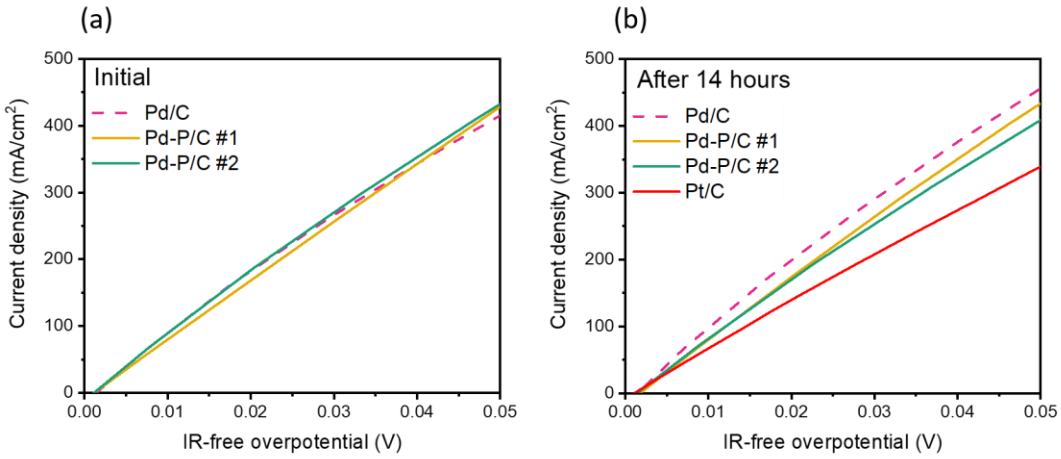

Figure 4.4 Comparison of IR-free polarization curves of electrochemical cells with different working electrodes composed of Pd/C (dash line) or Pd-P/C (solid line), (a) initial behavior and (b) after 14 hours electrochemical measurement. Polarization curve for 74 wt% Pt/C (15 mol%) electrode after 8 hours measurement is included to compare the performance with the Pd based electrodes.

In order to assess the catalytic performance for hydrogen oxidation reaction of Pd_6P rich and $Pd_3P_{0.8}$ rich palladium phosphide in comparison with the Pd-only, each catalyst is supported on carbon (~60 wt%) and introduced into a working electrode for the electrochemical cell. Each cell performance is characterized under the hydrogen oxidation condition. To minimize the size effect on the activity, all the catalysts are prepared with the average sizes in range of 11-15 nm. Figure 4.4 shows IR-free polarization curves of the three different catalysts; (1) Pd-only, (2) Pd_6Pd rich Pd-P (Pd-P/C #1), and (3) $Pd_3P_{0.8}$ rich Pd-P (Pd-P/C #2). Figure 4.S2 presents standard polarization curves, where the ohmic resistances are included. Applying voltage across the cells induces the hydrogen oxidation reaction to occur at the working electrode, where the subjected catalyst is present, and the proton

reduction reaction takes place at the counter electrode composed of the standard 20 wt% Pt catalyst on carbon support. Initial electrochemical responses from the three different catalysts at the working electrode are similar (Figure 4.4 (a)). However, after 14 hours of repeated electrochemical measurements (Figure 4.4 (b)), the catalytic performance of Pd overtakes the one of Pd-P as a result of the reduction of electrochemical resistance of Pd catalyst over time, while there is a negligible change in this resistance for the Pd-P catalysts. Initial phase composition of Pd-P seems less important based on the results of Pd-P/C #1 and Pd-P/C #2. X-ray diffraction analysis on the Pd-P/C #1, which was Pd_6P rich phase, after electrochemical measurement reveals the presence of $Pd_3P_{0.8}$ phase (not shown). This implies that the composition of Pd-P phases in the electrode is varying to the more thermodynamically favorable phases through solid-state phase reaction [63,64] during cell operation.

In order to compare the electrochemical properties of Pd and Pd-P, analogous molar amount of Pt catalyst on carbon (15 mol%) is prepared in a similar fashion to the Pd/C, using H_2PtCl_2 precursor instead of $PdCl_2$. Surpassing performance of Pd and Pd-P for the hydrogen oxidation reaction suggests a way to improve the overall fuel cell performance by replacing the anode catalyst to the Pd or Pd-P from the Pt. Comparable electro-catalytic performances of Pd and Pd-P for oxidizing the hydrogen are predictable results as Pd is expected to transform into Pd-P during the cell operation by a reaction with the CsH_2PO_4. Revealing the structural phase of the Pd/C after long-term measurement verifies this hypothesis. Figure 4.5 shows that the structure of Pd catalyst has changed into the mixture of Pd_6P, $Pd_3P_{0.8}$ and Pd, with 56±7 wt%, 30±4 wt% and 14±1 wt%, respectively.

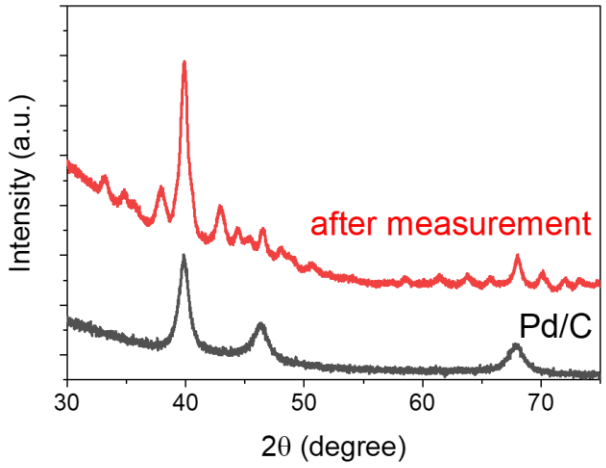

Figure 4.5 Comparison of X-ray diffraction patterns of the Pd/C as it was prepared before the measurement and the Pd/C after long-term electrochemical measurement (about 130 hours). Diffraction spectra for the one after measurement is collected after rinsing out the CsH_2PO_4, which was mixed with the Pd/C catalyst to compose the working electrode.

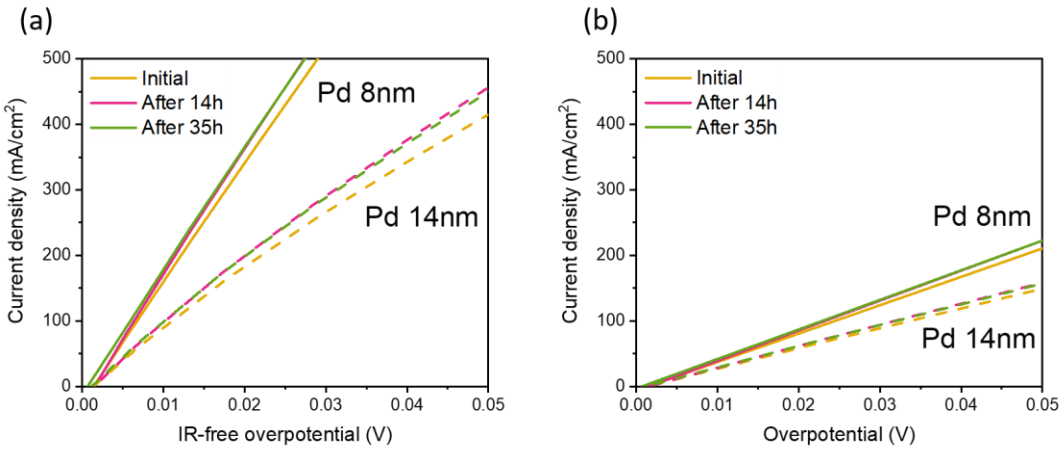

Figure 4.6 Temporal evolution of electrochemical behavior of the working electrodes with 8nm of Pd/C and 14nm Pd/C, presented in (a) IR corrected and (b) uncorrected polarization curves. Solid lines are from the electrochemical cell with the electrode composed of the 8nm Pd/C and dash lines are from the 14nm Pd/C.

Because the heterogeneous catalysis effect occurs at the surface, reducing the Pd nanoparticles size improves the catalytic performance substantially by increasing the ratio of

the surface area to the volume of the catalyst on the carbon support. Figure 4.6 shows the hydrogen oxidation polarization curves acquired from the Pd catalyst with the crystallite size of 14nm and 8nm, where X-ray diffraction results provide size estimates using Scherrer equation.[65] Both Pd catalysts show notable stability in I-V curves after initial improvement current density at a voltage. Evolution of impedance response at the open circuit voltage is presented in Figure 4.7. Regardless of the size of Pd nanoparticles, the reduction of ohmic resistances is observed, likely by the evolution of electrode structure. Impedance spectra for Pd catalyst consist of a distinct high frequency RQ circuit and more than two series of RQ circuits at the low frequency region. Here, R refers to a resistor and Q is a constant phase element.[43] The features at the low frequency are considered as a consequence of the hydrogen transport in the electrode.[27] This assumption is supported by an additional impedance measurement where low concentration of hydrogen, 3% hydrogen balanced with Ar, is supplied at the working electrode, while the counter electrode keeps the same gas condition (Figure 4.S3). The low frequency arc becomes substantial under the dilute hydrogen, implying the mass transport limitation is related. With this inference, the impedance spectra of Pd with the average particle size of 14 nm is interpreted as the hydrogen transport in the electrode is more limited than the one with 8 nm.

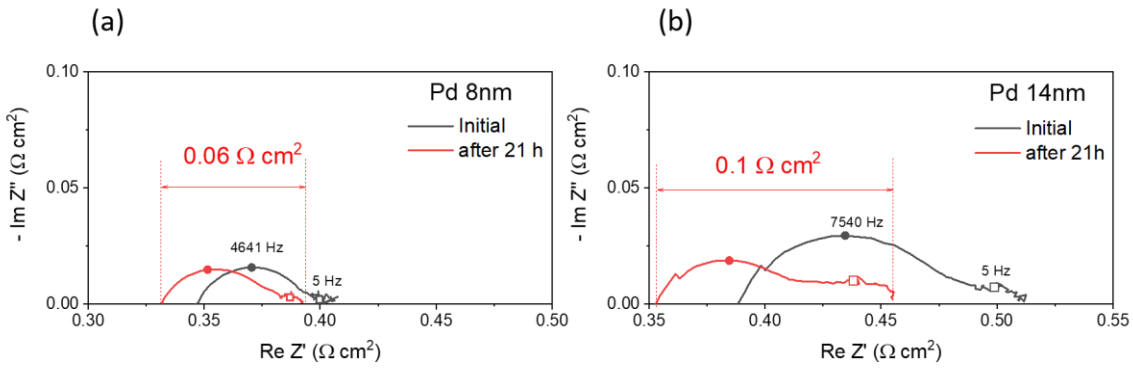

Figure 4.7 Impedance spectra at the open circuit voltage for the electrochemical cells with the working electrode consisting of (a) 8nm Pd/C and (b) 14nm Pd/C. Temporal evolution of impedance response from initial (black line) to after 21 hours electrochemical measurement (red line) are presented.

This result may correlate with the microstructure of the electrode shown in Figure 4.8. Figure 4.8(a) presents a representative image of the as-prepared mixture of Pd/C and CsH_2PO_4, where the morphology is alike regardless of the Pd size. After the electrochemical test, microstructural differences are observed from the cross-sectional images of the working electrodes with the 14 nm and 8 nm Pd. A distribution of CsH_2PO_4 particles at the working electrode, where 14nm Pd particles are deposited on carbon, is more agglomerated than the one with the 8nm Pd. Severe agglomeration of the CsH_2PO_4 is likely from the reaction between Pd and CsH_2PO_4, which may give a greater impact with a larger size of Pd. Losing the porosity at the working electrode as a result of CsH_2PO_4 agglomeration may lead to increased hydrogen mass transportation limitations. Total electrode resistances of counter electrode and working electrode after 21 hours measurement are compared for 14 nm Pd and 8 nm Pd. Recalling the electrochemical resistance of standard Pt catalyst used for the counter electrode here as ~0.05 Ω cm^2,[15] the resistance from the 8 nm Pd would be below 0.01 Ω cm^2, which is the lowest value from our group in solid acid electrochemical cells for H_2/H_2.

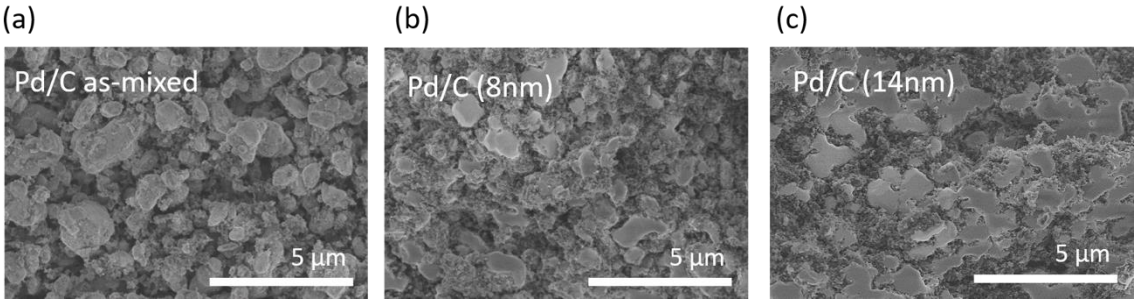

Figure 4.8 Cross-sectional SEM images of the electrodes composed of Pd/C and CsH_2PO_4 mixture. (a) representative image of as-mixed Pd/C and CsH_2PO_4 composite; (b) after electrochemical test with 8nm of Pd; (c) after electrochemical test with 14nm of Pd. Average size of CsH_2PO_4 particles is 1-3 μm.

4.4 Conclusion

The hydrogen oxidation kinetics of carbon support Pd and Pd-P nanoparticles are evaluated by preparing the working electrode for the electrochemical cells and measuring their electrochemical behavior. Synthesizing Pd-P catalysts through the annealing of Pd/C and CsH_2PO_4 together under humidified hydrogen atmosphere leads to a mixture of Pd_6P and $Pd_3P_{0.8}$ in addition to unreacted Pd. Polarization curve measurements show that the catalytic activity of Pd, Pd_6P rich Pd-P and $Pd_3P_{0.8}$ rich Pd-P are comparable, as Pd catalyst turns into Pd-P as a consequence of the reaction with CsH_2PO_4 in the electrode composite during cell operation. By comparison with the equivalent mole percent of Pt supported on carbon, both Pd and Pd-P appear to be more effective electrocatalysts for hydrogen oxidation than Pt alone. Moreover, further enhancement of Pd catalytic activity is observed by reducing its crystallite size. Reducing the Pd size leads to smaller total electrochemical resistance at the open circuit voltage, where the total electrode resistance could lower further by replacing the catalyst for the counter electrode to Pd as well. Finding the optimized metal loading and

the crystallite size of a metal can improve the catalytic properties of Pd for the hydrogen oxidation reaction.

4.5 Supplementary information

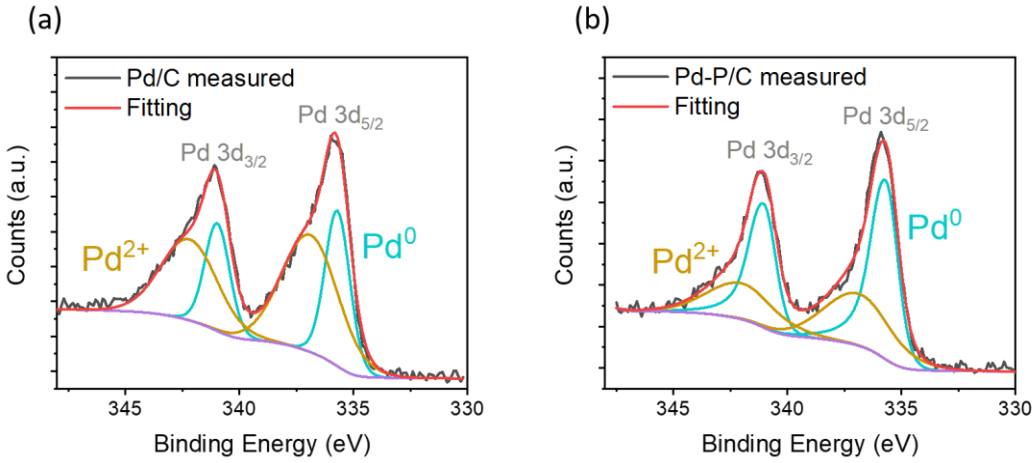

Figure 4.S1 XPS spectra in Pd 3d region collected from (a) Pd/C and (b) Pd-P/C. Pd 3d peaks are deconvoluted into Pd^0 and Pd^{2+} to show their relative amount.

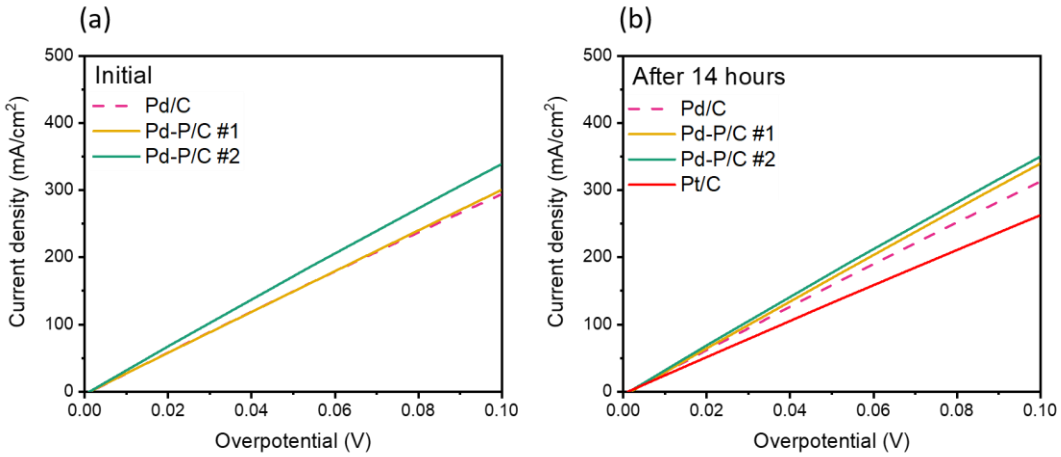

Figure 4.S2 Comparison of uncorrected polarization curves of electrochemical cells with different working electrodes composed of Pd/C or Pd-P/C, (a) initial behavior and (b) after 14 hours electrochemical measurement. Polarization curve for Pt/C electrode after 8 hours measurement is included to compare the performance with the Pd based electrodes.

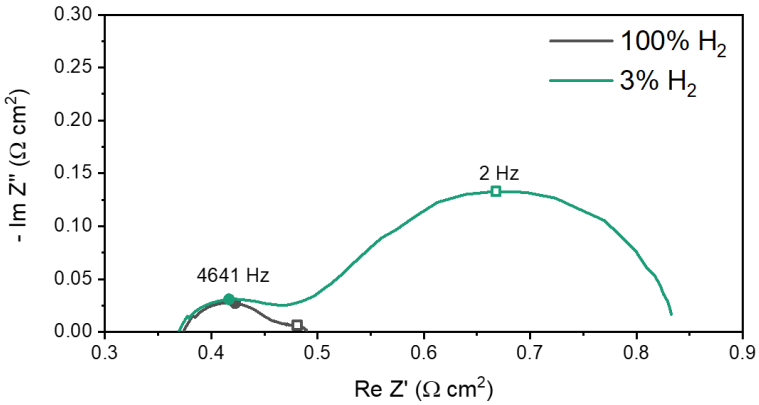

Figure 13 Comparison of impedance spectra at the open circuit voltage under humidified 100% of H_2 (black) and humidified 3% of H_2 balanced with Ar (green). Partial pressure of steam for both is 0.38 atm. Data is collected from the electrochemical cell with the working electrode composed with 14nm of Pd.

Chapter 5

OXYGEN ELECTRO-REDUCTION KINETICS ON PALLADIUM-TIN CATALYSTS

5.1 Introduction

Pd has been investigated as an electrocatalyst for the oxygen reduction reaction because of its outstanding catalytic activity compared to Pt.[10,19,20] However, the instability of Pd on CsH_2PO_4 has been an obstacle in implementing Pd in SAFCs. Incorporating Pt to form a Pd rich Pt-Pd alloy has been shown to have a high cathodic activity, yet these cathodes quickly react with CsH_2PO_4.[19,20]

In this work, SnO_2 thin film is introduced as a barrier layer to keep Pd from reacting with CsH_2PO_4 and a structural support for a Pd catalyst, utilizing its conductivity arising from intrinsic oxygen defects to maintain an electronic network.[66,67] Platinum group metals supported by SnO_2 also have been shown to improve the catalytic activity for oxygen reduction reaction,[68,69] explained by that a facility of reducing/oxidizing of SnO_2 surface can be involved in the reduction reaction.[67] The stability of SnO_2 with CsH_2PO_4 under cathode condition has been confirmed.[14]

To evaluate the SnO_2 as a support/barrier, a thin film of SnO_2 was directly deposited on CsH_2PO_4 powder by the atomic layer deposition (ALD) method. The growth of SnO_2 at the low temperature is achieved by using commercial organometallic precursor, tetrakis(dimethylamino) tin (TDMASn), and H_2O as a co-reactant.[70] ALD deposition was undergone at 150 °C, where CsH_2PO_4 is free from dehydration and decomposition.[11,71] The

assessment of the impact of SnO_2 thin films over Pd catalysts for in SAFC cathodes is carried out by the characterization of the chemistry and structure of SnO_2-Pd in a bilayer configuration and fuel cell polarization behavior.

5.2 Experiment

5.2.1 Pd deposition

Pd thin films were prepared in two ways, by RF sputtering and by metal-organic chemical vapor deposition (MOCVD). Sputtered Pd thin film was deposited on MgO (100) substrate purchased from MTI Corporation using an AJA International ATC Orion system under 3 mTorr pressure of Ar with a power of 150 W in RF mode. The thickness of Pd film was controlled by the deposition time.

Pd deposition on CsH_2PO_4 powders (supplied by SAFCell, Inc., BET surface area of ~2.4 m^2/g) or SnO_2 coated CsH_2PO_4 powder was carried out by gently shaking to mix Palladium(II) acetylacetonate ($Pd(acac)_2$, Sigma-Aldrich) precursor and CsH_2PO_4 powders and volatilizing the precursor at 210 °C in a N_2 and water vapor atmosphere.

5.2.2 ALD of SnO_2 thin film

Continuous thin films of SnO_2 were prepared by atomic layer deposition (ALD) using a pulse type Savannah 100 reactor (Cambridge Nanotech, Inc.) on powders of CsH_2PO_4 or Pd deposited CsH_2PO_4 powders. Tetrakis(dimethylamino)Tin (TDMASn, Strem) was used as the Sn source with ultra-high purity nitrogen as a carrier a carrier gas, and subsequent

deposition of SnO_2 was carried out at 150 °C using H_2O as an oxidant. Each deposition consisted of following steps: (1) 2 s pulse of TDMASn; (2) 180 s hold to provide time for the precursor to diffuse throughout the powder; (3) 180 s N_2 purge; (4) 0.015 s pulse of H_2O; (5) 180 s hold; (6) 180 s N_2 purge. This sequence of ALD steps was then repeated until a desired thickness of SnO_2 was obtained. Deposition rate was determined by a quartz crystal microbalance (QCM) measurement, which showed a deposition rate of 0.77 Å/cycle for this process.

5.2.3 Characterization

X-ray diffraction (XRD) patterns were collected using a D/MAX Ultima, Rigaku using Cu Kα radiation at 44 kV and 40 mA, with a with a 2θ range of 20-70 ° and a step size and scan rate of 0.05 ° and 5 °/min, respectively. The structural stability of the components was assessed through the analysis of the diffraction patterns X-ray diffraction spectra of Pd-Sn alloy was also analyzed to characterize the phase of the alloy. X-ray reflectivity (XRR) measurement of the SnO_2/Pd bilayer on MgO substrate was carried out to estimate the film thickness of SnO_2 and Pd using a Rigaku SmartLab X-ray diffractometer (Cu Kα radiation, 45 kV, 160 mA). Each film thickness was estimated by fitting the reflectivity spectra using Motofit software (not shown)[72]. The images of SnO_2 film and cross-sectional structure of fuel cells were obtained by field emission scanning electron microscopy (FE-SEM) using Hitachi SU8030 with accelerating voltage 10 kV. ALD deposited SnO_2 thin film was revealed by dissolving the CsH_2PO_4 in deionized water after depositing ~1 nm thickness of SnO_2 film on CsH_2PO_4 particles and placing them on adhesive carbon substrate. X-ray

photoelectron spectroscopy (XPS) spectra for SnO_2 and Pd were collected with a Thermo Scientific ESCALAB 250Xi X-ray photoelectron spectroscopy (XPS) system using Al Kα X-ray radiation (hν = 1486.6 eV) with a spot size of 300 μm in combination with an electron flood gun for charge compensation during the measurement. The spectra of Sn 3d and Pd 3d were an average of five scans acquired at a pass energy of 50 eV. Thermo Advantage software was used for full fitting including the subtraction of the SMART background and deconvolution of peaks. Chemical mapping of the top surface of SnO_2/Pd/MgO was collected by the time-of-flight secondary ion mass spectrometry (ToF-SIMS), which is a highly surface sensitive analytical method with less than 1nm depth resolution (PHI TRIFT III, Physical Electronics). Maps of the lateral distribution of elements were obtained by rastering over100 × 100 μm^2 areas (256 × 256 pixels) of interest using a 25keV Ga^+ primary ion beam. The primary ion dose rate was kept below 10^{11} ion/cm^2 in order to detect the outmost surface of the sample under static condition.[73]

5.2.4 Fuel cell fabrication and electrochemical characterization

The Pd-Sn based catalysts for oxygen reduction reaction were evaluated by fabricating 1.9 cm diameter fuel cells via a protocol described elsewhere.[4,15] The anode electrocatalyst layer was composed of 25 mg of a ball-milled mixture of CsH_2PO_4 and Pt on carbon (20 wt% Pt on carbon black, HiSPEC® 3000, Alfa Aesar) in a 6:1 mass ratio. This layer was supported on 75 mg of a mixture of CsH_2PO_4, carbon black acetylene (Alfa Aesar, 99.9 %), and naphthalene (Alfa Aesar, 99.8 %) in 3:1:2 mass ratio, where the naphthalene was used as a pore former, over the stainless steel gas diffusion layer (Dynapore® 2-layer

sintered mesh, Genesis Filtration Inc.). The anode layers were pressed together in a 19 mm diameter die at 103.5 MPa for 3 seconds. Fabrication of the anode supported half-cell was completed by pressing together with the 50 mg of CsH_2PO_4 and the anode layers at 138 MPa for a minute, followed by wrapping the side of the half cell with the Teflon tape. The thickness of the CsH_2PO_4 electrolyte was about 50 μm. Cathode powders were prepared by depositing SnO_2 and Pd thin film on CsH_2PO_4 particles described above, and 50mg of them were spread over the other side of electrolyte and pressed together at 34.5 MPa for 3 seconds. Fabrication of the fuel cell was completed by sealing the side of the cell with the Teflon tape after placing the carbon paper (TGP-H-120 Toray paper) as a current collector and stainless steel gas diffusion layer (McMaster-Carr, Type 316, mesh size 100×100) on top of the cathode layer.

For electrochemical characterization, fuel cells were sealed into an in-house constructed fuel cell test station.[4] Impedance spectra at open circuit voltage and fuel cell polarization curves were collected at 250 °C. Cathode and anode were supplied with humidified (pH_2O = 0.38 atm) high purity hydrogen and humidified synthetic air, respectively. Data were recorded using a SP-300 potentiostat (Bio-Logic Science Instrument) configured with an integrated frequency response analyzer. Impedance spectra at open circuit voltage were collected over the frequency range 0.1 to 10^6 Hz with applying a 20 mV sinusoidal perturbation voltage. Polarization curves were obtained every hour by scanning the voltage from 1 to 0 V at a rate of 10 mV/s. Previous data show the electrochemical resistance of standard anode for the hydrogen electrooxidation reaction under these conditions as ~0.05 Ω cm^2,[15] which is negligible value compared to the resistance from the

cathode reaction, and thus it is reasonable enough to consider the electrode overpotential is mostly from the cathode reaction.

5.3 Results and discussion

To confirm the reactivity between Pd and CsH_2PO_4 under cathode condition, ~16 wt% of Pd was MOCVD deposited on CsH_2PO_4 powders and diffraction patterns were collected as-deposited and after annealing under humid air for 40 hours. As shown in Figure 5.1, unidentified impurity peaks of significant intensity emerge after the anneal, in addition to those of Pd and PdO. It is notable that PdO is already formed during the Pd MOCVD deposition on CsH_2PO_4 powders.

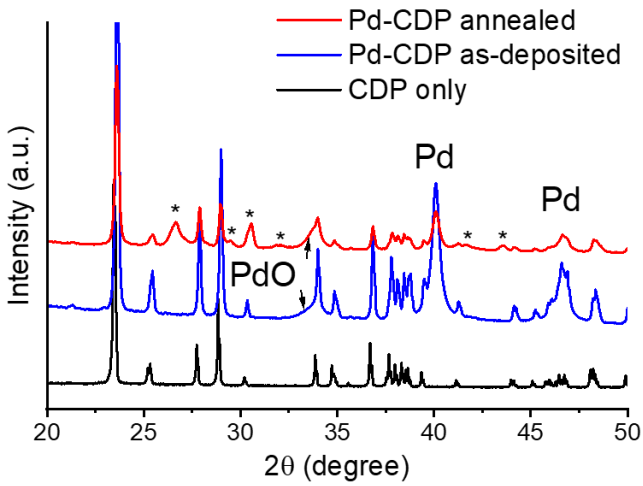

Figure 5.1 X-ray powder diffraction patterns showing reactivity of CsH_2PO_4 with Pd. Raw diffraction patterns of CsH_2PO_4 (black), CsH_2PO_4 milled with Pd (blue), and the milled mixture after annealing for 40 h at 250 ^{0}C under humidified air (red) are shown. Peaks from undefined phased are marked.

Before evaluating the role of SnO_2 oxide film at the cathode of SAFC, feasibility of ALD deposition of SnO_2 on to CsH_2PO_4 powders was first verified. After depositing nominally ~1 nm of SnO_2 film on CsH_2PO_4 powders with 13 cycles of ALD deposition sequences, free-standing SnO_2 film is revealed with dissolution of CsH_2PO_4. In Figure 5.2, SEM image of SnO_2 film confirms the successful deposition of a continuous SnO_2 thin on the CsH_2PO_4 powder. The large defects in the free-standing SnO_2 film are a result of the handling involved in removal by dissolution of the underlying CsH_2PO_4.

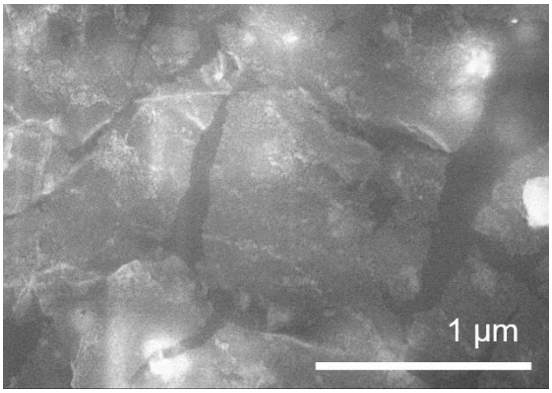

Figure 5.2 SEM image of 1 nm SnO_2 film synthesized by ALD. SnO_2 thin film deposited on CsH_2PO_4 surface is revealed by dissolving the CsH_2PO_4. Bright spots are from the underneath carbon tape feature

The ability of SnO_2 to act as a proactive barrier was evaluated by the following process; SnO_2 film was deposited by ALD over a layer of sputtered Pd film onto MgO (100) and chemical changes to this bilayer were evaluated after long-term exposure to high temperature humidified air (Figure 5.3). From the fitting results of X-ray reflectivity spectra from the SnO_2/Pd bilayer, film thickness of SnO_2 and Pd are 6 nm and 13 nm, respectively. ToF-SIMS maps presenting the lateral distributions of Pd and Sn species over a 100 × 100 μm^2 of the top surface of the SnO_2/Pd/MgO structure which in Figure 5.3(a) shows, and the

XPS spectra in Pd 3d and Sn 3d region, which Figure 5.3(b) shows. After annealing the bilayer for 40 hours at 250 °C under humidified synthetic air (pH_2O = 0.47 atm), the intensity of Pd signal from the ToF-SIMS elemental map increases clearly compared to as-deposited state, indicating that Pd does migrate through SnO_2 during the annealing. Remarkably, annealing does not change the Pd oxidation state in the XPS spectra for Pd 3d range when SnO_2 is the overlayer with a composition of about 80 % Pd^0 and 20 % Pd^{2+}, both before and after the exposure to humidified air. The Sn, on the other hand, which already shows a non-negligible concentration of Sn^0 in the as-deposited state, becomes substantially reduced as a consequence of annealing. Reduction of SnO_2, which becomes SnO_x ($x < 2$), alone under these conditions is not expected, and it is clear that this reduction occurs as a consequence of the presence of Pd. The fact that the Pd remains in the metallic state while Sn becomes reduced leads to the conclusion that an intermetallic Pd-Sn phase, which is highly stable against oxidation. Nine intermetallic Sn-Pd phases are in fact known in this binary system,[74] supporting the interpretation of XPS and ToF-SIMS results.

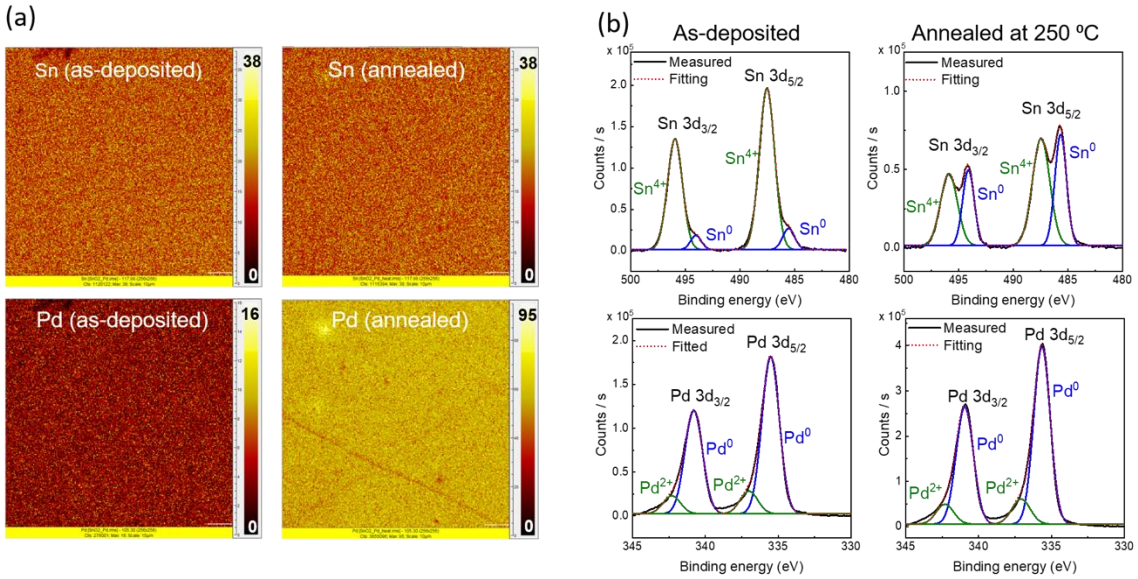

Figure 5.3 ToF-SIMS elemental mapping for Sn and Pd (a) and XPS spectra in the Sn 3d and Pd 3d region (b) collected from the SnO_x(6nm)/Pd(13nm)/MgO before (left column) and after (right column) annealing for 40 h at 250 ^{0}C under humidified synthetic air (pH_2O = 0.47 atm). (a) Top surface SIMS chemical mapping on sample does not detect the Pd underneath of SnOx film from the as-deposited, while strong Pd signal is detected after annealing. Analyzed area is 100 x 100 um, and false color scale indicates the number of counts in a pixel. (b) XPS spectra are collected in Sn and Pd ranges. The signal for Pd penetrates through the 6 nm oxide layer. Peak intensity of Sn^0 increases prominently after annealing. Baselines are subtracted for all XPS spectra and minor mismatches between measured and fitting data at the higher binding energy of Pd region (around 343 and 337 eV) is a result of the fitting with symmetric peak shape instead of asymmetric peak that is more realistic.

To evaluate reactivity of Sn-Pd with CsH_2PO_4, commercial powder of SnO_2 (Alfa Aesar, 99.9 %) was coated with Pd by MOCVD, and this coated powder was milled with CsH_2PO_4 powder. Bringing SnO_2 and Pd together in this way was found to yield a higher extent of reaction between the two materials than simply milling together oxide and metal particles. The diffraction results, Figure 5.4, show that after a heat treatment of 40 hours in humidified H_2 followed by 40 hours in humidified air at 250 °C with 0.47 atm water partial pressure. Figure 5.4(a) and 5.4(b) are the original diffraction spectra as measured and Figure

5.4(c) and 5.4(d) are the difference patterns obtained after subtracting the pattern of CsH_2PO_4 from the measured pattern. All peaks can be attributed to either CsH_2PO_4, Pd, SnO_2, or Pd_3Sn. This is the first time data shows a Pd-bearing alloy or intermetallic unreactive with CsH_2PO_4 under fuel cell cathode conditions.

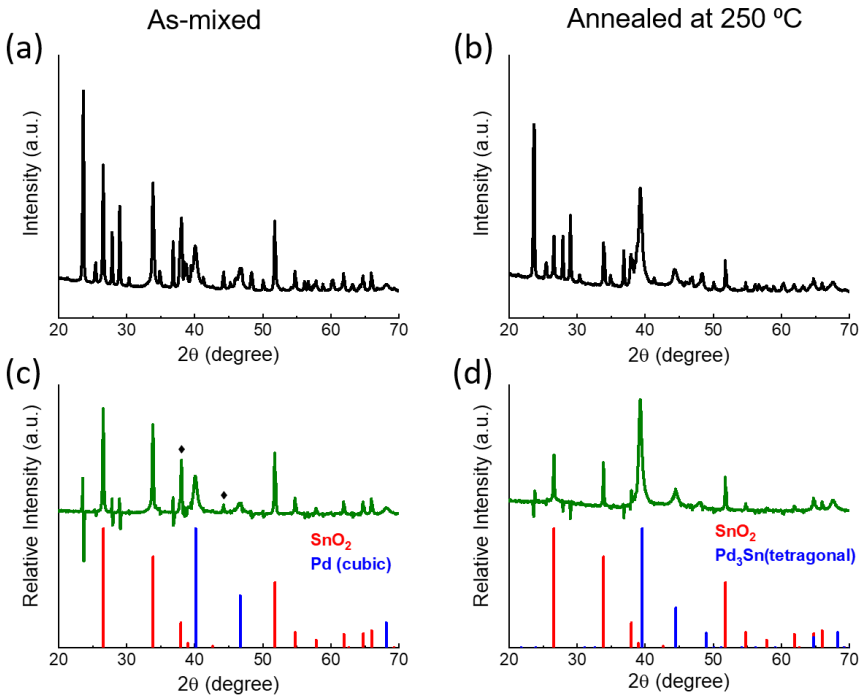

Figure 5.4 X-ray powder diffraction patterns showing non-reactivity of CsH_2PO_4 with Pd + SnO_2. (a, c) shows the diffraction patterns of as-mixed of Pd + SnO_2 and CsH_2PO_4 and (b, d) show the patterns after annealing the mixture at 250 ^{0}C under humidified hydrogen for 40 h followed by humidified air for 40 h (pH_2O = 0.47 atm). (c, d) are the difference pattern obtained after subtracting the pattern of CsH_2PO_4 from the measured pattern. Marked peaks in Figure (c) are from the sample holder substrate.

Fuel cell cathodes were prepared in three different geometries to evaluate the Pd-Sn materials as catalysts for the oxygen reduction reaction. First, an internal baseline for the behavior of Pd was established. Pd was coated onto fine (~2.4 m^2/g) CsH_2PO_4 powders (SAFCell, Inc.) using the above mentioned MOCVD method. The mass loading of Pd was

16.2 wt%, as determined by the weight change after deposition. A portion of this material was then coated with SnO_2 by ALD, with a target oxide thickness of 1 nm. The nominal Pd:Sn mass ratio is 14:1. In an attempt to assess the benefit of order of SnO_2-Pd bilayer, cathode powders with SnO_2 underneath of Pd were also fabricated. SnO_2 with the nominal thickness of 2 nm was deposited by ALD onto the fine CsH_2PO_4 powders followed by MOCVD deposition of 14.1 wt% Pd with the estimated mass ratio of Pd to Sn is 6:1. Anode-supported half-cells were fabricated and 50 mg of cathode powders were spread and pressed onto the other side of electrolyte making a completed fuel cell. Cells were raised to the measurement temperature of 250 °C with nitrogen supplied to the cathode and hydrogen to the anode (with humidification applied at temperatures of 150 °C and higher). Once at the measurement temperature, the gas supplied to the cathode was switched to humidified synthetic air.

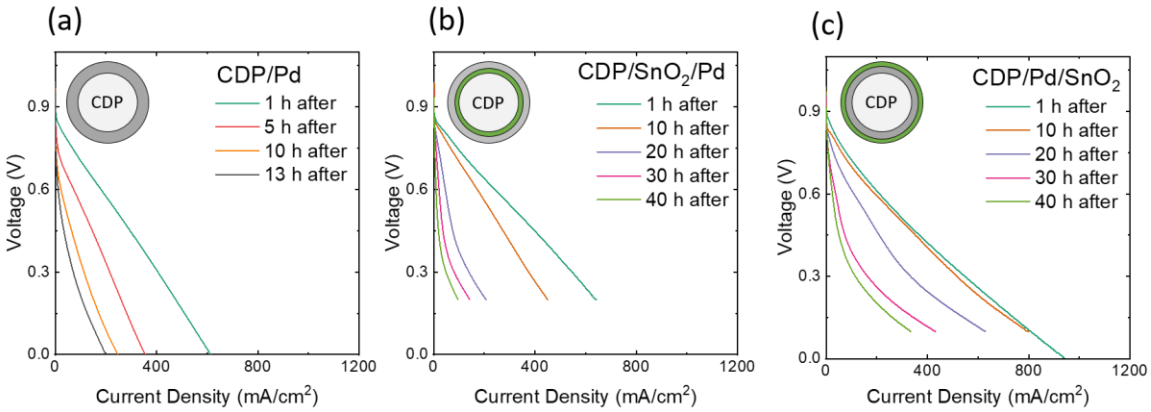

Figure 5.5 Polarization curves obtained from cells with Pd-based cathodes: (a) Pd alone on the CsH_2PO_4 particles of the cathode; (b) SnO_2 and Pd coated sequentially on the CsH_2PO_4 particles; (c) Pd and SnO_2 coated sequentially on the CsH_2PO_4 particles of the cathode. Cartoon on the top left of the graph illustrates the geometry of cathode (green shade representing SnO_2 and gray shade for Pd film).

The I-V characteristics of these three cells are shown in Figure 5.5 and IR-free polarization curves, where ohmic resistances mostly from the electrolyte are subtracted, are in Supplementary Figure 5.S1. As expected, the cell with the Pd-only cathode rapidly degrades with time. The cell with an SnO_2 overlayer on the Pd, in contrast, displays both an initial higher performance and better stability. When the SnO_2 is under Pd catalyst, on the other hand, initial performance and stability are higher than Pd-only cathode. Though, they still inferior to the those of Pd catalyst overlaid with SnO_2. The temporal evolution of the OCV and the voltage at 200 mA/cm^2 are presented in Figure 5.6, and corresponding impedance spectra under 200 mA/cm^2 bias are shown in Supplementary Figure 5.S2. The positive impact of the SnO_2 both underlayer and overlayer is clearly evident. From the comparison of the electrochemical behaviors of the cells with SnO_2/Pd and Pd/SnO_2 bilayer catalysts, applying SnO_2 film as an overlayer onto the Pd seems to be more effective approach to enhance the stability of the Pd catalyst presumably by keeping it metallic. Even though SnO_2-Pd bilayer cathodes show better performance than Pd-only, improving the stability is necessary in order to compete with the standard Pt cathode.

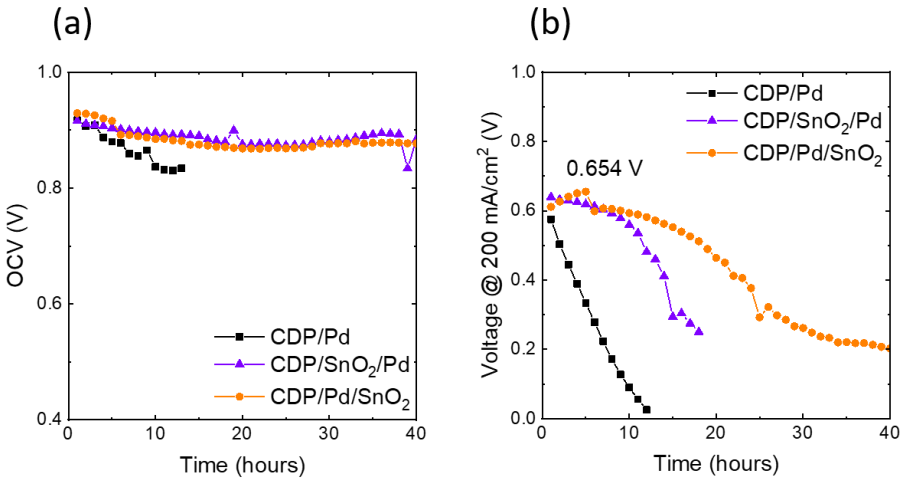

Figure 5.6 Temporal evolution of polarization characteristics of a cell fabricated with three different cathodes, Pd only (black), SnO_2/Pd (purple) and Pd/SnO_2 (orange): (a) open circuit voltage (b) voltage at 200 mA/cm^2

To examine the cause of poor stability of bilayer cathode, the cell having a SnO_2 underlayer that shows more evolution than the other bilayer was further investigated. The representative cross-sectional images of the cells after fuel cell operation are shown in Figure 5.7. In order to compare the structural evolution behavior of Pd-SnO_2 bilayer cathode, the cell with the Pt-SnO_2 bilayer cathode was prepared. The reference cathode was fabricated in a similar fashion to the Pd based cathode, as about 1nm of SnO_2 was coated onto the fine CsH_2PO_4 powders followed by MOCVD deposition of 15.5 wt% Pt. For Pt deposition, Platinum(II) acetylacetonate ($Pt(acac)_2$, $Pt(C_5H_7O_2)_2$) was used for the Pt precursor. After long-term electrochemical measurement, the microstructure of the cathode with the Pd overlayer collapses significantly and loses the porosity that is crucial for gas diffusion during

the electrochemical reaction, while the cathode powder with the Pt retains the porous structure after the measurement.

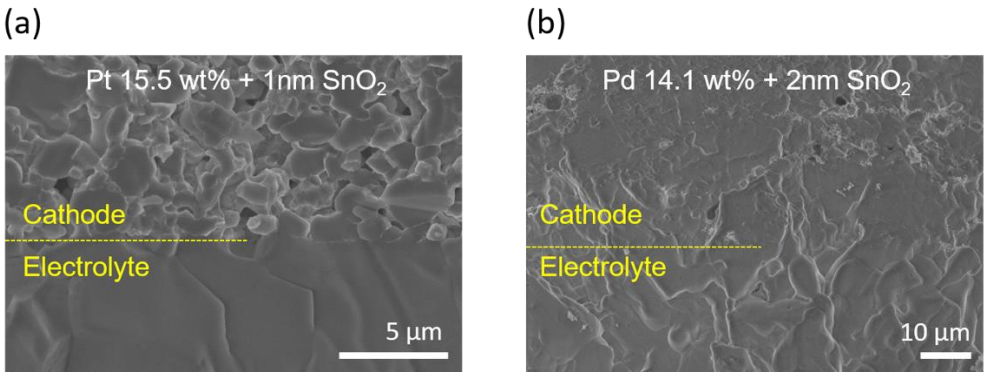

Figure 5.7 Cross-sectional SEM images of interface between electrolyte and $Pt/SnO_2/CsH_2PO_4$ cathode (a), and $Pd/SnO_2/CsH_2PO_4$ cathode (b) after fuel cell operation.

The XPS spectra on the $Pd/SnO_2/CsH_2PO_4$ cathode after annealing at the cathode condition for 6 hours are shown in Figure 5.8. Contrary to the expectation, both SnO_2 and Pd are notably oxidized. In accordance with the evidence of SEM images and XPS results shown in Figure 5.7 and 5.8, the major reason for the degradation of the cathode where the SnO_2 is between Pd and CsH_2PO_4 would be that oxidizing Pd is more favorable than forming the Sn-Pd alloy when Pd is exposed to the air. On the other hand, the stability is enhanced when Pd is covered by the SnO_2, suggesting that bilayer structure with SnO_2 overlayer is more effective to slow down the reaction between Pd and CsH_2PO_4. It is notable that initial improvement of performance for first 5 hours shown in Figure 5.6(b) is observed, yielding a voltage at 200 mA/cm^2 of 0.654 V, the highest value obtained from our group in solid acid fuel cells. One of the possible reasons for the evolution of $SnO_2/Pd/CsH_2PO_4$ would be the inherent cracks of the SnO_2 overlayer and part of Pd layer is exposed to the air, forming PdO.

Furthermore, 1nm of SnO_2 film may not be enough to convert the sufficient amount of Pd-Sn alloy, which is inactive to CsH_2PO_4, for 16.2 wt% of Pd (mole ratio of Pd to Sn is 14 to 1).

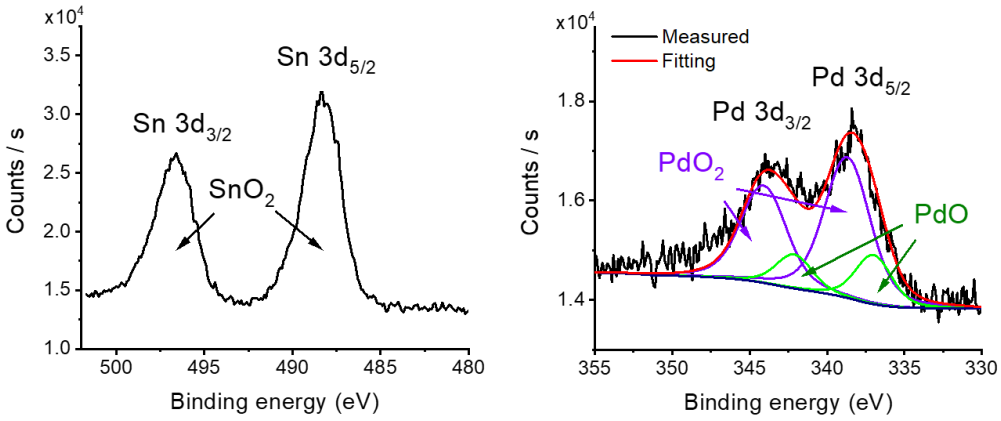

Figure 5.8 XPS spectra collected Pd/SnO_2/CsH_2PO_4 in Pd 3d and Sn 3d regions, after 6 h annealing at 250 °C under humidified air.

It is clear that cathode design with SnO_2 overlayer onto the Pd coated CsH_2PO_4 is a promising direction for developing the new cathode materials to replace the standard Pt MOCVD catalyst. Further efforts to develop the structural design of Pd-SnO_2 cathode are required to improve its stability. A possible method to do so would be finding the optimized ratio of Pd and SnO_2 and ensuring the defect-less continuous SnO_2 coating.

5.4 Conclusion

The cathode performance of Pd-SnO_2 bilayer deposited on CsH_2PO_4 powders was evaluated for SAFC application. Positive results of introducing a SnO_2 overlayer onto the Pd

coated CsH_2PO_4 cathode imply the possibility of overcoming the major challenge of utilizing Pd for the cathode catalyst. The fact that Pd oxidizes to PdO and reacts with CsH_2PO_4 under cathode condition has obstructed using Pd as a catalyst for the oxygen reduction reaction. The formation of Pd-Sn alloy that is stable with CsH_2PO_4 is achieved when SnO_2 and Pd are annealed together under the cathode condition and Pd stays in a metallic phase. This finding suggests a new approach for designing the cathode materials for SAFCs. Applying SnO_2 on top of Pd is more effective than SnO_2 underneath of Pd for the performance stability during the cell operation. It is supposed that Pd exposed to the air tends to be oxidized rather than to form Pd-Sn alloy with underlying SnO_2, while SnO_2 coating on Pd lowers the tendency for Pd oxidized. Finding the optimized thickness of SnO_2 and Pd and controlling the film quality need to be conducted for future work to enhance the performance stability in order to compete with the standard Pt based cathode.

5.5 Supplementary information

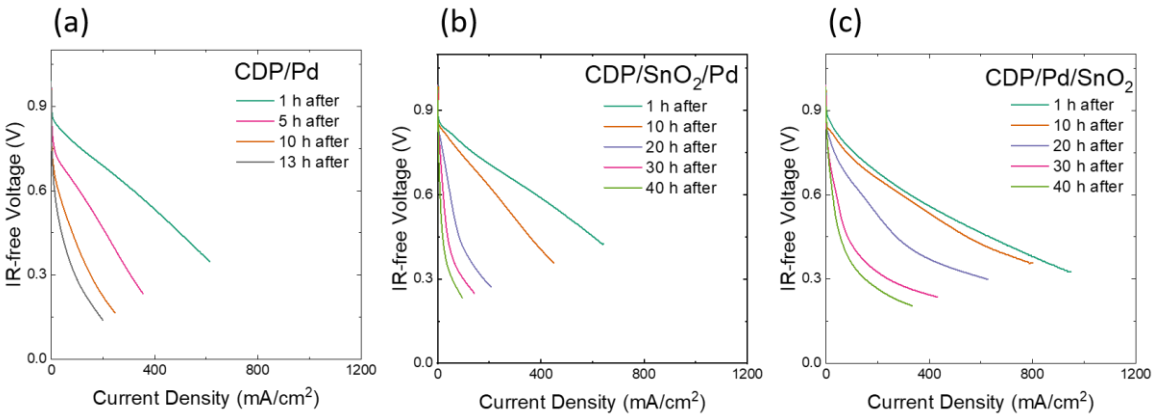

Figure 5.S1 IR-free polarization curves obtained from cells with Pd-based cathodes: (a) Pd alone on the CsH_2PO_4 particles of the cathode; (b) SnO_2 and Pd coated sequentially on the CsH_2PO_4 particles; (c) Pd and SnO_2 coated sequentially on the CsH_2PO_4 particles of the cathode

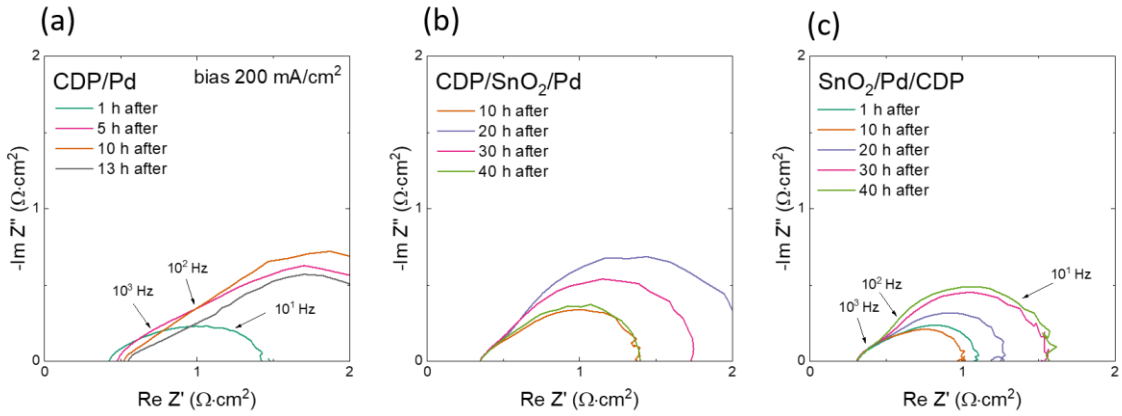

Figure 5.S2 Impedance spectra collected under bias of 200 mA/cm^2 for the cells with Pd-based cathodes: (a) Pd alone on the CsH_2PO_4 particles of the cathode; (b) SnO_2 and Pd coated sequentially on the CsH_2PO_4 particles; (c) Pd and SnO_2 coated sequentially on the CsH_2PO_4 particles of the cathode. These impedance spectra correspond to the data points in Figure 5.6(b)

Appendix A

ATOMIC LAYER DEPOSITION OF PLATINUM THIN FILM ON SOLID ACID ELECTROLYTE POWDERS

Lim, D.-K, Liu J., Pandey S. A., Paik, H., Chisholm, C. R. I., Hupp, J. T., Haile, S. M., Atomic layer deposition of Pt@CsH_2PO_4 for the cathodes of solid acid fuel cells, *Electrochimica Acta*, **288**, 12 (2018) doi : 10.1016/j.electacta.2018.07.076

Typical cathode composite in a solid acid fuel cell (SAFC) is prepared by Pt deposition on CsH_2PO_4 powders using metal organic chemical vapor deposition (MOCVD). This technique, however, does not lend itself to precise control of Pt morphology. In turn, this suggests challenges in tuning the process for optimal Pt utilization and in using such structures for elucidating the critical factors determining the oxygen reduction rate. Furthermore, degradation of the cathode created by this process was noted as a remaining challenge.[21]

Atomic layer deposition (ALD) has emerged as a remarkable process for deposition of conformal films of a wide variety of materials on an equally wide variety substrates.[75] The self-limiting adsorption behavior of the reactants used in the process affords exquisite control of film thickness. While preparation of metallic films by ALD is less developed than that of oxides, several reports of Pt growth appear in the literature,[76] suggesting its suitability as a method for obtaining Pt coated CsH_2PO_4. These prior studies use as the metal precursor either ($Pt(acac)_2$) or (methylcyclopentadienyl)trimethylplatinum ($MeCpPtMe_3$), and as the oxidant, either O_2, oxygen plasma, or O_3 (ozone).[77,78] Here we select $MeCpPtMe_3$ and ozone for Pt deposition on CsH_2PO_4 because growth temperatures as low as 100 °C with growth

rates on the order of 0.45 Å/cycle have been demonstrated for this combination.[78] These conditions are compatible with CsH_2PO_4, which unless held under high steam partial pressures, undergoes a slow and highly detrimental dehydration/decomposition reaction at temperatures above ~150 °C.[71] We examine the impact of varying the number of ALD cycles on both deposition characteristics and fuel cell polarization behavior.

ALD preparations were carried out using a pulse type Savannah 100 reactor (Cambridge Nanotech, Inc.) with 80 mg of CsH_2PO_4 powders loaded into the reactor for each deposition. Prior to the delivery of reactant gases, the CsH_2PO_4 was vacuum heat-treated for 30 min at 150 °C to remove any physisorbed water. The CsH_2PO_4 powder was then held at 150 °C for the subsequent deposition. The solid platinum precursor was pulsed at a temperature of 75 °C, using ultra-high purity nitrogen as the carrier, which also served as the purge gas. Each deposition cycle consisted of the following five steps: (1) 1 s pulse of $MeCpPtMe_3$; (2) 220 s hold to provide time for the precursor to diffuse throughout the powder; (3) 220 s N_2 purge; (4) 45 s pulse of O_3; (5) 45 s N_2 purge. This sequence of ALD steps was then repeated, between 100 and 450 times. Sample nomenclature hereafter follows the system Pt-xxx, where xxx is the number of cycles. The Pt-100 and Pt-200 preparations were duplicated to evaluate reproducibility.

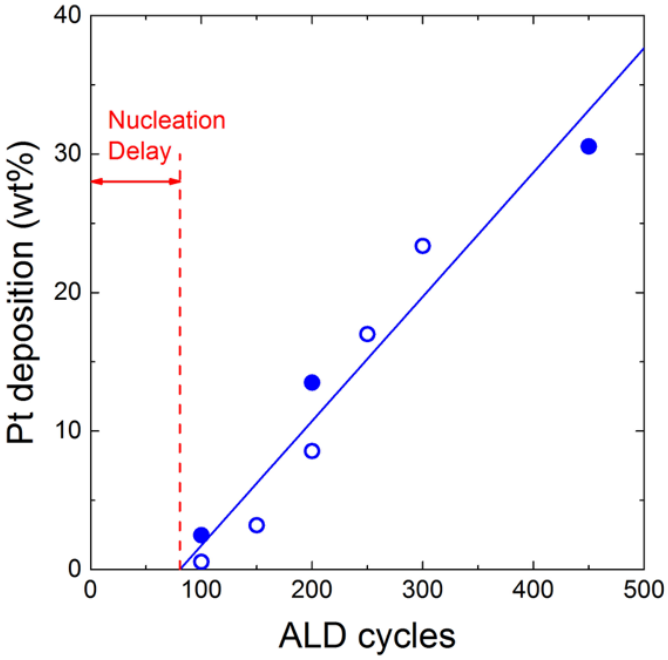

Figure A.1 Pt deposition on CsH_2PO_4 powder as a function of number of ALD cycles. The open symbols indicate Pt@ CsH_2PO_4 materials utilized in subsequent characterization, including fuel cell evaluation.

Deposition of Pt on CsH_2PO_4 powders was achieved, with amounts ranging from 0.6 to 30 wt% Pt for the range of cycle numbers utilized (100 – 450), Figure A.1. The Pt yield, a comparison of the quantity of Pt supplied to the system to the quantity deposited on the powder, is below 1 % (ranging from ~0.5 % for Pt-100 to ~0.8 % for Pt-300). The Pt growth was found to occur in a two-stage process as evidenced, not only from the amount of Pt deposited as a function of the number of cycles, but also the scanning electron microscope (SEM) imaging, Figures A.2 and the diffraction patterns, Figure A.3. In the first stage, of about 80 cycles, minimal deposition occurred. Specifically, after 100 ALD cycles an average of only 1.5 wt% Pt was deposited (Figure A.1). Moreover, for the Pt-100 materials with 0.56 wt% Pt, the metal was essentially undetectable in the X-ray diffraction pattern (Figure A.3),

and the SEM image, Figure A.2b, reveals the presence of isolated Pt nanoparticle clusters on the surface of the large CsH_2PO_4 particles. In the second stage, the deposition amount varied linearly with the number of ALD cycles. The deposition behavior was found to be reasonably reproducible, as indicated by the low scatter in the data ($R^2 = 0.93$). Unless stated otherwise, the samples with lesser Pt amounts from the two duplicated depositions, Pt-100 and Pt-200, were used for subsequent studies, including the SEM imaging and diffraction analysis (Figures A.2 and A.3).

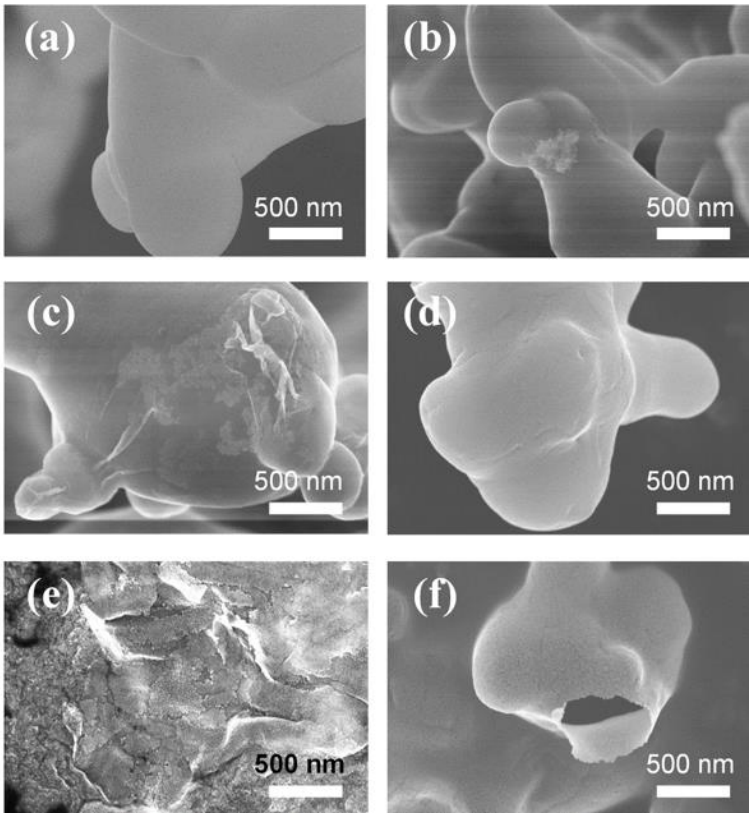

Figure A.2 Scanning electron microscopy images showing nature of ALD-Pt on CsH_2PO_4: (a) bare CsH_2PO_4, (b) as-deposited Pt-100, (c) as-deposited Pt-150, (d) as-deposited Pt-200, (e) Pt-150 after dissolution of CsH_2PO_4, and (f) Pt-200 after dissolution of CsH_2PO_4.

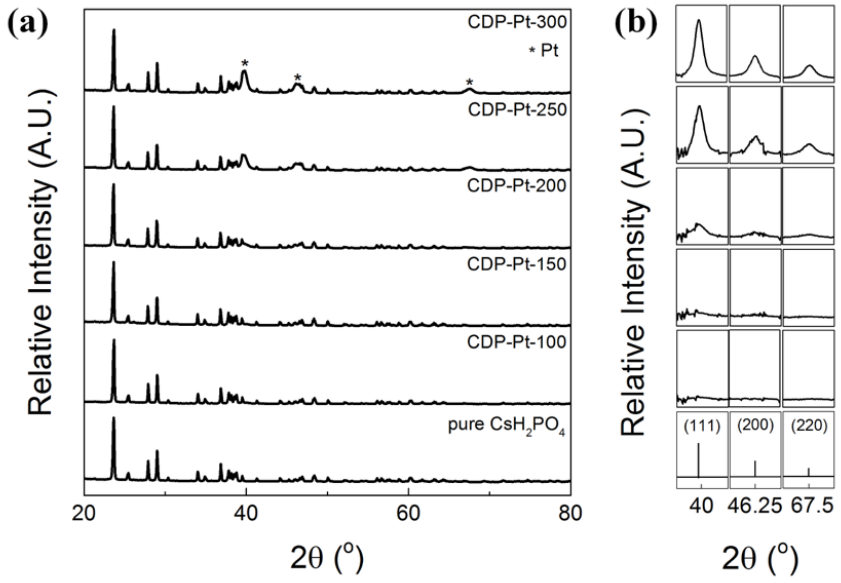

Figure A.3 X-ray diffraction patterns from neat CsH_2PO_4 and from as-prepared Pt@ CsH_2PO_4 particles: (a) raw diffraction patterns, and (b) residual peaks after subtraction of CsH_2PO_4 pattern, revealing Pt peaks.

We attribute the two-stage deposition behavior of Pt on CsH_2PO_4 to a nucleation delay prior to the onset of layer-by-layer growth. An incubation period for ALD growth of metals onto oxides has been observed in many systems, and is not surprising here.[79-82] During the incubation period, rather than the deposition of uniform, monoatomic layers of the metal, isolated nanoparticles, as exemplified in Figure A.2(b), are formed as a result of the high surface energy between substrate and deposit. These nuclei undergo very slow lateral growth (or additional nuclei are formed at a slow rate), until a continuous film is eventually attained. Linear growth occurs in the second stage, consistent with the self-limiting nature of the ALD process. The growth rate of Pt on CsH_2PO_4 in this latter regime is found to be 0.09 ± 0.01 wt% cycle, which corresponds to ~0.02 nm/cycle, as estimated on the basis of the CsH_2PO_4 specific surface area of 2.4 m^2/g. The zero-growth intercept is 84 ± 20 cycles. The transition

between films with discontinuous and continuous morphology as a function of number of ALD cycles is not sharp. Specifically, the SEM image of the Pt-150 material, with a Pt content of 3.2 wt%, reveals a Pt film that is generally interconnected, though clearly not yet continuous (Figure A.2(c, e)). After 200 cycles, the resulting film is entirely continuous (Figure A.2(d)); a large defect in the free-standing Pt-200 film (Figure A.2(f)) is a result of the handling involved in removal by dissolution of the underlying CsH_2PO_4. As a consequence of the limited thickness of the films (Figure A.2(f)), the micron scale surface morphology of the Pt@CsH_2PO_4 is largely unchanged from that of the neat CsH_2PO_4 material.

The slight variation in the deposition efficiency observed in the Pt-100 and Pt-200 experiments is attributed to variations in the nature of the CsH_2PO_4 surface, which would likely impact the nucleation characteristics. In addition, variation in the precursor vapor pressure, as a consequence of depletion of the source tank, may have played a role. This result indicates that in order to capitalize on the precise control of film thickness otherwise offered by ALD, enhanced control of the Pt nucleation behavior and process parameters may be desirable.

Appendix B

CAESIUM NITRATE DOPING EFFECT ON ANODE CATALYTIC ACTIVITY IN SOLID ACID FUEL CELLS

As we discussed in chapter 3 and 4, CsOH/Cs_2O, which is a byproduct after reaction of Pd and CsH_2PO_4, have been considered as a material might give a positive impact on hydrogen oxidation reaction at the anode of SAFCs. We also have a preliminary result that a small amount of CsOH added into standard Pt anode seems to improve the kinetics of oxidation of hydrogen from the ammonia decomposition study using a solid acid electrochemical cell. In order to find the best doping concentration of Cs compounds in the anode to promote the catalytic activity, we devised the systematic study testing anode symmetric cells with several different concentrations of Cs compounds.

The easiest way to study the impact of CsOH on standard Pt-based anode composite is by mixing two materials with an appropriate ratio and using it to make an anode layer of an electrochemical cell. However, the hygroscopic nature of CsOH absorbs the water molecules from the atmosphere quickly. This property makes difficult to measure the exact weight of CsOH and control the exact mass ratio of CsOH and Pt anode composites. Instead, we choose $CsNO_3$ as Cs compound because it has been known that $CsNO_3$ decomposes into CsOH under the H_2 environment at high temperature with a present of metal catalyst.[83] In order to confirm $CsNO_3$ is converted into CsOH with Pt catalyst, mass change of mixture of

$CsNO_3$ and Pt catalyst was observed under the humidified H_2 at 250 °C through the thermogravimetric analysis (TGA).

$CsNO_3$ (Alfa Aesar, 99.9%) was mechanically mixed with Pt 40 wt% on carbon (Alfa Aesar) with 12.9 mg and 20 mg respectively. Mixture and TGA sample holder were dried in oven at 80 °C overnight to remove water molecules. After measuring the exact weight of the mixture, TGA was conducted while the temperature increased up to 250 °C with the ramping rate of 2 °C/min. Mixture gas of 3 % H_2 and 97 % Ar flowed into the instrument chamber through the water bubbler chilled at 18 °C. Gas carried 0.02 atm of water molecules. After 4 hours measurement, the gas mixture directly flowed into the chamber skipping the water bubbler and measured the weight loss at 250 °C for next 2 hours. The analysis ended after additional 2 hours measurement with humidified gas again.

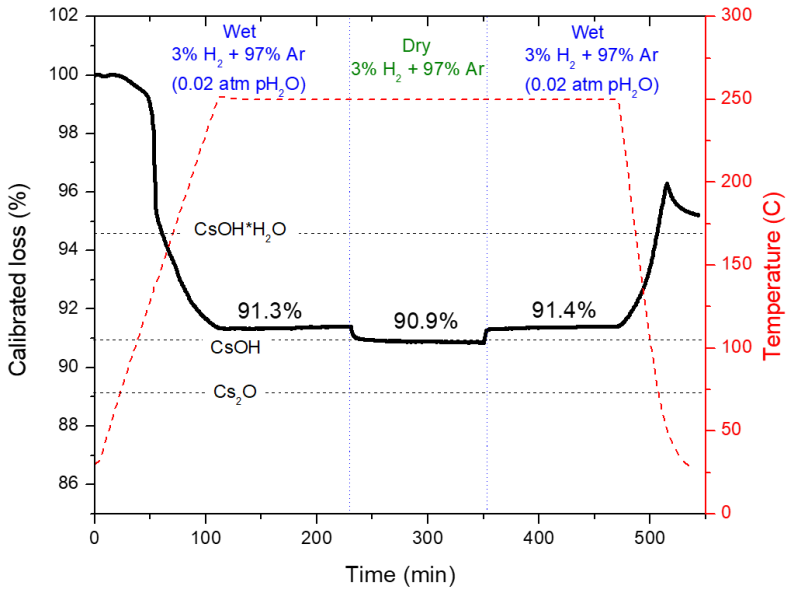

Figure B.1 Thermogravimetric analysis of 40 wt% Pt on carbon and $CsNO_3$. Materials examined at 250 °C upon exposure sequentially to lightly humidified 3% H_2, dry 3% H_2, and then returned to lightly humidified 3% H_2

Figure B.1 shows the weight loss of $CsNO_3$ with different gas conditions and temperatures. Weight loss of $CsNO_3$ was calculated by subtracting the weight change of Pt 40 wt% on carbon only, which was measured separately under the same experimental condition profile. If the measurement was well controlled and there was no any other mass loss except the decomposition of $CsNO_3$, expected mass change by converting into CsOH was 90.9 %, Cs_2O was 89.1 %, $CsOH{\cdot}H_2O$ was 94.6 % from the 100% of $CsNO_3$. Mass of $CsNO_3$ gradually reduced as temperature increased and became as 91.3 % of initial mass under humidified H_2, indicating that $CsNO_3$ was decomposed into partially hydrated CsOH. It fully converted into CsOH under the dry gas as mass changed to 90.9 % and backed to partially hydrated CsOH when the humidified gas was applied again. This result shows that

$CsNO_3$ eventually becomes to CsOH at the anode condition in SAFC when Pt catalyst presents. After finishing TGA on Cs compounds with Pt catalyst, the X-ray diffraction study was conducted for the mixture. There were not crystalline diffraction peaks except Pt, indicating that products of CsOH or hydrated CsOH had amorphous structure.

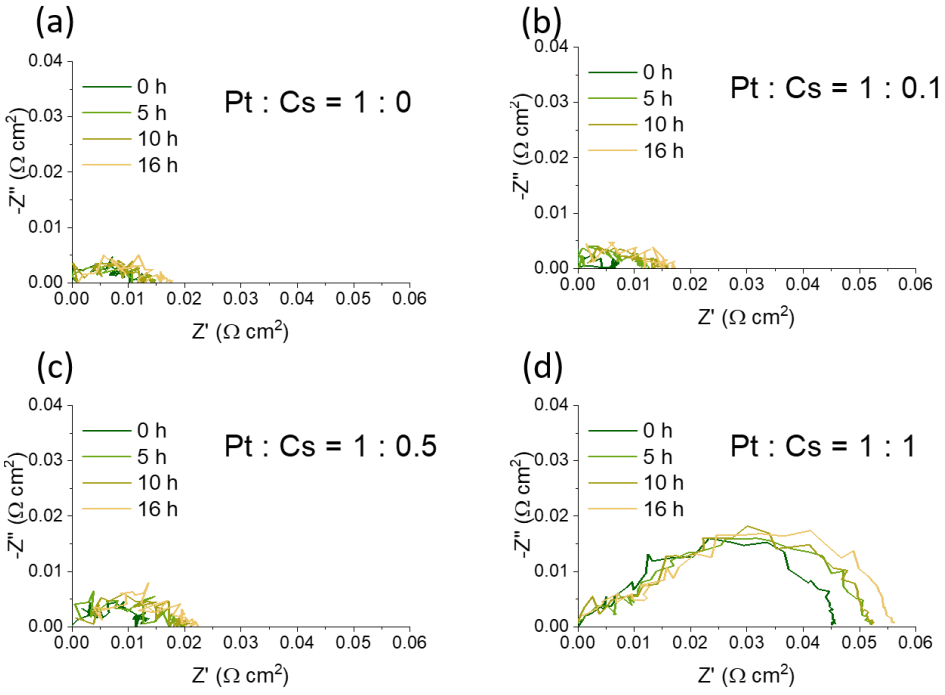

Figure B.2 Impedance spectra with time under SAFC anode conditions (T = 248 °C, pH_2 = 0.6 atm, pH_2O = 0.4 atm) at zero bias. Anode is composed with Pt/C, CsH_2PO_4, and $CsNO_3$. Pt : Cs indicates the mole ratio of Pt and Cs in $CsNO_3$.

After confirming $CsNO_3$ can be used as a precursor of CsOH, $CsNO_3$ was mixed with standard Pt anode composite with three different mole ratios of Cs : Pt, such as 0.1 : 1, 0.5 : 1, and 1 : 1. First, $CsNO_3$ was dissolved in deionized water and added into Pt on carbon (20 wt% Pt on carbon black, HiSPEC® 3000, Alfa Aesar) with desired concentration of Cs. After drying the mixture at 50 °C overnight, it mechanically mixed with fine powder of CsH_2PO_4

in 1 : 6 weight ratio of $CsNO_3$/Pt/C to CsH_2PO_4 using a mortar and a pestle in a glove box. The 50 mg of composites were spread on both sides of CsH_2PO_4 membrane and pressed together in 69 MPa for a minute to make an anode symmetric cell. Carbon paper and stainless steel meshes were placed on both sides as a current collector/gas diffusion layer (GDL) and Teflon tape wrapped the perimeter of the electrochemical cell.

The electrochemical properties of $CsNO_3$ doped Pt anodes were characterized by AC impedance measurement under uniform humidified H_2 (pH_2O = 0.38 atm) at 250 °C. Figure B.2 represents the sum of impedance responses from both sides of anodes, collected for 16 hours. For ease of comparison between spectra, non-electrode contributions (ohmic resistances) are subtracted from the impedance data. When the mole ratio of Cs to Pt is higher than 0.5, anode catalytic activities of $CsNO_3$/Pt/C, which eventually converted into CsOH/Pt/C, are lower than only Pt/C composite. However, when Cs compounds are added to Pt/C composite with Cs : Pt = 0.1 : 1, anode resistance is comparable to the one without Cs doping. It is clear that more than a certain amount of Cs compounds impedes the Pt standard anode catalytic activity. When the ratio of Cs and Pt is 1 : 1, the impedance spectra have a half-teardrop shape, which is a characteristic feature of Warburg impedance element, implying that there might be a diffusion rate limiting step.

There are a couple of possible explanations on the comparable impedance results of Pt only and $CsNO_3$/Pt anodes. First is that low concentration of $CsNO_3$ or CsOH, which is not mixed evenly through the Pt composite, is not enough to give an impact on the catalytic activity. In fact, mixing $CsNO_3$ and Pt is tricky because $CsNO_3$ tends to crystallize into a coarse particle when deionized water evaporates. We could improve the distribution of Cs

compounds more evenly by employing different deposition techniques, such as a rotary evaporator. Another possible reason is the optimized ratio of Cs to Pt exists between 0 to 0.1. According to the previous work, we indeed had observed the improvement of anode catalytic activity by a trace of Cs compounds added into Pt-based anode composite.

In addition, the sum of two anodes resistance values from Pt-only catalyst here is lower than the known Pt standard anode, which is ~0.05 $\Omega\,cm^2$[215]. There are several differences in procedures on preparing and measuring the samples between this work and the work by Lim *et al*. The major reason would be the difference in the amount of anode composite as 50 mg, which is twice more than the one by Lim *et al*. Also, anode/electrolyte/anode powders are spread in sequent and pressed together in 69 MPa here, while the standard anode is prepared by spreading on top of GDL/microporous layer (MPL) and pressed at 103.5 MPa and electrolyte powder is placed on top of the anode layer and pressed at 138 MPa. Thus, the anode layer in this work is made with twice amount of composite and pressed at half of the pressure than the standard anode, resulting in increasing the number of active sites and porosity in the anode layer. Besides, another minor difference, which hardly effects on the anode reaction rate, is that a carbon paper is used for the current collector instead of MPL.

In conclusion, $CsNO_3$ is decomposed into amorphous CsOH in humidified H_2 condition at 250 °C in the presence of the Pt catalyst. Effect of $CsNO_3$ on anode catalytic activity is evaluated by adding it into Pt-based standard anode composite with various concentration. When the mole ratio of Cs to Pt is higher than 0.5, anode electrochemical resistance increases. On the other hand, the anode composite with Cs : Pt ratio of 0.1 : 1, the

hydrogen oxidation reaction is comparable with the one without Cs doping. In order to conclude the positive effect of CsOH on anode catalytic activity in SAFC system, elaborate experimental design is required. Different Cs compounds deposition method, such as a rotary evaporator, should employ instead of the mortar and pestle mixing method to disperse Cs compounds more evenly over the Pt anode composite. Based on this work, the optimized ratio of Cs to Pt is expected to exist between 0 to 0.5.

BIBLIOGRAPHY

1. Haile, S. M., Boysen, D. A., Chisholm, C. R. I. & Merle, R. B. Solid acids as fuel cell electrolytes. *Nature* **410,** 910–913 (2001).
2. Haile, S. M., Chisholm, C. R., Sasaki, K., Boysen, D. A. & Uda, T. Solid acid proton conductors: from laboratory curiosities to fuel cell electrolytes. *Faraday Discuss.* **134,** 17–39 (2007).
3. Boysen, D. A., Uda, T., Chisholm, C. R. I. & Haile, S. M. High-Performance Solid Acid Fuel Cells Through Humidity Stabilization. *Science* **303,** 68–70 (2004).
4. Uda, T. & Haile, S. M. Thin-Membrane Solid-Acid Fuel Cell. *Electrochem. Solid-State Lett.* **8,** A245–A246 (2005).
5. Carrette, L., Friedrich, K. A. & Stimming, U. Fuel cells: principles, types, fuels, and applications. *ChemPhysChem* **1,** 162–193 (2000).
6. Haile, S. M. Materials for fuel cells. *Materials Today* (2003).
7. O'Hayre, R., Cha, S.-W., Colella, W. & Prinz, F. B. *Fuel Cell Fundamentals*. (John Wiley & Sons, 2016).
8. Medford, A. J. *et al.* From the Sabatier principle to a predictive theory of transition-metal heterogeneous catalysis. *Journal of Catalysis* **328,** 36–42 (2015).
9. Appleby, A. J. Electrocatalysis and Fuel Cells. *Catalysis Reviews* **4,** 221–244 (1971).
10. Chisholm, C. R. *et al.* From Laboratory Breakthrough to Technological Realization: The Development Path for Solid Acid Fuel Cells. *Electrochem Soc Interface* **18,** 53 (2009).
11. Taninouchi, Y.-K., Uda, T., Awakura, Y., Ikeda, A. & Haile, S. M. Dehydration behavior of the superprotonic conductor CsH_2PO_4 at moderate temperatures: 230 to 260 °C. *J. Mater. Chem.* **17,** 3182–3189 (2007).
12. Taninouchi, Y.-K., Uda, T. & Awakura, Y. Dehydration of CsH_2PO_4 at temperatures higher than 260 °C and the ionic conductivity of liquid product. *Solid State Ionics* **178,** 1648–1653 (2008).

13. Bronowska, W. & Pietraszko, A. X-ray study of the high-temperature phase transition of CsH_2PO_4 crystals. *Solid State Communications* **76,** 293–298 (1990).
14. Louie, M. W. C. Electrocatalysis in Solid Acid Fuel Cells. Ph.D. thesis, California Institute of Technology, California, United States (2011).
15. Lim, D.-K. *et al.* Atomic layer deposition of Pt@CsH_2PO_4 for the cathodes of solid acid fuel cells. *Electrochim. Acta* **288,** 12–19 (2018).
16. Uda, T., Boysen, D. A., Chisholm, C. R. I. & Haile, S. M. Alcohol Fuel Cells at Optimal Temperatures. *Electrochem. Solid-State Lett.* **9,** A261–4 (2006).
17. Mohtadi, R., Lee, W. K. & Van Zee, J. W. Assessing durability of cathodes exposed to common air impurities. *Journal of Power Sources* **138,** 216–225 (2004).
18. Louie, M. W., Sasaki, K. & Haile, S. Towards Understanding Electrocatalysis in CsH_2PO_4-Based Fuel Cells: Platinum and Palladium Thin Film Electrodes. *ECS Transactions* **13,** 57–62 (2008).
19. Papandrew, A. B., Chisholm, C. R. I., Zecevic, S. K., Veith, G. M. & Zawodzinski, T. A. Activity and Evolution of Vapor Deposited Pt-Pd Oxygen Reduction Catalysts for Solid Acid Fuel Cells. *J. Electrochem. Soc.* **160,** F175–F182 (2013).
20. Papandrew, A. B., John, S. S. & Elgammal, R. A. Vapor-Deposited Pt and Pd-Pt Catalysts for Solid Acid Fuel Cells: Short Range Structure and Interactions with the CsH_2PO_4 Electrolyte. *J. Electrochem. Soc.* **163,** F464–F469 (2016).
21. Papandrew, A. B., Chisholm, C. R. I., Elgammal, R. A., Oezer, M. M. & Zecevic, S. K. Advanced Electrodes for Solid Acid Fuel Cells by Platinum Deposition on CsH_2PO_4. *Chem. Mater.* **23,** 1659–1667 (2011).
22. Varga, Á., Brunelli, N. A., Louie, M. W., Giapis, K. P. & Haile, S. M. Composite nanostructured solid-acid fuel-cell electrodes via electrospray deposition. *J. Mater. Chem.* **20,** 6309 (2010).
23. Varga, Á. *et al.* Carbon nanotubes as electronic interconnects in solid acid fuel cell electrodes. *Phys. Chem. Chem. Phys.* **15,** 15470 (2013).

24. Thoi, V. S., Usiskin, R. E. & Haile, S. M. Platinum-decorated carbon nanotubes for hydrogen oxidation and proton reduction in solid acid electrochemical cells. *Chem. Sci.* **6,** 1570–1577 (2015).
25. Papandrew, A. B. & Zawodzinski, T. A. J. Nickel catalysts for hydrogen evolution from CsH_2PO_4. *Journal of Power Sources* **245,** 171–174 (2014).
26. Papandrew, A. B., Atkinson, R. W., III, Unocic, R. R. & Zawodzinski, T. A. Ruthenium as a CO-tolerant hydrogen oxidation catalyst for solid acid fuel cells. *J. Mater. Chem. A* **3,** 3984–3987 (2015).
27. Louie, M. W. & Haile, S. M. Platinum thin film anodes for solid acid fuel cells. *Energy Environ. Sci.* **4,** 4230 (2011).
28. Sasaki, K. A., Hao, Y. & Haile, S. M. Geometrically asymmetric electrodes for probing electrochemical reaction kinetics: a case study of hydrogen at the Pt–CsH_2PO_4 interface. *Phys. Chem. Chem. Phys.* **11,** 8349–8357 (2009).
29. Paik, H., Berenov, A. V., Skinner, S. J. & Haile, S. M. Hydrogen oxidation kinetics on platinum-palladium bimetallic thin films for solid acid fuel cells. *APL Materials* **7,** 013201 (2019).
30. Lohmann-Richters, F. P., Abel, B. & Varga, Á. In situ determination of the electrochemically active platinum surface area: key to improvement of solid acid fuel cells. *J. Mater. Chem. A* **6,** 2700–2707 (2018).
31. Gobbi, A. L. & Nascente, P. A. P. in *Encyclopedia of Tribology* (eds. Wang, Q. J. & Chung, Y.-W.) 699–706 (Springer US, 2013).
32. Wasa, K., Kanno, I. & Kotera, H. *Handbook of sputter deposition technology: fundamentals and applications for functional thin films, nano-materials and MEMS*. (2012).
33. Taga, Y. & Takahasi, R. Role of kinetic energy of sputtered particles in thin film formation. *Surf. Sci.* **386,** 231–240 (1997).
34. Thornton, J. A. Influence of substrate temperature and deposition rate on structure of thick sputtered Cu coatings. *J. Vac. Sci. Technol.* **12,** 830–835 (1975).

35. Evoen, V. Electrocatalysis in Solid Acid Fuel Cell Electrodes. Ph.D. thesis, California Institute of Technology, California, United States (2016).
36. Zoski, C. G. *Handbook of Electrochemistry*. (Elsevier, 2007).
37. Wu, W.-P. & Jiang, J.-J. Effect of plating temperature on electroless amorphous Ni–P film on Si wafers in an alkaline bath solution. *Applied Nanoscience* 1–10 (2017).
38. Louie, M. W., Hightower, A. & Haile, S. M. Nanoscale Electrodes by Conducting Atomic Force Microscopy: Oxygen Reduction Kinetics at the Pt|$CsHSO_4$ Interface. *ACS Nano* **4,** 2811–2821 (2010).
39. Varga, Á. Advancing Electrocatalysis in Solid Acid Fuel Cells. Ph.D. thesis, California Institute of Technology, California, United States (2013).
40. Springer, T. E., Zawodzinski, T. A., Wilson, M. S. & Gottesfeld, S. Characterization of Polymer Electrolyte Fuel Cells Using AC Impedance Spectroscopy. *J. Electrochem. Soc.* **143,** 587–599 (1996).
41. Barsoukov, E. & Macdonald, J. R. *Impedance Spectroscopy*. (John Wiley & Sons, 2005).
42. Bard, A. J. & Faulkner, L. R. *Electrochemical Methods: Fundamentals and Applications, 2nd Edition*. (Wiley Global Education, 2000).
43. Orazem, M. E. & Tribollet, B. *Electrochemical Impedance Spectroscopy*. (John Wiley & Sons, 2017).
44. Sasaki, K. A. Electrochemical characterization of solid acid fuel cell electrodes. (2010).
45. Papandrew, A. B. *et al.* Electrochemical Hydrogen Separation via Solid Acid Membranes. *J. Electrochem. Soc.* **161,** F679–F685 (2014).
46. Miller, M. K., Russell, K. F., Thompson, K., Alvis, R. & Larson, D. J. Review of atom probe FIB-based specimen preparation methods. *Microsc. Microanal.* **13,** 428–436 (2007).

47. Rego, R., Ferraria, A. M., do Rego, A. M. B. & Oliveira, M. C. Development of PdP nano electrocatalysts for oxygen reduction reaction. *Electrochim. Acta* **87,** 73–81 (2013).
48. Okamoto, H. *Pd-Pt (Palladium-Platinum).* **3,** 3033–3034 (Binary Alloy Phase Diagrams, II Ed., Ed. T.B. Massalsk, 1990).
49. Manova, D., Gerlach, J. W. & Mändl, S. Thin film deposition using energetic ions. *Materials* **3,** 4109–4141 (2010).
50. Nicolet, M. A. Diffusion barriers in thin films. *Thin Solid Films* **52,** 415–443 (1978).
51. Prins, R. & Bussell, M. E. Metal Phosphides: Preparation, Characterization and Catalytic Reactivity. *Catal Lett* **142,** 1413–1436 (2012).
52. Xiao, P., Chen, W. & Wang, X. A Review of Phosphide-Based Materials for Electrocatalytic Hydrogen Evolution. *Adv. Energy Mater.* **5,** 1500985–13 (2015).
53. Kibsgaard, J. *et al.* Designing an improved transition metal phosphide catalyst for hydrogen evolution using experimental and theoretical trends. *Energy Environ. Sci.* **8,** 3022–3029 (2015).
54. Kucernak, A. R. J., Fahy, K. F. & Sundaram, V. N. N. Facile synthesis of palladium phosphide electrocatalysts and their activity for the hydrogen oxidation, hydrogen evolutions, oxygen reduction and formic acid oxidation reactions. *Catalysis Today* **262,** 48–56 (2016).
55. Cheng, L., Zhang, Z., Niu, W., Xu, G. & Zhu, L. Carbon-supported Pd nanocatalyst modified by non-metal phosphorus for the oxygen reduction reaction. *Journal of Power Sources* **182,** 91–94 (2008).
56. Izhar, S. & Nagai, M. Transition metal phosphide catalysts for hydrogen oxidation reaction. *Catalysis Today* **146,** 172–176 (2009).
57. Luo, F. *et al.* Palladium Phosphide as a Stable and Efficient Electrocatalyst for Overall Water Splitting. *Angew. Chem. Int. Ed.* **57,** 14862–14867 (2018).
58. Okamoto, H. *P-Pd (Phosphorus-Palladium).* 2971–2972 (Binary Alloy Phase Diagrams, II Ed., Ed. T.B. Massalski, 1990).

59. Flanagan, T. B., Bowerman, B. S., Rundqvist, S. & Andersson, Y. Solution of hydrogen and deuterium in palladium phosphide, Pd_6P. *J. Chem. Soc., Faraday Trans. 1* **79,** 1605–12 (1983).

60. Flanagan, T. B., Biehl, G. E., Clewley, J. D., Rundqvist, S. & Andersson, Y. Solution of hydrogen in non-stoichiometric Pd_3P_{1-x} compounds. *J. Chem. Soc., Faraday Trans. 1* **76,** 196–13 (1980).

61. Cullity, B. D. & Stock, S. R. *Elements of X-ray Diffraction, Third Edition*. (Prentice-Hall, 2001).

62. Andersson, Y., Rundqvist, S., Tellgren, R., Thomas, J. O. & Flanagan, T. B. A Neutron-Diffraction Investigation of Deuterated $Pd_3P_{0.80}$. *Journal of Solid State Chemistry* **32,** 321–327 (1980).

63. Belykh, L. B., Skripov, N. I., Sterenchuk, T. P., Umanets, V. A. & Schmidt, F. K. Pd–P Hydrogenation Catalyst: Nanoparticle Nature and Surface Layer State. *NANO* **11,** 1650065–14 (2016).

64. Carenco, S. *et al.* Structural transitions at the nanoscale: the example of palladium phosphides synthesized from white phosphorus. *Dalton Trans.* **42,** 12667–8 (2013).

65. Fultz, B. & Howe, J. *Transmission Electron Microscopy and Diffractometry of Materials*. (Springer Science & Business Media, 2013).

66. Sahm, T., Gurlo, A., Bârsan, N. & Weimar, U. Basics of oxygen and SnO_2 interaction; work function change and conductivity measurements. *Sensors and Actuators B: Chemical* **118,** 78–83 (2006).

67. Batzill, M. & Diebold, U. The surface and materials science of tin oxide. *Prog. Surf. Sci.* **79,** 47–154 (2005).

68. Watanabe, M., Venkatesan, S. & Laitinen, H. A. Preparation of Dispersed Platinum on Conductive Tin Oxide and Its Catalytic Activity for Oxygen Reduction. *J. Electrochem. Soc.* **130,** 59–64 (1983).

69. Baker, W. S. *et al.* Enhanced Oxygen Reduction Activity in Acid by Tin-Oxide Supported Au Nanoparticle Catalysts. *J. Electrochem. Soc.* **153,** A1702–6 (2006).

70. Mullings, M. N., Hägglund, C. & Bent, S. F. Tin oxide atomic layer deposition from tetrakis(dimethylamino)tin and water. *J. Vac. Sci. Technol. A* **31,** 061503 (2013).

71. Ikeda, A. & Haile, S. M. The thermodynamics and kinetics of the dehydration of CsH_2PO_4 studied in the presence of SiO_2. *Solid State Ionics* **213,** 63–71 (2012).

72. Nelson, A. Co-refinement of multiple-contrast neutron/X-ray reflectivity data using MOTOFIT. *J Appl Crystallogr* **39,** 273–276 (2006).

73. Senoner, M. & Unger, W. E. S. SIMS imaging of the nanoworld: applications in science and technology. *Journal of Analytical Atomic Spectrometry* **27,** 1050–1068 (2012).

74. Okamoto, H. *Pd-Sn (Palladium-Tin).* 3049–3051 (Binary Alloy Phase Diagrams, II Ed., Ed. T.B. Massalski, 1990).

75. George, S. M. Atomic layer deposition: An overview. *Chem. Rev.* **110,** 111–131 (2010).

76. Hämäläinen, J., Ritala, M. & Leskelä, M. Atomic layer deposition of noble metals and their oxides. *Chem. Mater.* **26,** 786–801 (2014).

77. Hämäläinen, J., Munnik, F., Ritala, M. & Leskelä, M. Atomic Layer Deposition of Platinum Oxide and Metallic Platinum Thin Films from $Pt(acac)_2$ and Ozone. *Chem. Mater.* **20,** 6840–6846 (2008).

78. Dendooven, J. *et al.* Low-temperature atomic layer deposition of platinum using (methylcyclopentadienyl)trimethylplatinum and ozone. *Journal of Physical Chemistry C* **117,** 20557–20561 (2013).

79. Lee, H. B. R., Pickrahn, K. L. & Bent, S. F. Effect of O_3 on growth of pt by atomic layer deposition. *Journal of Physical Chemistry C* **118,** 12325–12332 (2014).

80. Baker, L. *et al.* Nucleation and growth of Pt atomic layer deposition on Al_2O_3 substrates using (methylcyclopentadienyl)-trimethyl platinum and O_2 plasma. *J. Appl. Phys.* **109,** 084333 (2011).

81. Kim, S. K., Han, J. H., Kim, G. H. & Hwang, C. S. Investigation on the growth initiation of Ru thin films by atomic layer deposition. *Chem. Mater.* **22,** 2850–2856 (2010).

82. Elam, J. W., Zinovev, A. V., Pellin, M. J., Comstock, D. J. & Hersam, M. C. Nucleation and growth of noble metals on oxide surfaces using atomic layer deposition. in **3,** 271–278 (The Electrochemical Society, 2007).

83. Raróg-Pilecka, W. *et al.* Carbon-supported ruthenium catalysts for NH3 synthesis doped with caesium nitrate: Activation process, working state of Cs-Ru/C. *Journal of Catalysis* **239,** 313–325 (2006).